Multi-Timescale Accelerated Dynamics and Trajectory Analysis of Alloy Surface Transformations Using Novel Interatomic Potentials

by

Richard Burke Garza

B.S. in Chemical and Biomolecular Engineering, William Marsh Rice University, 2019

Submitted to the Graduate Faculty of

the Swanson School of Engineering in partial fulfillment

of the requirements for the degree of

Master of Science

University of Pittsburgh

2022

UNIVERSITY OF PITTSBURGH

SWANSON SCHOOL OF ENGINEERING

This thesis was presented

by

Richard Burke Garza

It was defended on

November 2nd, 2022

and approved by

Thesis Advisor: Judith C. Yang, PhD, Professor, Department of Chemical and Petroleum Engineering

J. Karl Johnson, PhD, Professor, Department of Chemical and Petroleum Engineering

John Keith, PhD, Professor, Department of of Chemical and Petroleum Engineering

Multi-Timescale Accelerated Dynamics and Trajectory Analysis of Alloy Surface Transformations Using Novel Interatomic Potentials

Richard Burke Garza, M.S.

University of Pittsburgh, 2022

Although the equilibrium composition of many alloy surfaces is understood, the rate of transient surface segregation during annealing or oxidation is not known despite their crucial effects on alloy corrosion and catalytic reactions which occur on overlapping timescales. This thesis focuses on computational studies of the surface segregation of CuNi alloys, with methods and analyses generally applicable to all other bimetals. The text summarizes results for the CuNi(100) surface facet primarily in vacuum, with new interatomic potentials introduced to model interactions with oxygen optimized via evolutionary algorithm and deep learning.

We first introduce the CuNi alloy, including its thermodynamically expected behavior in vacuum and oxygen environments. Molecular dynamics (MD) are used to simulate the dominant mechanisms which facilitate surface segregation of the binary alloy system. These preliminary findings are validated using first-principles and Monte Carlo annealing with the embedded-atom method (EAM) to find the equilibrium composition profile versus surface depth, a measurement that provides a defined endpoint for later transient simulations.

Then, three accelerated methods are utilized to transiently evolve the system towards equilibrium: parallel trajectory splicing (ParSplice), adaptive kinetic Monte Carlo (AKMC), and kinetic Monte Carlo (KMC) from cluster expansion. From nanosecond to second timescales, this hierarchy of multiscale approaches can observe stochastic events not typically seen with standard MD, closing the gap between computational and experimental timescales for surface segregation and providing a timescale for vacuum segregation to occur.

The final chapter presents two novel interatomic potentials for the Cu-Ni-O system which can be used within our hierarchy of multi-timescale methods to furnish realistic simulations of alloy oxidation: one reactive forcefield (ReaxFF) developed utilizing an evolutionary algorithm, and a larger set of parameters trained with deep learning tools available in the DeepMD kit. We assess the performance of both forcefields through comparison to DFT results for the Cu, Ni, CuO, NiO, and CuNiO bulk and surface-terminated systems.

Keywords: Molecular dynamics, accelerated dynamics, interatomic potentials, evolutionary algorithms, deep learning, alloys, phase separation, surface segregation, oxidation, thin films.

Table of Contents

List of Tables

List of Figures

Preface

I would like to thank my advisors and lab group members, who have always inspired and motivated me to learn and adapt, even if we couldn't always meet in person. Special thanks to Stephen, Meng, Xianhu, and Henry, who all taught me new skills in the lab and on the computer, patiently answered my questions, had masks for me when the first lockdown began, gave great Pittsburgh restaurant recommendations, and so much more.

Additionally, I'm grateful to the members of my graduate committee, without whose patience and support this work would not be possible. My time at Pitt has been exceptional and unique, in unforgettable experiences with professors to the challenges of remote work, I've been blessed with many growth opportunities. The faculty here have supported me in my goals, and I'm forever thankful.

This work is dedicated to my fiancée, Kendal, my guiding star and the light of my life, who has been with me from the start of my graduate career and will be long after. You inspire me to hold onto hope for the future and dream big. Thank you for always holding me to my highest standard, bringing balance to my world, and supporting me in both good times and bad.

1.0 Introduction

The study of alloy surface transformations bridges the fields of materials science and chemical engineering. As the system size for surface chemistry approaches the atomic and nanoscale where experimental resolution becomes an issue, computational tools prove essential in examinations of dynamical processes, revealing the atomic mechanisms and kinetics underlying more macroscopic behavior like surface segregation. In this process, tension caused by dangling atomic bonds on the exposed area will thermodynamically drive one constituent metal towards sites with low coordination near vacuum, segregating the other metal towards fully-coordinated sites within the bulk[10, 14, 28]. This phenomenon is a contributory effect to corrosion at the nanoscale, substantially altering the alloy composition in the topmost atomic layers relative to the overall, bulk composition. Alloy surfaces are typically enriched with one particular metal due to that element's lower surface energy in the pure state compared to other elements in the mixture[14, 93].

Because it is driven by a difference in surface tension, surface de-mixing occurs even in inert gas or vacuum, inadvertently altering the useful properties gained from homogeneously alloying pure metals together before the material's service life even begins. Alloy surface segregation and ordering has been measured experimentally both in vacuum and gas environments, with differences in the equilibrium alloy composition induced near the exposed top layers for many bimetallic alloys[10, 14, 28, 48, 57, 118]. Consequently, studies of alloy surface transformations are influenced by prior phase separation in vacuum during thermal pre-treatment. A decoupling of the experimental environment from the pre-treatment annealing environment is required to understand the transient effect on non-equilibrium surface composition, since nanoscale elemental mapping is not feasible on relatively short microsecond (μs) timescales even using electron and X-ray diffraction [16, 74]. There is limited understanding of the degree to which oxidation and vacuum segregation can compete, or if they even occur at the same timescales.

This thesis addresses these issues with a novel hierarchy of computational dynamics and developed interatomic potentials, filling the spatiotemporal gap between experimental and computational approaches. Some of the mechanisms underlying surface transformations occur early in the non-equilibrium dynamics, and can be sampled with short (ns) molecular dynamics (MD) simulations; the identified transitions can be validated with first-principles theory. Earlier studies in the literature guide the search for mechanisms of binary alloy segregation. Thermodynamic trends for CuNi surface segregation are presented in the results section of Chapter 2 and compared with existing findings. Behavior on short timescales and equilibrium timescales informs intermediate and long timescale, with results published in the Journal of Chemical Theory and Computation [35].

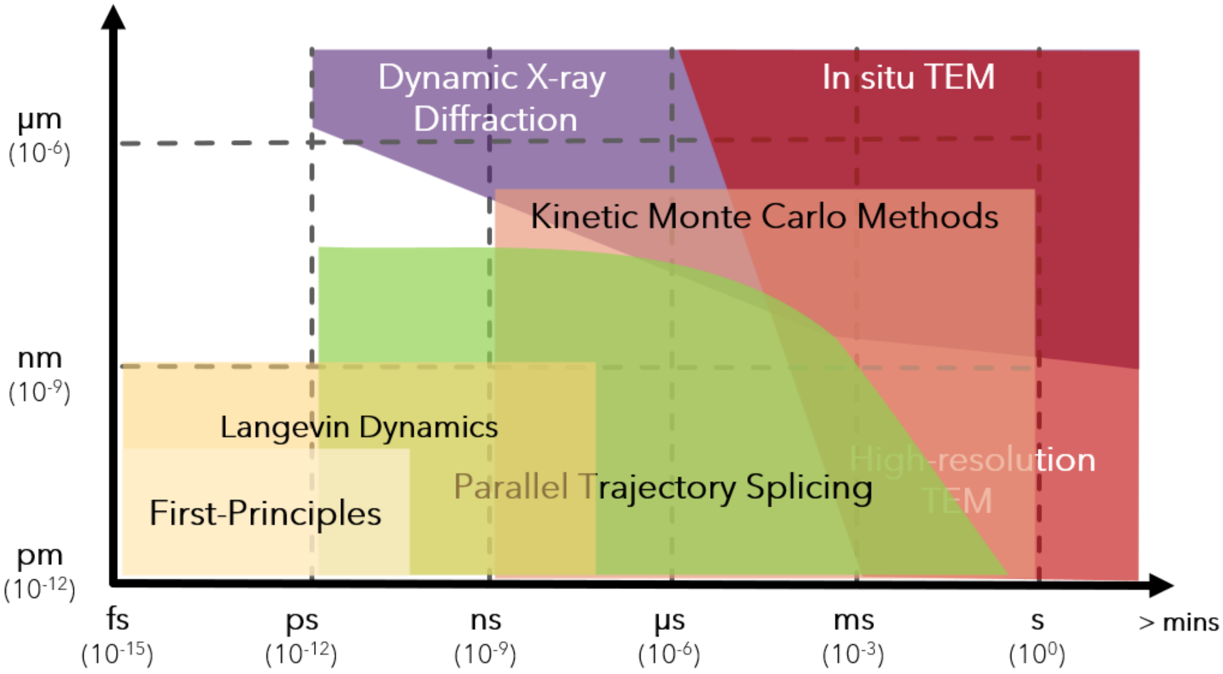

Figure 1: Spatiotemporal gap spanned by accelerated dynamics (ParSplice, KMC) between conventional computational methods and relevant experimental techniques

Accelerated methods explore greater timescales, while early timescale simulations are carried out with standard MD and equilibrium states are found using Monte Carlo (MC) annealing (Chapter 2). The studies reported in Chapter 3 utilize a variety of multi-timescale simulation methods to perform accelerated atomistic dynamics for the CuNi binary alloy, sampling the early transient, intermediate, and equilibrium states of alloy surfaces during the segregation process. This study generated milliseconds and even multiple seconds of alloy segregation, directly comparable to experimental observations.

The third chapter describes the application of accelerated MD methods to binary alloys, which rely on developments in transition state theory (TST) to fill the remaining time gap between conventional MD and experiments (μs to s). TST was first pioneered by French mathematician René Marcelin in 1915 [70], who used it to describe products and reactants as separated by a "dividing surface" in phase space across which reaction rates could be determined from fluxes. The theory was later reinvigorated by Henry Eyring, Meredith Gwynne Evans, and Michael Polanyi in 1935 [30] who simultaneously co-developed the Eyring equation. Vast improvements to TST using variational approaches in the latter half of the 20th century revealed deep connections between the mathematics of stochastic processes and those governing semi-classical dynamics like conventional MD[60]. These fundamental connections will be detailed in chapter three within the context of MD acceleration up to realistic timescales.

These dynamical simulations utilize semi-empirical potentials, or force fields, trained to reproduce the behavior of first-principles DFT and experimental measurements. The fourth chapter deals primarily with the development of force fields from first-principles data. Because there is no pre-existing interatomic potential to describe oxygen interactions with CuNi alloy, we optimize force field parameters between these nuclei. The first optimization begins from separate reactive forcefield (ReaxFF) parameters in the literature for CuO and NiO, combining the two sets into a single CuNi alloy oxidation potential using an evolutionary particle swarm method, with my code provided at `github.com/15garzab/pso_rff`. Then, deep learning is applied to create a much larger parameter set that is able to achieve lower overall error. The second optimization utilizes a Python/C++ package, DeepMD, with the same input structures as before to develop a neural network potential (DeepPot) which describes the oxidation of CuNi surface more closely, with code provided by the developers at `github.com/deepmodeling/deepmd-kit`.

The CuNi alloy is of interest for different applications with extreme environmental conditions, including marine settings due to its resistance to corrosion by seawater[49, 99] and for its utility in thermal catalysis of CO_2-to-syngas-to-fuels reactions[8, 68, 115, 97]. Typically, the "cupronickel" alloy exhibits surface segregation at elevated temperatures in vacuum, enriching with Cu near the surface and Ni in the bulk[43, 108]. In all orientations, the top three monolayers experience significant decrease in Ni solute concentration, which approaches its value in the bulk at a depth of four or five atomic layers below the vacuum[37, 34, 98]. This alters its performance for any future heterogeneous catalysis, in which the available surface concentration of Nickel must be well-tuned[84, 113, 115].

However, alloy segregation and timescales related to the bimetallic dynamics are not well understood in nanoscale thin films, as these require larger systems (>100 atoms) and non-equilibrium dynamics to accurately simulate the region between bulk and exposed surface. These larger, periodic systems can approximate the semi-infinite boundary for dopant concentration present in thin films, which could differ from that of nanoparticle (NP) systems at least for relatively small examples[47, 109]. In addition to varying finite-size effects between NPs of different sizes, NPs also exhibit strain responses from overall lower surface coordination near edges and vertices compared to pristine, periodic films without these edges.

Further, strain effects result in core-shell structures for CuNi NPs that do not appear in thin films[8, 106]. A recent KMC study investigated the dynamics in bulk NiFe solid solution, reporting that the vacancy migration barrier is highly influenced by the local composition, behavior that the authors predict will influence the rate of microscale phase transformations[32]. Previously, only the dependence of activation energy on overall alloy composition could be predicted or measured with any accuracy[39]. The failure of these global models for concentrated solid solutions is known, though they may be corrected by sampling transition energies in differing chemical environments[79]. We do this later in Chapter 3 using adaptive KMC (AKMC).

In place of DFT, it is common in the field of molecular simulation to derive model Hamiltonians from physical intuition (Ising model, Lennard-Jones potential, etc.), statistical mechanics, and/or semi-empirical models[36, 57, 59, 85, 98]. These interatomic potentials aim to reproduce physical behavior from both experiments and *ab initio* theory. In the current work, we take advantage of the embedded-atom method (EAM) to model the system energy of CuNi binary alloys, a modified pair potential that also accounts for local electron density effects[33, 76, 78]. Novel potentials describing interactions with oxygen are presented in Chapter 4, which are in preparation for journal submission.

This thesis contains material first reported in the following publication:

R.B. Garza, J. Lee, M. H. Nguyen, A. Garmon, D. Perez, M. Li, J.C. Yang, G. Henkelman, and W.A. Saidi, *J. Chem. Theory Comput.* 2022, 18, 7, 4447–4455, doi:10.1021/acs.jctc.2c00303

Primary contributions to the research, results, data analysis, text, and figures were provided by the University of Pittsburgh (Garza, Li, Yang, and Saidi), including all data collection and simulations involving DFT, MC, MD, and ParSplice (Garza). Part of this work has been reprinted in the present thesis according to the American Chemical Society (ACS) Journal Publishing Agreement and scholarly sharing policies. Initial guidance for running ParSplice with application to binary alloy segregation was provided by Los Alamos National Laboratories (Garmon, Perez), though all simulation and data collection was performed at Pitt (Garza). Data collection with KMC-based methods was performed by collaborators at the University of Texas at Austin (Lee, Nguyen, and Henkelman), who provided Figure 7 which was then refined by Pitt (Garza). All other figures were created at Pitt (Garza).

Further work was conducted to develop novel interatomic potentials for the Cu-Ni-O system, with specific application to the nanoscale surface oxidation of CuNi alloy. Parameters from the literature for Ni-O [122] were improved to better match first-principles data (Garza) after creation of a particle swarm optimization approach which yields more accurate force fields than the standard Gaussian perturbation (Garza, Curnan, and Saidi). The method was then applied to re-scale pre-existing Cu-O parameters [121] alongside the improved Ni-O parameters to create a novel Cu-Ni-O force field from a set of structures relaxed with DFT (Garza). A separate deep learning method (DeepMD) was applied to ab initio MD trajectories created from the previously mentioned training structures to train a more accurate potential with exclusive application to CuNi surface oxidation (Saidi) with less general applications than the ReaxFF potential. A series of benchmarks were created for all developed potentials (Garza).

2.0 Early and Equilibrium States of CuNi(100)

This chapter contains material adapted from the following publication:

R.B. Garza, J. Lee, M. H. Nguyen, A. Garmon, D. Perez, M. Li, J.C. Yang, G. Henkelman, and W.A. Saidi, *J. Chem. Theory Comput.* 2022, 18, 7, 4447–4455, doi:10.1021/acs.jctc.2c00303

MD can generally resolve atomic transitions on the picosecond (ps) to nanosecond (ns) timescales. While these short timescale dynamics can be easily investigated using energetic models based on either classical force fields or first-principles methods, longer timescales that are often more relevant experimentally are challenging to realize with conventional resources and techniques[104, 73, 75]. This chapter details these conventional techniques: first-principles density functional theory (DFT), MD, and the MC algorithm, including previous literature findings regarding CuNi segregation that we replicate.

2.1 CuNi Surface Segregation from First-Principles

For solid phase diffusion, extended systems that repeat periodically in all directions in multiples of the box length are suitable to describe large surfaces with many layers of depth, representing the semi-infinite boundary within the interior of an alloy relative to its surface. To generate a surface slab geometry with vacuum above and below the slab, the command-line tool *atomsk* by Pierre Hirel[45] is ideal for removing atoms to create a symmetric slab with mirrored areas exposed to the same vacuum. The following command generates a Cu(100) slab with $N_{Cu} = 90$ and ~ 9 Å of vacuum between either side:

```
atomsk --create fcc 3.62 Cu orient [100] [010] [001] -dup 3 3 5 -cut above 9 z POSCAR
```

The file type is determined by the final argument i.e. “POSCAR” outputs the resulting structure as a POSCAR file for VASP (DFT) input. This contains the simulation box geometry, including void space for the vacuum and atom positions relative to the box origin. This void is wide enough to avoid spurious interactions between the two surfaces.

2.1.1 Limits of Simulating Realistic Vacancy Concentration

It is known that the rate of metallic phase separation depends on the defect density in the lattice, which would naturally facilitate atomic migration at low vacancy concentration, and larger dislocation junctions at high vacancy concentration[56, 79, 13]. The latter scenario is unlikely except in the event of neutron/alpha particle bombardment in radioactive settings. However, the availability of surface and subsurface vacancies on exposed metals is highly influential for surface vacuum segregation [48, 61, 63], reduction[20] and oxidation[65, 19, 120, 121, 119, 69]. For a single metal, the equilibrium vacancy concentration at a temperature T can be approximated using the vacancy formation energy for the pure metal, the law of mass action, and assuming that the activities of pure solids are unity:

$$x_{vac}^{i,eq} = \frac{K_{eq}N_{vac}}{N} = A\exp\left(-\Delta G_f\right) \sim \exp(-\Delta H_f)\exp\left(T\Delta S_f\right) = \exp\left(-\frac{E_{f,i}^{vac}}{kT}\right) \tag{2.1}$$

Applying this to available vacancy formation energies in literature[26, 27, 15] listed in the previous validation of the EAM potential (2.4), one can find $x_{vac}^{Cu,eq} \sim 10^{-13}$ and $x_{vac}^{Ni,eq} \sim 10^{-18}$. The values found with the EAM potential and (A.17) yield $x_{vac}^{Cu,eq} \sim 10^{-14}$ and $x_{vac}^{Ni,eq} \sim 10^{-16}$. However, simulations involving 10^{13} atoms (> 1 trillion) are infeasible for even the largest computers.

2.2 Molecular Dynamics of Vacancy Migration

Molecular dynamics seeks to evolve the trajectories of particles bound in either periodic or molecular systems under realistic thermodynamic constraints (constant energy, constant volume, constant temperature, etc.). It operates with the assumption that forces on atoms can be easily computed from a pre-determined energetic potential using Equation (A.1), ideally one that is computationally inexpensive. Newton's 2$^{\text{nd}}$ Law for any particle's dynamics is

$$\mathbf{F}_i = m_i \mathbf{a}_i = m_i \frac{d^2 \mathbf{r}_i}{dt^2} = m_i \frac{d\mathbf{v}_i}{dt} \tag{2.2}$$

The relationship between force, particle mass, and displacement in time allows the kinematic equations to be numerically integrated via approximations to these derivatives. It is important to select a small enough timestep such that the dynamics are stable: numerical integration of the equations of motion requires a timestep less than the period of the fastest vibrational frequency[4]. This algorithm is implemented in LAMMPS alongside structural optimization and Monte Carlo annealing. The influence of temperature and pressure on the particle velocities must also be taken into account through some method of velocity rescaling, which will be described in the following section regarding thermostats.

Vacancy detection using OVITO is performed using the standalone Python package, part of the code repository for trajectory analysis presented later in 2.6 and available at `github.com/15garzab/trajectory-analysis-redux`.

2.2.1 Embedded-Atom Method (EAM) Interatomic Potential

Energetic potentials provide an interatomic relationship approximating the less tractable quantum Hamiltonian, allowing the atomic centers to be propagated forward in space and time to evolve true molecular dynamics at minimal computational cost. These models typically contain a pair-wise component, such as the interatomic distance used in the Lennard-Jones potential. The embedded-atom method (EAM) involves a second moment approximation to the electron density, created to amend the errors of the simple pair potential, which mispredicts the cohesive energy and vacancy formation energy for crystalline solids[21]. Although the Cauchy relations for elasticity theory ($C_{12} = C_{44}$) and the relation $E_v^f = E_{coh}$ may hold true for the LJ potential and some noble gases in the solid state, the coordination-dependent properties of bulk, ordered metals show significant deviation from the 1:1 scaling of lattice-bound ideal gases[22].

To address this difference, EAM considers the embedding electron gas as a background potential on which atomic dynamics take place; the "electron sea" of alloys becomes a kind of solvent. In a lattice, the background electron density can be approximated as a linear superposition of the bound electrons from the atoms in the alloy determined by atom type and local composition:

$$E_{tot} = \sum_{i} F[\rho_i] + \frac{1}{2} \sum_{i,j \epsilon i \neq j} \phi(R_{ij}) \tag{2.3}$$

$$\rho_i = \sum_{i} \rho_i^a \tag{2.4}$$

Where F is the embedding functional depending on the local electronic coordination environment provided by neighboring atoms ρ_i and ϕ is the pair-potential between atoms within a certain cut-off distance. Equation (2.4) describes the local electron density as the sum of contributions from nearby atoms i.e. a linear superposition.

All studies in this thesis except those in Chapter 4 involve use of the same EAM potential for the CuNi alloy system from Fischer, Schmitz, and Eich, which was developed to model grain boundaries and the effects of surface tension at the nanoscale[33]. In 2.4, we show that this force field replicates the expected behaviors from first-principles theory.

2.2.2 LAMMPS: Large-scale Atomic/Molecular Massively Parallel Simulator

Simulation methods are made widely available through various implementations: for materials science, one of the most commonly used programs is LAMMPS, which contains algorithms for structural relaxation, MD, nudged elastic band calculations (described in 3.1.1.1), and Monte Carlo annealing (described in the next section). The underlying code, written in C++, assembles neighbor lists (or Verlet lists) of the atoms in the system, allowing for interatomic distances to easily be stored in arrays for quick matrix algebra involving the thermostat and the provided model Hamiltonian. Input scripting takes advantage of these methods and tools within LAMMPS. For example, a structural relaxation following the conjugate gradient method for optimization could be performed with the following commands:

```
min_style cg
```

```
minimize 1e-8 1e-6 100 1000
```

Where the additional parameters for the "minimize" command are, in order, the energy tolerance, force tolerance, number of force iterations per optimizer step, and number of energy iterations before convergence. These parameters set the minimum change in energy and forces before the optimizer finishes relaxation of the chemical structure.

Static calculations such as this are much less time-intensive than MD simulations. One of the primary benefits of LAMMPS for MD is its parallelization in the spatial domain: a simulation volume is split into separate domains, each of which contains atoms that mostly do not interact with atoms in distant domains. Spatial domain decomposition allows each portion of the simulation volume to be time-integrated by a single processor, receiving inputs from neighboring regions with their own respective processors. Although the task is distributed among the processors, the computation of neighbor lists for all atoms remains the most expensive part of the Verlet algorithm, since each domain must still account for atomic interactions from neighboring domains.

To omit calculating many zero interactions with distant atoms in the system–or spurious interactions in the case of hard sphere overlap–options can be added to modify the neighbor lists. The frequency of neighbor list updates can also be changed. The `neighbor` and `neigh_modify` commands can be used to alter these settings in LAMMPS:

```
neighbor 2 bin
neigh_modify every 10 delay 0 check no
```

The binning method will be used to determine neighbor lists, and the "skin distance" is set to 2 Å. This distance is an additional length added to the force cutoff. The second command sets the frequency of neighbor list updates to every 10 steps without delay steps and without checking for an noticeable change in distances (more than half the skin distance).

The following commands set the units of energy to eV ("metal" units), create periodic boundaries to mirror atoms to the opposite side of the simulation cell (when atoms leave the cell), and read input data:

```
units metal
boundary p p p
read_data data.lmp
```

Thermodynamic constraints can be exerted on the particles in the simulation using various "fixes" to set up modifications to the Verlet algorithm described in A.2. The Nosé-Hoover (NH) thermostat (NVT ensemble) can be applied to the dynamics with the following fix:

```
fix 1 all nvt temp $temp $temp $(100*dt)
```

Where the temperature variable "temp" is used to set the initial and final temperatures (no ramping when $T_{final} = T_{initial}$), and the damping constant is 100 times the timestep size "dt". The 100:1 ratio of damping constant to timestep for integration is commonly employed to generate stable NH dynamics.

Langevin dynamics at constant NVT can be established with a different fix:

```
fix 1 all langevin $temp $temp $(10*dt) 1234
fix NVE all nve
```

There is an internal requirement that the "NVE" fix also be used with the "langevin" fix in order for the forces to be properly calculated during time integration of particle momenta. More details of these commands and the broader specifics of LAMMPS input scripting can be found in the documentation and user manuals.

2.3 Monte Carlo Annealing to Equilibrium

To identify equilibrium configurations of atoms in the topmost layers of CuNi alloy, it is critical to minimize the overall energy of the system. In practice, this means that many atomic configurations must be tested to find the arrangement with lowest energy. As previously cited, X-ray photoelectron spectroscopy (XPS) and Auger electron spectroscopy (AES) experiments for the CuNi alloy on the microscale demonstrate clear segregation of Ni to the bulk after exposure to elevated temperatures in vacuum[107, 14, 105, 108]. To computationally identify the same equilibrated state, a probabilistic state space search algorithm termed the "Monte Carlo" method has been used for many decades to perform simulated annealing, identifying equilibrium atomic configurations for both slabs and nanoparticles[34, 37, 95, 25, 31, 88, 87, 43, 38].

The Metropolis-Hastings algorithm was first published by Nicholas Metropolis and others from LANL in 1953, though it was in use at least a year earlier for research involving the first hydrogen bombs[72, 86]. It uses a search heuristic, the Metropolis criterion, which weights the probability of the next possible explored configuration P_{i+1} based upon its energetic difference with the current configuration P_i:

$$\frac{P_{i+1}}{P_i} = \frac{\exp\left[-\beta U_{i+1}(\mathbf{r})\right]}{\exp\left[-\beta U_i(\mathbf{r})\right]} = \exp\left[-\beta(U_{i+1}(\mathbf{r}) - U_i(\mathbf{r})\right] \tag{2.5}$$

At each step, the potential is used to give a likelihood estimate for an exchange of two atoms of different type relative to the energy lost during this transition. The acceptance criterion depends on a pseudo-random number generated between 0 and 1, which should be less than the likelihood threshold for a move to be accepted (RNG $< P_{i \to i+1}$):

$$P_{i \to i+1} = \min\Big[1, \exp\left[-\beta(U_{i+1} - U_i)\right]\Big] \tag{2.6}$$

Conversely, the exchange is rejected if RNG $> P_{i \to i+1}$. The procedure of sampling the more thermodynamically “acceptable” moves is called importance sampling. The exponential Boltzmann factor used to weight the state by its energy is a familiar term from the partition function of statistical mechanics.

For this series of atomic jumps in the alloy lattice to be considered a Markov process, each transition should be microscopically reversible, that is, each atomic migration can *likely* be reversible. Trajectories escaping from a local basin on the potential energy surface (PES), from one topologically distinguishable state to another, should necessarily have re-crossings unless the reaction is truly irreversible. In a metallic alloy system with two very similar metals (Cu and Ni), migration events are almost guaranteed to be reversible, although the non-equilibrium dynamics near the surface are of critical interest because they should cause an irreversible macroscale change through many stochastic, rare steps. Thus the degree of reversibility should differ in the mechanisms underlying CuNi segregation dynamics and mediate the time it takes for equilibrium to be realized during annealing.

Unfortunately, in most applications of the MC method, it is practical and often necessary to accelerate the annealing by exchanging atoms unphysical distances (beyond the nearest-neighbor distances) away from their starting positions. Thus, large energy drops can be sampled in few iterations via the acceptance criterion. Although the equilibrium state is discovered more quickly and the transitions obey detailed balance, the timescale for the atom exchange is unknown. Accelerated dynamics methods introduced in Chapter 3 carry out trajectories composed of realistic, atomic migrations, each with a measurable time duration for varying mechanisms.

2.4 Results: Cu and CuNi Surface Energies

The surface energies of doped Cu surfaces up to 2.7at%Ni were computed using DFT and the EAM potential of focus in this work: this was done not only to validate the forcefield's application in the study of surface segregation, but also to examine the process with ab initio accuracy[33]. We used the Vienna Ab Initio Package (VASP)[53, 54, 55, 12] in conjunction with the Perdew-Burke-Ernzerhof (PBE)[82] exchange-correlation functional and an energy cutoff of 500 eV to expand the wavefunction. We used a 3 x 3 x 1 k-point mesh generated with a Monkhorst-Pack routine to sample the Brillouin zone for (100), (110), and (111) slab models composed of 100 atoms. All calculations are spin polarized. We used a slab approach to model the surfaces and included 10 Å of vacuum between exposed surfaces to mitigate spurious interactions in the non-periodic direction. One of the host lattice atoms in the system (Cu) were replaced with Ni at both surface (1^{st} layer) and subsurface (2^{nd} layer) positions. The surface energy of a pure Cu slab model with (hkl) orientation including N_{atoms} is calculated relative to the bulk energy per atom E_{Cu} and the total exposed area 2A:

$$E_{hkl}^{surf} = \frac{E_f^{pure} - N_{atoms} E_{Cu}^{bulk}}{2A} \tag{2.7}$$

The equation for surface energy of structures containing one dopant atom is very similar to (A.7), and requires the bulk energy per atom of the dopant (Ni in this study):

$$E_{hkl}^{surf} = \frac{E_f^{doped} - (N_{atoms} - 1) E_{Cu}^{bulk} - E_{Ni}^{bulk}}{2A} \tag{2.8}$$

The pure Cu surface energies for orientations with low Miller index ($h^2 + k^2 + l^2 \leq 3$) are shown in Table 1, which were calculated with DFT and EAM. As is known from previous calculations and measurements of surface energy for pure Cu, (111) surfaces are most thermodynamically stable, followed by (100) and (110) surfaces. The validation with pure Cu surfaces finds 2.6% average relative error between the EAM potential and first-principles. We then replaced one atom in these structures with Ni to study the effect of doping at different surface depths.

Table 1: Surface Energies of pure Cu from DFT and the EAM potential of Fischer et al[33]

	DFT (J/m^2)	EAM (J/m^2)
Cu(100)	1.412	1.357
Cu(110)	1.477	1.488
Cu(111)	1.208	1.246

Table 2: Surface Energies of Cu with 1x Ni dopant atom included on the surface, subsurface, or interior (1st, 2nd, or 3rd layer) to illustrate segregation trends from DFT and EAM

	CuNi(100)		**CuNi(110)**		**CuNi(111)**	
Layer #	DFT (J/m^2)	EAM (J/m^2)	DFT	EAM	DFT	EAM
1st Layer	1.387	1.371	1.457	1.512	1.165	1.264
2nd Layer	1.360	1.365	1.430	1.505	1.150	1.256
3rd Layer	1.364	1.362	1.429	1.501	1.152	1.247

Oriented slabs along (100), (110), and (111) planes exhibit segregation trends as a function of crystallographic direction in the FCC system for Ni, evident in Table 1-2. EAM calculations of Cu surface energy with an included Ni dopant at various locations have only 4.7% average relative error compared to DFT results. Additionally, the difference in minimized energies between structures with Ni on the exposed surface or beneath it (subsurface) is 0.38-0.39 eV for (100) and <111> Cu surfaces, yet this gap is only 0.17 eV for doped (111) Cu surface. The same trend was found to cause the equilibrium segregation profiles from previous MC studies of CuNi surface separation, agreeing with the calculated energetics in our own validation step[43, 37, 34, 25, 31]. Overall, the trend indicates that Ni will segregate towards subsurface sites to relax the local surface tension.

Additionally, the monovacancy migration energies for pure Cu and pure Ni are approximately 1.29 eV and 1.57 eV, respectively, as calculated with Equation (A.17) from Appendix A.4. These negligibly differ from literature values for Cu (1.28 eV) [26] and Ni (1.79 eV) [27].

2.5 Results: Monte Carlo Composition Profiles vs. Depth

We employed slab models of the (100) surface termination that are composed of 216 and 384 atoms by randomly substituting Cu with Ni. These slabs were 12 monolayers in thickness with 3x3 and 4x4 surface periodicity; nearly doubling the vacancy concentration (1:216 vs. 1:384 atoms) did not affect our observed mechanisms or energetics. Thus, systems of smaller surface periodicity (3x3, 216 atoms) were simulated to realize the longest timescales for higher fidelity time-averaging and activation energy histograms. MC simulations across the composition range of 2.7 – 16at% Ni, and temperature range of 300 – 700 K showed no detectable variation in the amount of Ni segregated. For this reason, we chose to exclusively simulate systems with 16at% Ni at 500 K with the accelerated MD methods later in Chapter 3.

Because the low temperature (500 K) used in the work negligibly alters the alloy lattice spacing, the structures do not require NPT equilibration of the system and slab volumes. Our simulation approach fixes the slab volume (NVT ensemble) during the equilibration and production phases by maintaining a constant surface area for both sides of the slab.

The simulated annealing attempted 10^6 MC swaps of Cu and Ni atoms with subsequent minimization between exchanges. The equilibrium composition profiles obtained with MC (Figure 2) exhibit Ni migration out of the top three surface layers, while the concentration of the fourth and fifth layers approach the bulk value. This trend did not quantifiably vary with changes in system temperature or Ni concentration. The near-surface Ni concentration observed with the EAM potential agrees with the profiles derived from previous MC simulations [43, 37, 34, 98, 80] as well as experiments [10, 108, 14, 28].

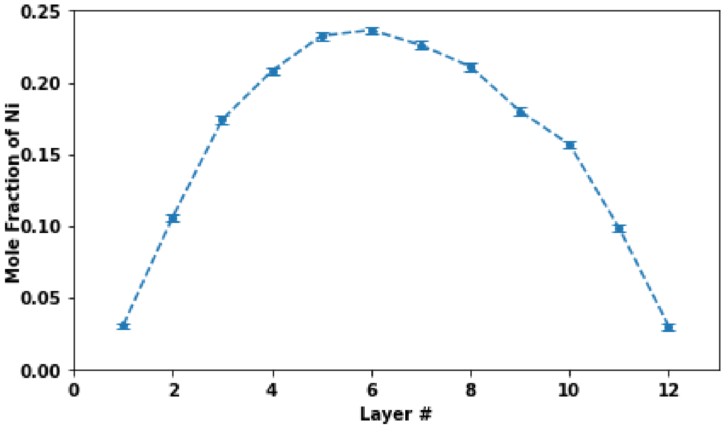

Figure 2: Ni composition profiles of Cu-16at%Ni (100) surface as a function of layer depth after MC annealing at 500 K. The slab has 12 layers with layers 1 and 12 exposed to the vacuum. Composition is normalized by 18, the number of atoms in a pristine FCC <100> layer, resulting in a mismatch between the bulk composition of layer 6 (∼22at% Ni) and the overall composition (16at% Ni).

Importantly, each step in the MC annealing is correlated with its neighboring steps, although this correlation vanishes as incremental steps cause more changes in the system configuration ($n_{steps} \to \infty$). Similarly, in molecular dynamics, the correlation coefficient between states should vanish as their separation time increases ($t \to \infty$). To compute the error bars in Figure 2, the correlation between sequential measured compositions was calculated first. The correlation coefficient allows an estimate of the true error from the underestimate obtained from naive comparison of two correlated measurements, a procedure described in Appendix A.3.

2.6 Interparticle Trajectory Correlation Analysis

The correlation decay as a function of time can be measured directly from the position coordinates of atoms during key transitions, allowing spatiotemporal relationships between atoms and vacancies to be developed. This is a novel method for characterizing reaction mechanisms that, to my knowledge, has not been applied to molecular dynamics trajectories. Coordinated movement of particles within a single reaction mechanism can be summarized using the cross-correlation coefficient of their cartesian coordinates. For two particles A and B with trajectories evolved for n timesteps, let the $n \times 3$ matrices $\mathbf{A} = [\mathbf{a}_x, \mathbf{a}_y, \mathbf{a}_z]$ and $\mathbf{B} = [\mathbf{b}_x, \mathbf{b}_y, \mathbf{b}_z]$ consist of column vectors $[\mathbf{a}_i, \mathbf{a}_j, \mathbf{a}_k]$ representing a time series for each coordinate axis. Because alloy segregation occurs in the z-direction, normal to the surface, we can focus first on the vertical component of interparticle cross-correlation:

$$\rho_z^{AB}(t_1, t_2, \tau) = \int_{t_1}^{t_2} \mathbf{a}_z(t - \tau)\mathbf{b}_z(t)dt \tag{2.9}$$

where the cross-correlation will necessarily change based upon the two points in time chosen during the particle trajectories. Convolution over a set of offsets or lag times $\tau \in [-\tau_{max}, \tau_{max}]$ reveals leader-follower relationships between the two particles[92]. There will be a noticeable maximum/minimum in correlation during particle exchange with a vacancy in the lattice, which can be visibly confirmed using chemical visualization software like OVITO[94]. By dividing the total timesteps n into bins or "epochs", one can produce a heatmap of the interparticle correlation coefficient as a function of time and τ similar to the example shown in Figure 3. The left vertical axis represents time in this diagram, while the horizontal axis represents the set of τ supplied to Equation (2.9). The slightly darker blue patch at $\tau \approx 25$ between Epochs 196-210 implies that the incoming vacancy determines the dynamics by approaching the Ni atom from beneath, segregating it towards the bulk during exchange.

This method of measuring time series correlation is used in finance to predict asset pricing trends relative to one another[92]. I have repurposed the technique in the context of molecular dynamics with the goal of detecting unique spatial relationships evolving in time

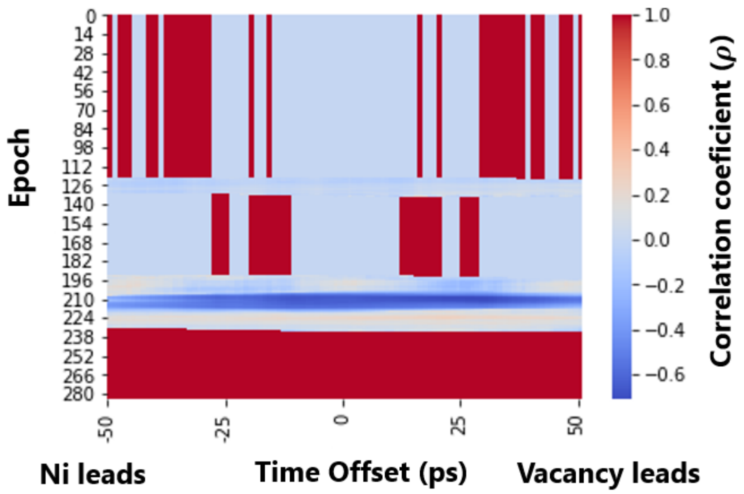

Figure 3: Rolling window cross-correlation heatmap comparing the z-coordinates over 40 ns for a segregating Ni atom (negative offset) and a counter-migrating vacancy (positive offset). Time is binned in epochs on the vertical axis while time offset τ is on the horizontal axis. Solid red bands denote a numerical error filled with the default value($\rho = 1$).

during interparticle exchange. The method characterizes not only the simple monovacancy exchange but also a more complex divacancy mechanism. The activation energies for both these processes are described in section 3.2.3. The code is written in Python, utilizing the OVITO package to detect vacancies with Wigner-Seitz analysis: a self-made tracking algorithm propagates the positions from frame to frame. Finally, a matrix of windowed cross-correlations is computed with `NumPy`, which provides the fastest implementation. The open-source code is available publicly at `github.com/15garzab/trajectory-analysis-redux`.

It should be noted that long periods of low correlation may result in numerical errors in calculating cross-correlation coefficient due to division by zero('`NaN`'): a fill color corresponding to an unphysical maximum of $\rho = 1$ was selected to provide high contrast in the correlation heatmaps and localize numerical errors with a distinct bright red. An unnaturally high value of $\rho = 1$ was selected since this never appeared in any calculations with real trajectory data. It is unclear whether the numerical instability results from inadequate bin size or the long time required for the vacancy to approach the particle of interest during its random walk.

A combination of the two issues is likely, since no numerical errors resulted from correlation measurements of systems with high vacancy concentration ($N_{vacancies} > 2$). This concentration, though unphysical, causes rapid point defect alignment into known FCC dislocations, leading to dopant segregation with simultaneous glide near the junction locks. Small or large bin sizes did not induce numerical errors for this system's dynamics, which are highly deterministic due to junctions. These dynamics result in a more clear signal characterized by the cross-correlation heatmap in Figure 4, which compares a single segregating Ni with one vacancy in a group of counter-migrating point defects, which arrive at the surface simultaneously via dislocation glide.

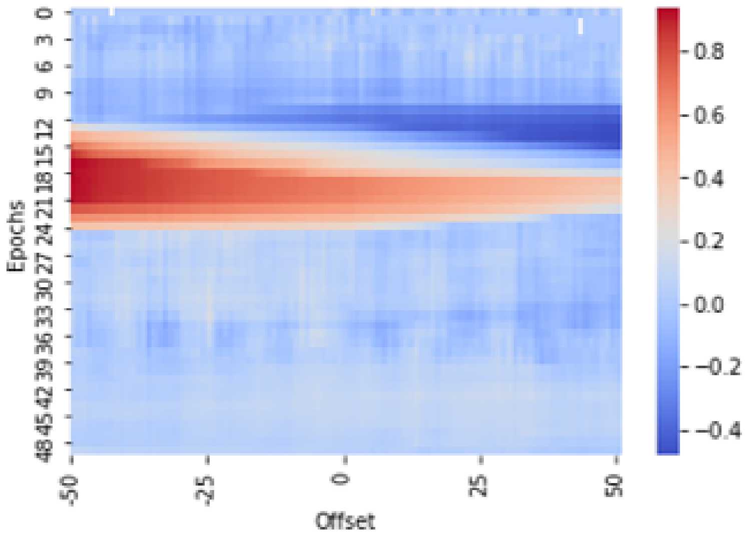

Figure 4: Rolling window cross-correlation heatmap comparing the z-coordinates over 5 ns for a segregating Ni atom (negative offset) and a counter-migrating vacancy (positive offset). Time is binned in epochs on the vertical axis while time offset τ is on the horizontal axis. Solid red bands denote a numerical error filled with the default value($\rho = 1$).

Leader-follower dynamics are much more obvious in the case of high vacancy concentration (large pre-peak at $\tau = 50$), since the position and orientation of a dislocation uniquely determines which Ni atoms have available pathways for segregation in the defective Cu matrix. Spatiotemporal details of reaction mechanisms are quickly deduced by this method.

This chapter has detailed the first-principles, MD, and MC simulations of CuNi alloy segregation, finding that Ni segregates into the bulk even on small timescales, but especially as annealing is carried out on experimental timescales of seconds and minutes to equilibrium. Additionally, a novel particle trajectory analysis method was described in which the cross-correlation of atom and vacancy coordinates can be computed to identify particle exchange during migration and segregation. This approach spatiotemporally localizes events hidden within the FCC structure of the alloy to allow for more nuanced representations of the process to be visualized with a heatmap of vertical, radial, and angular coordinate frames. This method will be applied to great effect in Chapter 3.

In future, cross-correlation heatmaps can be used to analyze heterogeneous surface reactions like oxidation, since diffusing gases in vacuum have much faster dynamics relative to the solid substrate even after adsorption. These events and surface diffusion of adsorbed atoms will be easy to detect because multiple degrees of translational freedom are lost upon surface adsorption. A relatively stationary metal substrate provides a consistent backdrop for correlation with rapid heterogeneous reactions. In other words, metallic diffusion occurs much more slowly than gas diffusion, providing a strong difference in cross-correlation signals before and after surface reactions.

However, because surface defects are the primary site for gas adsorption, the annihilation of vacancies with adsorbed oxygen and metals diffusing into formed oxides will complicate heatmap characterization of vacancies. This represents a new problem for vacancy tracking using Wigner-Seitz analysis. Furthermore, before oxide growth is developed, the initial stages of oxide formation are not characterized by a well-defined lattice, exacerbating detection of the underlying Bravais lattice until the oxide is already more than a few layers thick. Vacancies may disappear and reappear as the local lattice geometry is redefined while atoms move into regions that were previously considered defects or voids.

Initial work has already been performed using the force fields in Chapter 4 for Cu-Ni-O interactions using hybrid MD/MC in NVT and grand canonical ensembles. These simulations are in preparation for submission to journals alongside the force field benchmarks in our results: at equilibrium, the expected trend of Ni segregation is inverted. Ni atoms are pushed to the surface to form nickel oxides above 0.125 fractional monolayer (ML) coverage i.e. NiO is formed preferentially at equilibrium when $\theta_O > 0.125$.

3.0 Intermediate States of CuNi(100) from Accelerated Dynamics

For vacuum segregation of binary alloys, the critical vacancy migration events occur near the surface of the alloy, enriching the surface with the metal of lowest surface energy. For the CuNi alloy, it is thermodynamically unfavorable for a vacancy to re-enter the sub-surface ($E^{\text{migration}}_{\text{surf}\rightarrow\text{subsurf}} \approx 0.8$ - 0.9 eV), a result found later in section 3.1.1.1. This differs significantly from the vacancy percolation back to the surface ($E^{\text{migration}}_{\text{subsurf}\rightarrow\text{surf}} \approx 0.4$ - 0.6 eV), a fast process occurring typically within nanoseconds across several atomic layers of depth. The latter can be sampled with conventional MD but the former requires more advanced methods of molecular simulation.

Rare events like vacancy re-entry cause alloy re-ordering on the nanoscale: in our systems, the vacancy cyclically visiting the surface and leaving represents the lowest energy pathway for segregation to occur. Stochasticity during this process implies that there is a degree of rarity for some transitions based on physical availability from the current state (i.e. frequency factor) and the activation barrier. The flux of Ni to the bulk can be monitored directly with MD but not to completion due to the long time required between events, which depend on the random walk of the vacancy through the lattice. Accelerated methods bridge this gap.

Transition state theory (TST) is essential to measure the rates of slow processes like vacancy re-entry, which occur rarely in the dynamics but are essential to inducing larger nanoscale phase transitions. Yet, to date, the transient dynamics of segregation in CuNi have not been investigated. Previous studies have employed Monte Carlo (MC) to describe the systems in equilibrium, but they do not give a timescale for the segregation process. In contrast, MD can provide a timescale for the non-equilibrium dynamics, but it has not been utilized before to study transient dynamics of segregation. Limited investigations of dislocation slip under applied stress (work hardening) or melting in CuNi [80, 110] have been carried out using MD because these processes occur over ns timescales, yet the impact on larger scale reordering on experimental timescales was not explored in those studies. Thus, the mechanism, as well as the timescale, for transformation from a randomly mixed to ordered alloy on the nano- and microscales remains unclear.

Accelerated methods can provide insight on longer timescales into atomistic mechanisms of surface segregation phenomena. Previously, AKMC investigations of the segregation kinetics of PdAu nanoparticles showed greater kinetic stability due to reduced strain in the mixed-phase[63]. In that work, the authors also utilized parallel replica dynamics to enhance MD acceleration, combining multiple acceleration methods. In the present work, we probe segregation dynamics in planar, (100) CuNi surfaces, employing conventional MD and three accelerated dynamics methods: parallel trajectory splicing (ParSplice), AKMC, and KMC with kinetic barriers derived from a cluster expansion. ParSplice affords accurate system evolution up to ∼10 μs, while AKMC and KMC simulate longer timescales up to ms and seconds, respectively. The methods employed in our multiscale hierarchy are described in the following sections in order of accessible timescale.

3.1 Transition State Theory (TST) and State Space Exploration

Dynamical corrections to the TST rate constant were identified as necessary by Marcelin in 1915 when first describing the theory, although he could not evaluate the resultant integrals in his time. In the 1960s, James Keck was the first to use MD to statistically correct the rates of collision from kinetic theory, which are often only variational upper bounds for the true reaction rate[52]. This error is caused by re-crossings of the dividing surface between states in phase space resulting in no net reaction and a smaller frequency factor than expected[103].

A formal derivation of the dynamical correction was originally made for two-states (trans-gauche conformations of a polymer chain) by David Chandler by redefining the current state populations in time relative to the equilibrium populations[17, 3].

$$\begin{aligned} \dot{N}_A &= -k_{A\to B}N_A + k_{B\to A}N_B \\ \dot{N}_B &= k_{A\to B}N_A - k_{B\to A}N_B \end{aligned} \tag{3.1}$$

Fluctuations away from the equilibrium values for state occupancy $\tilde{N}_A$ and $\tilde{N}_B$ can be defined as

$$\begin{aligned}\delta N_A &= N_A - \tilde{N}_A \\ \delta N_B &= N_B - \tilde{N}_B\end{aligned} \tag{3.2}$$

As always, the two-state system obeys detailed balance ($\delta N_A + \delta N_B = 0$). Combining this fact with equations (3.1) and (3.2) yields the first order rate law for the fluctuation, which depends on an effective reaction rate:

$$\begin{gathered}\delta\dot{N}_A(t) = -k_{eff}\delta N_A(t) \\ \text{where } k_{eff} = k_{A\to B} + k_{B\to A}\end{gathered} \tag{3.3}$$

The effective reaction rate is not an elementary rate like $k_{A\to B}$ and $k_{B\to A}$. Using perturbation theory, the above form yields the fluctuation-fluctuation autocorrelation function:

$$k_{eff} = \frac{\left\langle \delta\dot{N}_A(0)\delta N_A(t)\right\rangle}{\left\langle \delta N_A(0)\delta N_A(t)\right\rangle} \tag{3.4}$$

where the angular brackets represent the canonical ensemble average. Next, a simple assumption can be stated by recognizing the denominator is a much slower varying function of time than the numerator, admitting the following approximation:

$$\left\langle \delta N_A(0)\delta N_A(t)\right\rangle \approx \left\langle \delta N_A(0)\delta N_A(0)\right\rangle \tag{3.5}$$

We will return to this assumption at the end of the section, since it plays a key role in parallel replica dynamics. The right side is simply the standard deviation of the fluctuation at t = 0:

$$\left\langle \delta N_A(0)\delta N_A(0)\right\rangle = \tilde{N}_A - \tilde{N}_A^2 \tag{3.6}$$

Detailed balance also provides the following relationship for the ratio of equilibrium state populations and their escape rates:

$$\frac{k_{A\to B}}{k_{B\to B}} = \frac{\tilde{N}_B}{\tilde{N}_A} \tag{3.7}$$

So that k_{eff} equation (3.3) becomes

$$k_{eff} = k_{A\to B}\left(1 + \frac{\tilde{N}_A}{\tilde{N}_B}\right) \tag{3.8}$$

Thus, the transition rate depends on the correlation between on the correlation between the current escape flux from reactant state A and the population of the product state B at time t:

$$k_{A\to B} = \frac{-\langle \delta\dot{N}_A(0)\delta N_B(t)\rangle}{\tilde{N}_A} \tag{3.9}$$

This powerful result for the transition rate constant also holds true in the many-dimensional case. The multi-state version originally from Adams and Doll[3], then refined by Voter[103], provides the same result for a generalized state

$$k^{el}_{i\to j} = \frac{-\langle \delta\dot{N}_i(0)\delta N_j(t)\rangle}{\tilde{N}_i} \tag{3.10}$$

where $k^{el}_{i\to j}$ is the elementary rate constant of any transition from i to j. The choice of t in the two-state ((3.9)) and multi-state equations for the transition rate constant is highly influential on the calculated rate. This is because re-crossings of the dividing surface between states i and j are highly correlated with one another up to a certain "correlation time" τ_{corr}, after which the system will have thermalized with noise from the remaining degrees of freedom[103]. Counting the reactive events across all timescales proves to be difficult, since state i can be revisited later in the future. The system may still transition from j back to i, but this latter transition would be uncorrelated with the former unless they are within τ_{corr} of one another.

To surmount this challenge, parallel trajectory splicing relies on small simulation times: if every particle that crosses the dividing surface out of state i irreversibly remains outside of state i, the uncorrected transition rate constant $k^{TST}_{i\to}$ is recovered. The dynamical correction factor f_d must be the ratio of the true rate to this idealized, irreversible rate:

$$f_d(t) = \frac{k^{el}_{i\to j}}{k^{TST}_{i\to}} \tag{3.11}$$

where $1 > f_d > 0$ for times $\tau_{corr} < t_p \ll \tau_{rxn}$ where the correction should decay exponentially to zero as $t \to \tau_{rxn}$. By restricting t_p to be much lower than the reaction time τ_{rxn}, we can easily validate the previous assumption made in (3.5).

The equality $k^{TST}_{i\to j} = k^{el}_{i\to}$ only holds when $f_d = 1$ and $t = 0$. By evolving many replicas from the same state, the first escape time (smallest time) can be discovered among the available trajectories close to $t = 0$. The trajectory segments are then spliced together, each elapsing at least τ_{corr}. Selecting only times on the order of τ_{corr} provides a series of reactive transitions that likely has no missed re-crossings in between. Thus, the parallel replica method can capture nearly all reactive events without significant errors in over or under counting state transitions, obeying detailed balance.

The expressions in Equations (3.9) and (3.10) refer to the flux of particles from one state to another. Thus, a similar expression can be derived in terms of the velocity normal v_i through the dividing surface around state i:

$$k^{TST}_{i\to} = \frac{\big\langle |v_i(0)|\delta_i(0)\big\rangle}{2\tilde{N}_i} \tag{3.12}$$

$$k^{el}_{i\to j} = 2\frac{\big\langle v_i(0)\delta_i(0)\theta_j(t)\big\rangle}{\big\langle |v_i(0)|\delta_i(0)\big\rangle} k^{TST}_{i\to} \tag{3.13}$$

where $\theta_j(t)$ is a function of the fluctuation from the equilibrium population of state j

$$\delta N_j(t) = \theta_j(t) - \tilde{N}_j \tag{3.14}$$

KMC methods find the elementary reaction rate as a function of the velocity correlation shown in (3.12) and (3.13). In practice, the activation energy E_a from the ground state to the transition state is used to approximate this transition rate. The nudged elastic band (NEB) method is used to identify the transition saddle point on the PES, later shown in equation (3.16) in 3.1.1.1. In the view of KMC (section 3.1.2), the time is not restricted, allowing for very stochastic processes to be described by a slow velocity over the dividing surface. This family of approaches results in a series of transitions with a variable timestep separating them, in contrast with the constant timestep of conventional MD and ParSplice.

3.1.1 ParSplice: Parallel Trajectory Splicing

Parallel trajectory splicing, or ParSplice[83], is an accelerated molecular dynamics method that generates accurate state-to-state evolution by simulating many replicas of a system in parallel, then splicing together trajectory segments by matching their graph topologies. A running database of segments prevents wasteful, repetitive computations and allows for even greater speedup. Using fewer than 224 cores and a week of compute time, we can simulate a trajectory for a system of several hundred atoms, reaching tenths of a microsecond, far beyond the timescales accessible with conventional molecular dynamics.

The method is derived from the earlier parallel replica (ParRep) dynamics of Voter, Montalenti, and Germann, who developed a robust method to calculate expectation values for escape rates from distinct states in phase space[104]. As demonstrated in 3.1, Voter and colleagues' applications of transition state theory have been highly influential for the improvement of basin-hopping algorithms in recent decades. In their treatment, the probability distribution for time of next escape from an arbitrary State A is assumed to obey first-order kinetics after a certain correlation time has elapsed (i.e. higher order rates will decay to a negligible amount once the system is sufficiently de-correlated)[102], and such a process can be expressed as

$$p(t) = k \exp{(-kt)}, \tag{3.15}$$

where k is the rate constant for the escape process, regardless of the favored reaction pathway(s) out of this state. The rate constant changes for each new state visited during the dynamics. The first-order behavior is a natural outcome of any ergodic, chaotic exploration within an energy basin. A dynamical correction factor can be analytically calculated, which depends on the chosen correlation time for the basin-hopping algorithm[103]. We can approximate the random walk of a lone-vacancy in any bulk, solid-state material as an ergodic process obeying Liouville's theorem: in other words, the material derivative (convective time derivative) of the continuum flow is zero. Since equation (3.15) applies to escape from a single basin, we can consider the problem of multi-state basin hopping to be locally ergodic within each basin on the PES.

In this view, each trajectory segment with duration greater than τ_{corr} has no memory of the previous trajectory segments because enough time has elapsed. Rather than sample the average time for all escapes from a basin, which would consist of many uncorrelated revisits and exits, a sampling is made of the first escape time from the basin to form the probability distribution in equation (3.15).

Using the parallel replica approach with M processors and N atoms, each processor can explore phase space independently (after a brief de-phasing period using randomized velocities to avoid correlated trajectories) while covering M-times more states within the energetic basin than the serial approach. ParRep and ParSplice replicas can utilize spatial decomposition across a group of assigned child processors with distributed, spatially-parallelized codes like LAMMPS. That is, ParSplice has LAMMPS as a dependency to provide spatial decomposition, and the overarching replica scheduling algorithm provides temporal parallelization.

This potent combination of state-space exploration heuristics provides a measurable speedup: almost 3x more Ni dopant atoms are observed segregating to the interior of CuNi surfaces. These events significantly change the local composition at the surface layer in Figure 3.1.1.

Many instances of LAMMPS were then orchestrated by the EXAALT/ParSplice code to carry out long-time ParSplice simulations. Direct MD realized ns of simulated time using the velocity Verlet algorithm and modest resources (4 processors). ParSplice accelerated these dynamics up to μs timescales using 224 processors. Both standard MD and ParSplice were carried out in the same way: after initializing particle velocities according to a Boltzmann distribution representing the target temperature, the systems were equilibrated with a 2 fs timestep and a 1 ps temperature relaxation time for 200 ps. Multiple random number seeds are used by ParSplice to initialize system velocity many times during replica dynamics, allowing exploration of the local state space to identify new segments[102]. The first segment identified escaping to a new state is appended to the end of the parallel trajectory. After the equilibration phase of MD, a further 400 ns were simulated to constitute the production phase, while ParSplice was employed to accelerate this simulation time up to 35 μs. Minimization was done with the conjugate gradient algorithm using convergence criteria of 10^{-8} eV and 10^{-3} eV/Å for the energy and forces[91], respectively. These quenching parameters

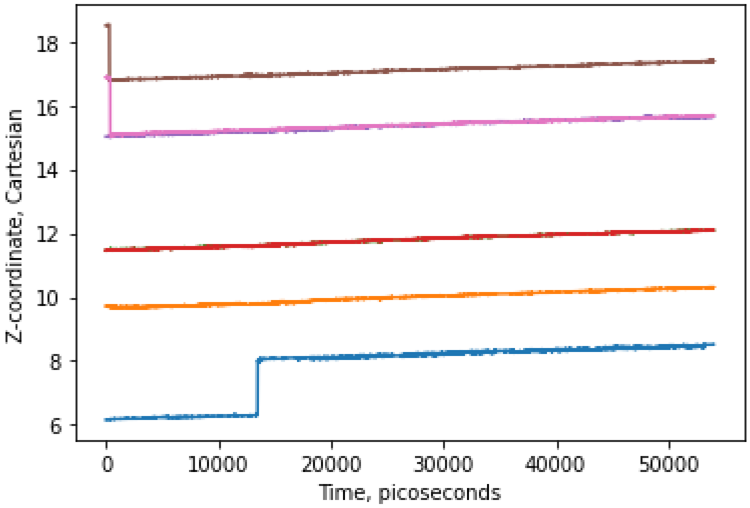

Figure 5: High variance z-coordinates of Ni atoms from 500 K ParSplice trajectory of Cu-16at%Ni symmetric surface alloy within simulation cell containing top surface near 19 Å and bottom surface around 6 Å. Segregation of Ni to the interior marked in blue, pink, and brown.

are also used by ParSplice to identify state transitions and properly terminate each parallel MD replica.

3.1.1.1 Nudged Elastic Band Method

In contrast to the fixed point energies used to obtain structural relaxation/optimization in both VASP (DFT) and LAMMPS (classical MD) which are subsequently utilized in cohesive energy calculations, activation energies are important to differentiate varying elementary mechanisms and rates of binary alloy segregation. NEB barriers determine the rates of transition. Each mechanism of atomic migration within the alloy lattice has an identifying reaction rate each associated with an activation energy. A spectrum of activation energies is sampled over all the available pathways through state space during adaptive KMC, which finds reaction rates on the fly (section 3.1.2). In an alloy, these transitions will primarily involve vacancy counter-migrations to allow metal atoms to diffuse within the crystalline bimetallic system.

To reach experimentally relevant time scales in simulations with greater acceleration than ParSplice, an approach which directly calculates reaction rates is required. For solid systems and for reactions at surfaces, the activated reaction rates are dominated by smooth energy barriers between states. This allows use of the simple harmonic form for the transition rate constant:

$$k = A \exp\left[\frac{-E_a}{kT}\right] \tag{3.16}$$

which is essentially the Arrhenius equation. The difficult part of NEB is identifying the saddle point on the PES which joins reactant and product.

The vacancy migration energy can be found using the nudged-elastic band method, which creates images along a proposed reaction coordinate. These images are structures with various atomic displacements following the chosen mechanism. One of these images will be near the apex of the system energy during this transition, uniquely identifying the peak of the activation energy curve. The approach is dubbed climbing image NEB (CI-NEB)[42, 91].

CI-NEB allows for trajectory discovery during simulation, exploring mechanisms on-the-fly, or adaptively. In lieu of pre-calculating the reaction rates before simulation begins, as was done in the past with lattice KMC [114, 32, 5], the modernized KMC approach instead executes saddle searches to adaptively discover new and possibly unknown reaction mechanisms. For this reason, the simulation method is called adaptive KMC (AKMC).

3.1.2 AKMC: Adaptive Kinetic Monte Carlo

KMC-based methods do not have a fixed timestep; instead, they find the time elapsed for the first escape from one state to another, allowing for large periods of vibrational motion in the atomic system to be bypassed[63, 112]. These escape times correspond to reaction rates, which are calculated adaptively or "on the fly" to construct an AKMC state model: nothing in the output event table is predefined or assumed from prior knowledge[112, 63, 41]. AKMC uses minimum-mode following searches or high-temperature MD to construct this event table: the transition state energies (activation barrier heights) are found using single-ended saddle point finding algorithms such as the dimer method[44, 50, 40].

In contrast to ParSplice and MD, the AKMC and KMC models use a non-constant timestep, which varies to match the timescale of the first escape time from a given state. Over longer timescales, up to many seconds, KMC-based acceleration approaches the segregation found with MC[41, 112]. KMC methods simulate the time evolution of the system, requiring a predetermined event table in which the kinetic rate of each event is approximated through the Arrhenius relation to the pre-calculated activation energy. At each step, a random event i is selected from the table in the order from 1 to i with the condition

$$\sum_{1}^{i-1} r_{i-1} < p_1 \sum_{1}^{N} r_N \leq \sum_{1}^{i} r_i \tag{3.17}$$

where $\sum_1^i r_i$ is the sum of the rate from event 1 to event i, $\sum_1^{i-1} r_{i-1}$ is the sum of the rate from event 1 to event i-1, p_1 is a random number between 0 and 1, and $\sum_1^N r_N$ is the total rate of the event table. Time is then incremented by

$$\frac{-\ln p_2}{\sum_1^N r_N} \tag{3.18}$$

where a random number p_2 is drawn between 0 and 1. AKMC allows the system to find all potential events without need of a predetermined event table [41]. In order to search for events, AKMC uses high-temperature MD and CI-NEB to identify and calculate saddles for the new states using the EON software[41, 112, 40].

3.1.3 KMC from Cluster Expansion

To achieve further acceleration while maintaining as much accuracy as possible, in the present study, we use off-lattice dynamics from AKMC to fit a more approximate, lattice-based KMC model, which functionally depends on the Ni-coordination via a cluster expansion.

An energy estimation based on the local environment of the vacancy was generated by a cluster expansion. The energy was predicted to be dependent on the concentration of Ni and Cu located in the first nearest neighbor shell of the vacancy. In the FCC CuNi alloy, there are eight nearest neighbors for the vacancy on the surface and twelve nearest neighbors for the vacancy in the subsurface. Sequentially, the energy-fitting model was used to determine the barrier and rate of the events in the event table based upon the trajectory data from our AKMC simulations. More information about the cluster expansion method is provided in appendix section A.5. Further, we found satisfactory agreement between AKMC and KMC by carrying out the dynamics up to 300 µs, further validating the KMC model (34).

3.1.3.1 Equilibration Rate for KMC-CE

Finally, the concept of an equilibrium rate is introduced to further accelerate the timescale accessible by KMC. In this approximation, no rate is allowed to be larger than the specified equilibrium rate with the assumption that all states connected by rates faster than equilibrium rate should already be in equilibrium. In the case of CuNi segregation, the planar diffusion of a vacancy on the exposed surface is rapid, equilibrating on much shorter timescales than for defect re-entry to the subsurface to occur even once. Ultimately, the effect of an artificial equilibrium rate in KMC simulations is that these key transitions can be sampled more effectively instead of the many horizontal transitions that do not alter the composition with respect to surface depth.

In both AKMC and KMC simulations, the temperature was set to 500 K and the prefactor for the rates was fixed at 5×10^{12} s^{-1}. The optimizer used in AKMC was L-BFGS, with a convergence criterion of 0.01 eV/Å[91]. System evolution from AKMC reached ms timescales running for a week on 24 cores. The following KMC timings are the average of five separate runs in both cases: KMC realized seconds of simulation time running on a single processor for 2 hours with the added equilibration rate. KMC without the equilibrium rate was only simulated up to 10 ms, since only one minute of wall clock time was necessary before the surface vacancy trapping described above halted Ni segregation in the system.

3.2 Results: Comparison of Multi-timescale Methods

This section contains material adapted from the following publication:

R.B. Garza, J. Lee, M. H. Nguyen, A. Garmon, D. Perez, M. Li, J.C. Yang, G. Henkelman, and W.A. Saidi, *J. Chem. Theory Comput.* 2022, 18, 7, 4447–4455, doi:10.1021/acs.jctc.2c00303

Primary contributions to the research, results, data analysis, text, and figures were provided by the University of Pittsburgh (Garza, Li, Yang, and Saidi), including all data collection and simulations involving MC, MD, and ParSplice (Garza). Initial guidance for running ParSplice with application to binary alloy segregation was provided by Los Alamos National Laboratories (Garmon, Perez), though all simulation and data collection was performed at Pitt (Garza). Data collection with KMC-based methods was performed by collaborators at the University of Texas at Austin (Lee, Nguyen, and Henkelman), who provided Figure 7 which was then refined by Pitt (Garza). All other figures were created at Pitt (Garza).

In this study, we probed the segregation dynamics using MD, ParSplice, AKMC, and KMC starting from the same initial configuration of the random alloy. Lattice vacancies are the primary defect responsible for alloy segregation: the only other mechanism, self-interstitial migration of metal atoms to octahedral or tetrahedral sites, is destabilized by greater formation and migration energies than those for the point defect (vacancy)[56]. Hence, our simulations included a single vacancy to facilitate surface segregation since this the lowest concentration feasible in the system. Decreasing the system size from 384 to 216 atoms had no appreciable effect on transition energies or state occupancy.

Importantly, the formation and migration energies of a di-vacancy are even lower than for the monovacancy[71]. Although it represents a significant, unphysical increase in the vacancy concentration, we found that introducing two vacancies to the system activated an alternate, lower energy mechanism for segregation that merits some discussion.

Rapid diffusion of a vacancy through the slab is resolved by all four methods in tens of ns. Stochastic re-entry of vacancies into the subsurface, however, is only seen on the microsecond timescale in the two KMC methods. Kinetic vacancy trapping on the surface and its effect on the segregation rate are discussed. The equilibrium composition profile of CuNi after segregation during annealing is estimated to occur on a timescale of seconds as determined by KMC, a result directly comparable to nanoscale experiments.

Although the effect of local composition on activation energies (vacancy migration energies) reported from AKMC is low, the influence of vacancy separation is notably influential on the rate of defect migration and percolation towards the surface. Trajectory analysis

Figure 6 shows the composition over time within the top layer of our Cu-16at%Ni (100) slab model for a single simulation of each type within our methodology. The concentration of Ni atoms in the top surface layer decreases over time as it transitions from a uniform distribution to that of equilibrium, as shown by the MC simulations in Figure 2. The accessible simulation time increases sequentially for each method (MD, ParSplice, AKMC and KMC). In MD (Figure 6a), the vacancy diffuses to the surface at 0.3 μs, displacing a Ni atom to the subsurface; up to the total time of 0.4 μs the vacancy remains trapped on the surface so that the Ni concentration does not change. With over thirty different MD simulations, we observed that the time for vacancy percolation to the surface was consistently less than 1 μs, resulting in similar degrees of segregation as shown in Figure 6a.

ParSplice (Figure 6b) shows similar dynamics as in standard MD, with vacancy migration to the surface in a fraction of a μs. Throughout the simulation, the ParSplice trajectory visited 8,278 topologically unique states while making 37,458 transitions, the vast majority of which occurred after the vacancy had reached the surface. The parallel acceleration of ParSplice increased the timescale from the standard MD simulation by a factor of ~100 up to 35 μs, but even at this longer timescale the vacancy remained trapped on the surface and no additional Ni segregation was observed. As expected, ParSplice is consistent with MD on timescales where they overlap (0.4 μs) not only in terms of bulk vacancy diffusion but also the timescale at which the vacancy diffuses to the surface. I have repeated the ParSplice simulations dozens of times with different random seeds observing early vacancy diffusion to the surface (before 1 μs) in nearly all trials, just as with MD.

With AKMC, we increased the simulation timescale by another order of magnitude (Figure 6c): a total of 144,597 transitions evolved the system through 32,369 unique states (a

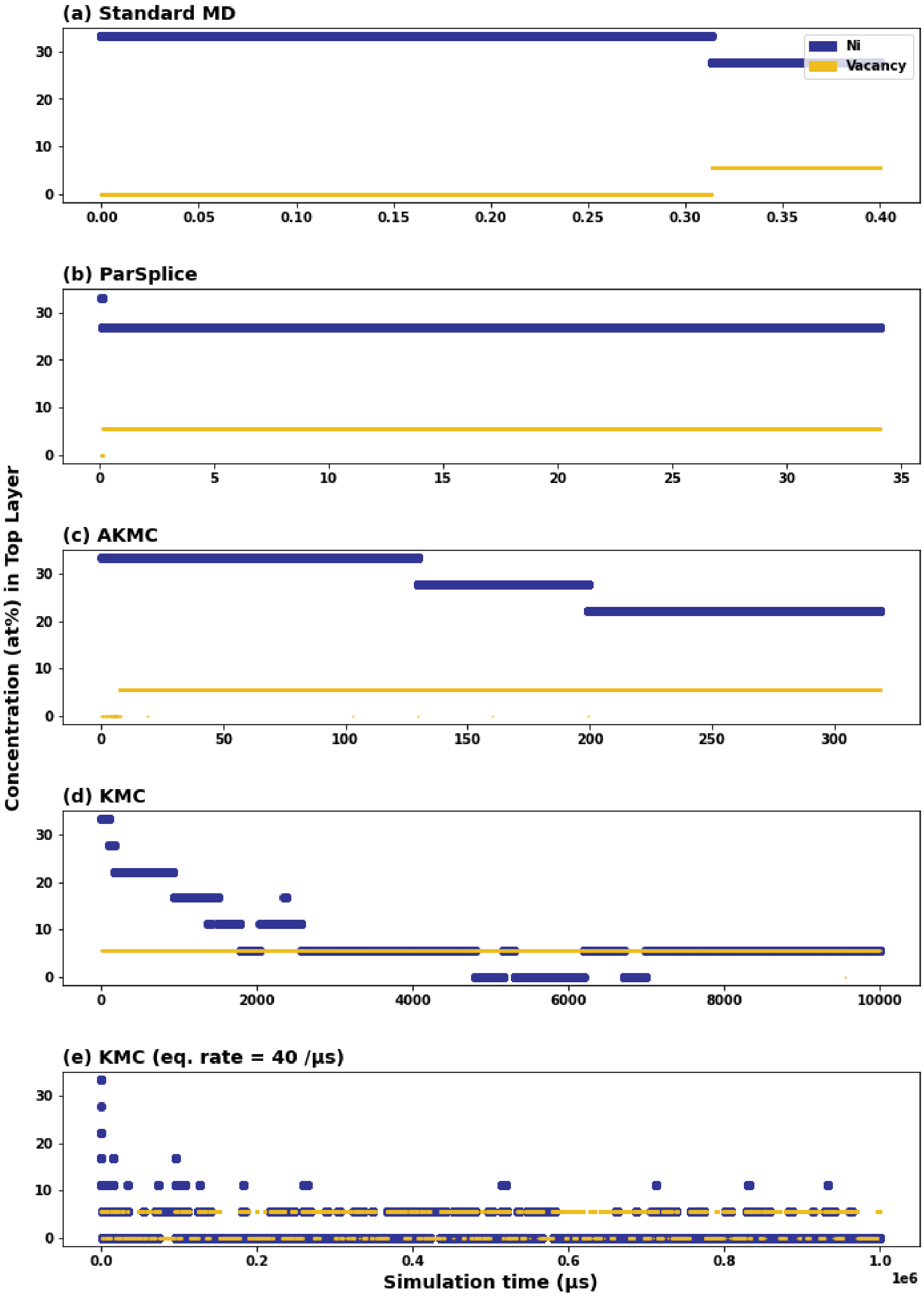

Figure 6: Ni content in the top layer of Cu-16at%Ni(100) with a vacancy for (a) standard MD, (b) ParSplice, (c) AKMC, (d) KMC, and (e) KMC with applied equilibrium rate. Composition is normalized as in Figure 2

similar ratio of transitions to new states found as in ParSplice). Note that our AKMC approach uses coarse-graining following the MC with absorbing Markov chains (MCACM) method, allowing many more transitions to be considered via an analytic solution to the rate equations[77]. From the AKMC dynamics, we can observe events in which the vacancy moves from the surface to the subsurface at a timescale of roughly 50 μs. Percolation to the surface occur multipel times at 20, 105, 140, 160, and 200 μs (yellow dots in Figure 6c). Although the vacancy arrives at the surface multiple times, it does not cause Ni segregation until the third percolation, resulting in some differences with the MD and ParSplice results, though this is only a consequence of the stochasticity of the studied system. Over the simulation time of 300 μs, these five percolation events resulted in 3 Cu atoms and two Ni atoms migrating from the surface to the subsurface.

With our KMC model (Figure 6d), we executed 4.7 million transitions generating 10 ms of simulated time. Over these timescales, the system appears to approach equilibrium, with fluctuations in the surface concentration between 0 and 5% Ni. However, what is not obvious from these plots is that the vacancy spends all of its time in the first and second layer, so that Ni segregation only occurs between the surface and subsurface layers. This behavior originates from a disparity in barrier heights that embodies the "low-barrier problem", more aptly referred to as the "heterogeneous barrier" problem. Dynamics with a mix of low and high activation barriers are inherently more difficult to accelerate since groups of states interconnected by low barriers will always dominate the trajectory during naive state space exploration[73, 83]. The barrier for vacancy surface diffusion is 0.4-0.5 eV, whereas the barrier for the vacancy to go subsurface is 0.8-0.9 eV. Thus, we are simulating on the order of a million KMC steps with the vacancy mostly diffusing on the surface for one subsurface diffusion event, offering a low chance for segregation to occur. Even factoring in the small cost of each KMC step, this makes it impossible to simulate an equilibrium distribution of Ni in the top three layers.

3.2.1 Heterogeneous Barrier Problem

To further accelerate the dynamics and mitigate the "heterogeneous barrier" problem, in our final simulation (Figure 6e), we perform KMC with the equilibrium rate approximation described in the methods section, realizing 160 million transitions to reach a simulated time of 1 s. Here, the idea is that the vacancy will quickly reach local equilibrium diffusing in the top layer, and no new states of interest are explored until subsurface diffusion occurs. Since vacancy surface diffusion occurs on a timescale of ns, and diffusion of the vacancy to the subsurface occurs on a timescale of µs, we chose an equilibrium rate of 40/μs to slow the surface diffusion and accelerate the diffusion of the vacancy to the subsurface and below. Figure 6e shows that on a timescale of seconds, the surface Ni concentration fluctuates around equilibrium after 0.4 seconds until the end of our simulation lasting 1 s.

In order to more accurately estimate the timescale required to obtain the equilibrium profile, we performed five individual KMC simulations with the same equilibrium rate (40/μs), extending the total time to 2.5 seconds corresponding to about 400 million transitions. Although we utilize the per-layer final compositions previously shown in Figure 2 from MC annealing as a predictor for the local equilibrium composition, the moving average for local concentration from KMC may continue to fluctuate after this target composition is first realized. Figure 7 shows the moving average of Ni composition obtained from these KMC simulations in the bottom three layers (referred as layer 1, 2 and 3) and the top three layers (referred as layer 12, 11, and 10) in bold lines compared with the corresponding, non-moving average equilibrium layer compositions obtained by MC (data from Figure 2) in dashed lines. From Figure 7a, we can see that layer 1 reached the MC value in less than 0.1 second and even approached zero Ni concentration at 1.5 seconds, although this does not occur in MC annealing on average, during which a single Ni atom remained on the surface for most of the equilibrium samples (Figure 2). Layer 2 exhibits more dramatic changes. The local composition started from 30% Ni, dropped to the MC composition of 10at% 1.75 seconds, and remained near the estimated value from MC profiles until the end of the simulation. While the MC simulation left 16% Ni in layer 3, our KMC model shows more Ni segregations, leaving 10% Ni in the layer. This might explain the higher Ni composition profiles of the top two sublayers (layer 11 and 10) in Figure 7b. While layer 12 shows similar behavior as layer 1, layer 11 did not reach the MC profile until 2.5 seconds when its composition started to move toward MC composition, and layer 10 first reaches the MC profile at 0.6 s before the composition increased again. The overall profile, nonetheless, clearly shows an increase in the number of Ni atoms in bulk layers, indicating thermodynamic tendency for this dopant to remain in the bulk rather than on the surface. The state space exploration from KMC is inherently much greater than that of MC, which is not a dynamical method and can only follow an unphysical trajectory towards the lowest system energy.

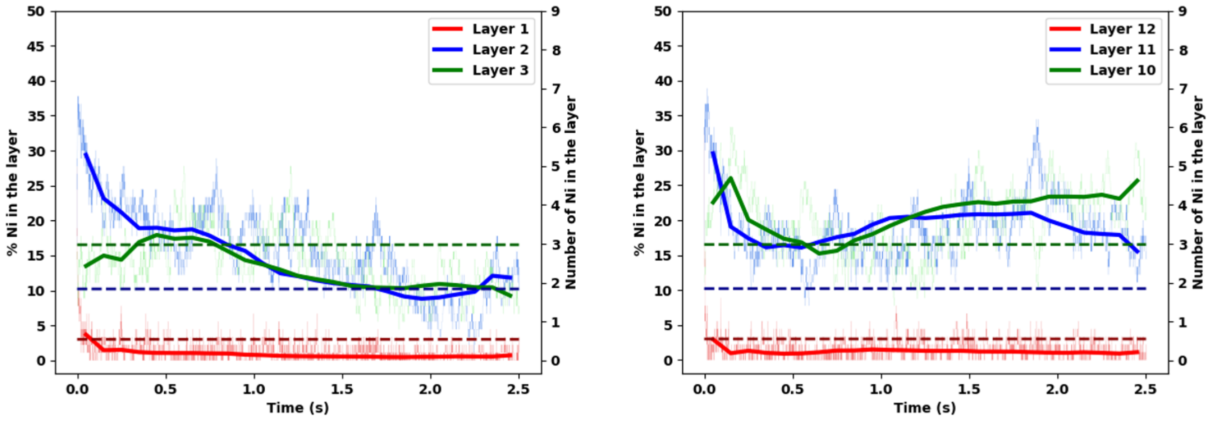

(a) (b)

Figure 7: Ni composition averaged over five KMC simulations for the (a) bottom three layers and (b) top three layers over 2.5 seconds with an equilibrium rate of 40/µs. The bold line represents the 0.5-second-average calculated from the lighter single-frame datapoints, and the dashed line corresponds to the average concentration of Ni by MC calculation with EAM potential at each layer when the system moves toward equilibrium. Composition is normalized as in Figure 2

3.2.2 Monovacancy Activation Energy and State Residence

Apart from surface effects, the local chemical environment around a vacancy is expected to influence the system energetics and the rate of Ni composition change. To investigate this, we tracked the number of Ni atoms within a 5 Å radius of the vacancy. The number of Ni atoms in the local environment ranges from 0 to 12, with three distinct "bins" of equal width formed for low, mixed, and high Ni-content environments.

The spectrum of barriers calculated during AKMC for all vacancy migration events within this trajectory is presented as a histogram in Figure 8a, which shows the lowest transition state energies for vacancy migration in Ni-rich regions of the alloy. Additionally, because the system has lower Ni content than Cu, the integrated peak area is smaller for transitions into/within Ni-rich regions than for those with mixed and Cu-rich compositions. Vacancy migration energies are shifted closer to 0.4 eV in the Ni-rich regions than for migration in Cu-rich regions according to Figure 8a. We can deduce that vacancy migration is favored in the Ni-rich regions, contributing to the lower dwell time near Ni as the vacancy more rapidly diffuses towards and away from this dopant. Vacancies must slowly explore the Cu-rich regions of the host lattice before returning to possibly segregate the Ni atoms away from the surface. The order of integrated peak areas in Figure 8a also supports this conclusion.

The overall time spent in low Ni, mixed, and high Ni content environments is also shown with respect to time in Figure 8b-d using a cumulative measure of residence time for MD, ParSplice, and AKMC and re-scaling this measure by the prevalence of each environment in the system. The number of Ni atoms in the vicinity of the vacancy modulates these timescales substantially but in similar fashion for all methods. Further, the logarithmic trendlines and their orders of magnitude agree across overlapping timescales for MD/ParSplice (ns) and ParSplice/AKMC (µs): this supports the hierarchy of methods utilized herein as a theoretical foundation to connect correlated observations evolving across many timescales for the same process. The cumulative dwell time and thermodynamic trends match for all of the simulation methods in the order of integrated peak areas (Figure 8a) and residence times (Figure 8b-d): $t^{total}_{Cu-rich} > t^{total}_{mixed} > t^{total}_{Ni-rich}$. Though this agreement does not hold at very

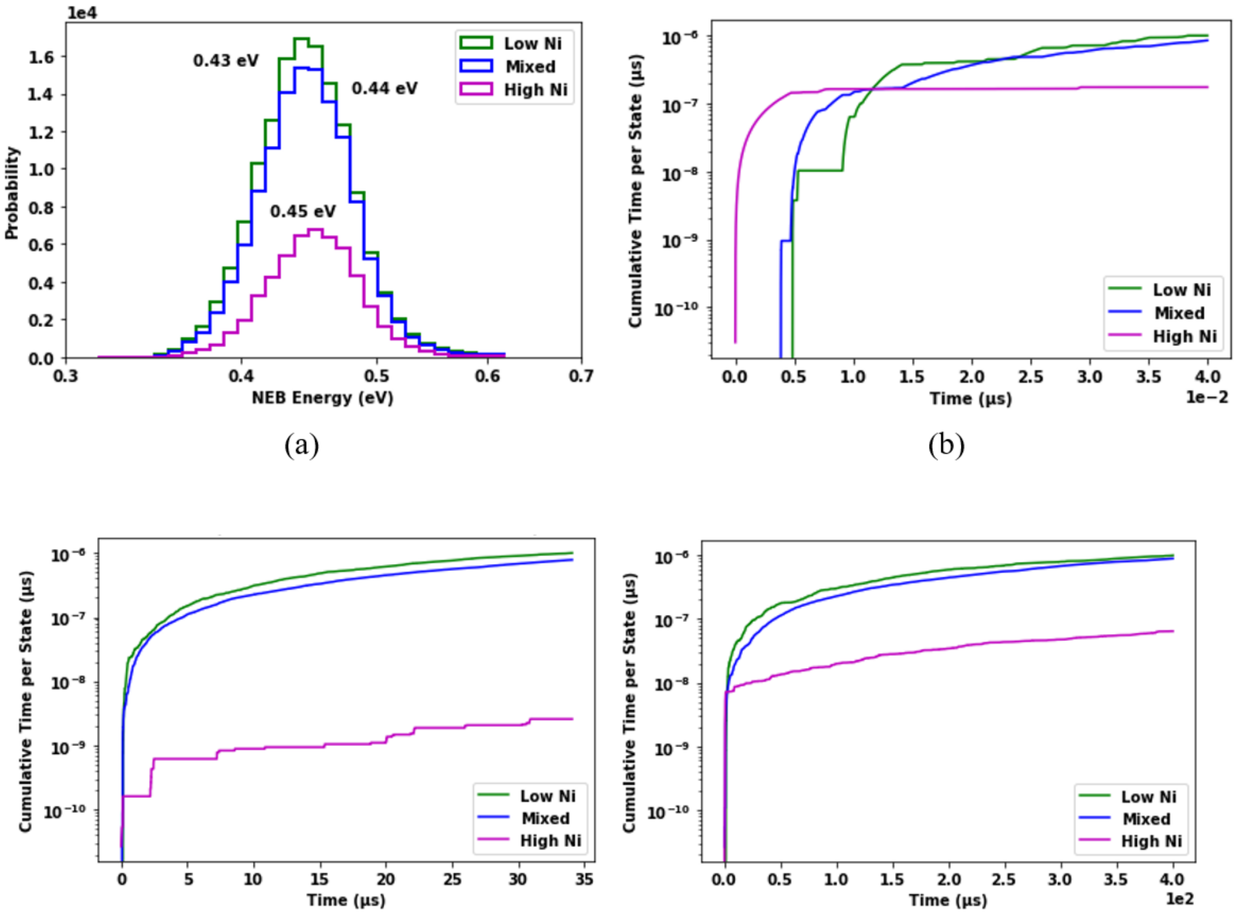

(a) (b)

(c) (d)

Figure 8: (a) Histogram of vacancy migration energy barriers obtained from a 319 μs AKMC simulation. (b-d) Total residence time for the vacancy in different chemical environments for (b) MD, (c) ParSplice, and (d) AKMC. Cumulative times are normalized by the prevalence of each composition type in the system rendering them unphysical.

early (ps) simulation times with low cumulative sums, particularly for MD which is noisier as compared to accelerated methods, the trend becomes evident in the ergodic limit.

The residence times of vacancy chemical environment presented in Figure 8b-d confirm that the local composition is an effective determinant of where a vacancy spends most of its time during annealing and segregation. Specifically, the position of Ni in the lattice is a minor determinant of the dynamics, since the dopant slightly biases the vacancy's random walk by ∼0.1 eV. This effect has also been documented in Ni-Fe surfaces annealed at 1100 K using KMC, where the local composition and the identity of the atoms exchanging during segregation (solute vs. solvent) significantly influenced the vacancy migration energy and the measured tracer diffusion coefficient[32].

3.2.3 Divacancy Activation Energy and State Residence

It is known that this combination of two vacancies is more stable than two point defects in isolation: the predicted stability of the divacancy decreases in order of 1^{st} NN $>$ 2^{nd} NN $>$ 3^{rd} NN according to previous calculations and our own[6, 71]. Accordingly, we created an alloy with a known initial divacancy location and separation (3rd and 5th layers, 3^{rd} NN separation distance) and binned the distance between two vacancies within the periodic simulation cell into 1^{st}, 2^{nd}, 3^{rd}, 4^{th} and $\geq 5^{\text{th}}$ NN groups (2.56, 3.62, 4.43, 5.12, and all distances ≥5.72 Å, respectively) to characterize the divacancy state. We used Wigner-Seitz analysis to track the divacancy separation distance throughout conventional and accelerated trajectories shown in Figure 9.

The mono- and divacancy are respectively distinguished as red and blue peaks within the overall spectrum of barriers for an entire AKMC simulation in Figure 9a. This histogram represents 400 µs of annealing with vacancies mostly trapped on the surface for the duration (only ∼6 at% change in local composition occurs in the top layer). Using the divacancy NN separation distance, we can easily differentiate the largest peaks in the activation barrier spectrum as the migration of a single point defect (0.52 eV) or the rotation of the point defect about the center of a coupled divacancy (low-energy peak, 0.22 eV). These two energies represent energy distributions of mono- and divacancy migration in our structures characterized by the $4^{\text{th}}/5^{\text{th}}$ and 1^{st} NN distances between the divacancy, respectively. The peak around 0.52 eV in Figure 9a for independent migration of distant monovacancies resembles the distribution shown in Figure 8a, which shows the thermodynamics for a system with one vacancy.

The peak areas for each NN separation distance of the divacancy also correspond to the

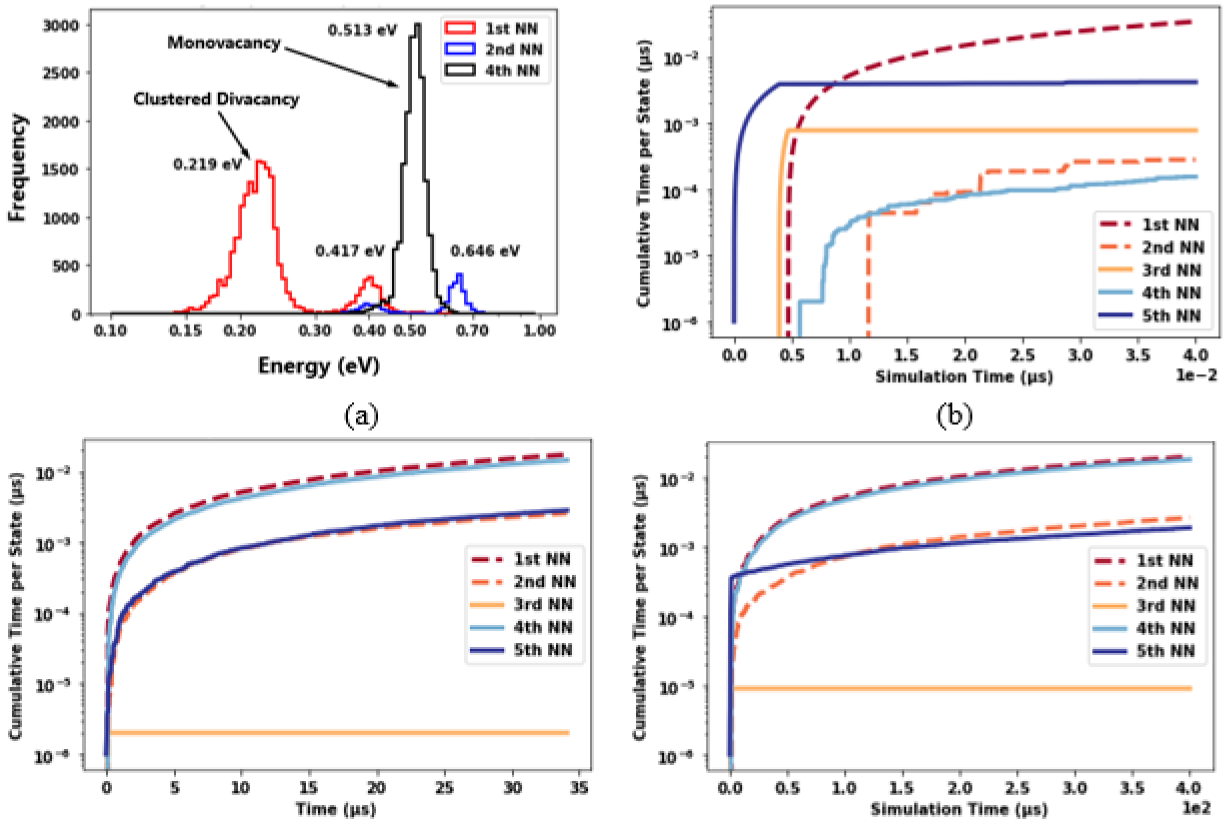

(a) (b)

(c) (d)

Figure 9: (a) Histogram of divacancy migration energy barriers obtained from a 400 s AKMC simulation. (b-d) Total residence time for each divacancy separation distance for (b) MD, (c) ParSplice, and (d) AKMC. Cumulative times are normalized by the prevalence of each composition type in the system rendering them unphysical.

values of trendlines in Figure 9b-d as well, agreeing on the expected order of dwell times in each of the five divacancy separation states. The most visited states—the 1st and 4$^{\text{th}}$ NN separation distances—are energetically similar because the divacancy formation energy is only slightly (∼0.1 eV) smaller than that required to form two isolated vacancies in both Cu and Ni crystals[71, 116]. Accordingly, the 2$^{\text{nd}}$ and 5$^{\text{th}}$ NN distances are also revisited at similar rates in accelerated MD (Figures 8b and 3c), but since these states adjoin the 1$^{\text{st}}$ or 4$^{\text{th}}$ NN states, respectively representing a destabilized divacancy or two isolated monovacancies, they occur with less overall probability. Fast planar clustering on the order of 10^1-10^2 ns brings the vacancies together such that the 3^{rd} NN divacancy separation, though initially introduced at this distance, is not measurably revisited in the dynamics. Higher resolution simulations with ps and fs frames printed to our data pipeline showed the same result, so we conclude that the absence of transitions into the 3^{rd} NN state (Figure 9a) or revisiting in cumulative timescale plots (Figure 9b-d) is not an artifact of our methodology.

The competition between divacancy formation and vertical migration to the surface for individual vacancies biases the random walks of point defects in proximity to one another in the lattice. In our alloy systems with two atoms deleted (2 vacancies introduced), a rapid clustering of the vacancies into a single void consistently occurred in less than 20 ns for nearly all simulations. Because of the favorable clustering of monovacancies into divacancies, planar defect diffusion is not random but instead biased towards formation of grouped defects (see Appendix A.4)[6, 71, 81]. We expect to see stochasticity from the random walks of isolated vacancies to cause lasting separation of some pairs, since we simulated fifty different trajectories in total with the methods (except KMC, due to its applied equilibrium rate and inability to model the divacancy). Despite this, only three trajectories with a divacancy did not contain the clustered divacancy on a single surface after 400 ns.

Particularly, from the analysis of the trajectory, we can see that the divacancy rotates and rapidly ascends to the exposed surface of the alloy, since its migration energy is much lower than that of a single vacancy (Figure 9a)[6, 71, 81]. Rotation of the divacancy by 60° within close-packed <111> planes has been previously confirmed with first-principles and EAM NEB calculations for both Cu and Ni, though the rotation path is slightly out of plane in the case of pure Ni[6, 71]. We also observed this mechanism through analysis of vacancy coordinates from Wigner-Seitz analysis, a finding that reinforces our earlier statement: the position of Ni in the lattice is a minor determinant of the dynamics, since the dopant slightly biases the vacancy's random walk by ~0.1 eV.

3.3 Cross-Correlation Heatmaps for Divacancy Segregation Mechanism

As discussed in Section 2.6, trajectory correlation analysis can be performed to compare the path of a vacancy with a counter-migrating Ni atom during a segregation event. We have shown that the divacancy mechanism should dominate the dynamics based on its formation and migration energies relative to those for the monovacancy(Section 3.2.3 and Appendix A.4). In previous literature, a 60° divacancy rotation within 111 planes has been shown to occur in both Cu and Ni using DFT and EAM to calculate activation barriers previously [6], though the rotation path is slightly out-of-plane in the case of pure Ni[71]. To confirm this mechanism occurs similarly during divacancy segregation in our own simulations, I carried out windowed cross-correlation analysis between one of the vacancies in the pair and the counter-migrating Ni atom of interest. The resulting heatmaps in Figure 10 were developed from trajectories made by conventional MD (a), ParSplice (b), and AKMC (c). The timing of divacancy exchange is very different between each simulation method, since AKMC does not have a constant timestep (the bins in the third row do not represent equal time, nor does the offset τ). ParSplice has a constant time step, bin size, and offset, but covers a much greater timespan than standard MD can. Thus, the short pattern in row 1 (MD) reoccurs as a fractal within the longer ParSplice trajectory containing multiple segregation events.

In summary, the multiscale acceleration framework of MD, ParSplice, AKMC, and KMC with added equilibration rate have increased the segregation trajectory timescale from nanoseconds to full seconds, allowing for direct comparison with experimental data captured during annealing. The latter two simulation methods are highly scaleable, with the primary computation bottleneck occurring in ParSplice, since many replicas are required to be simulated at once with only small gains from topology matching for the spherically asymmetric slab. In future, KMC-based methods in combination with novel potentials will allow for comparison of oxidation experiments with computational simulation, revealing the initiation and growth of oxides on realistic timescales by closing the gap between experiment and theory.

The trajectory analysis method of cross-correlation heatmapping allows for multiple segregation mechanisms to be identified which depend on the local density of defects i.e. mono-

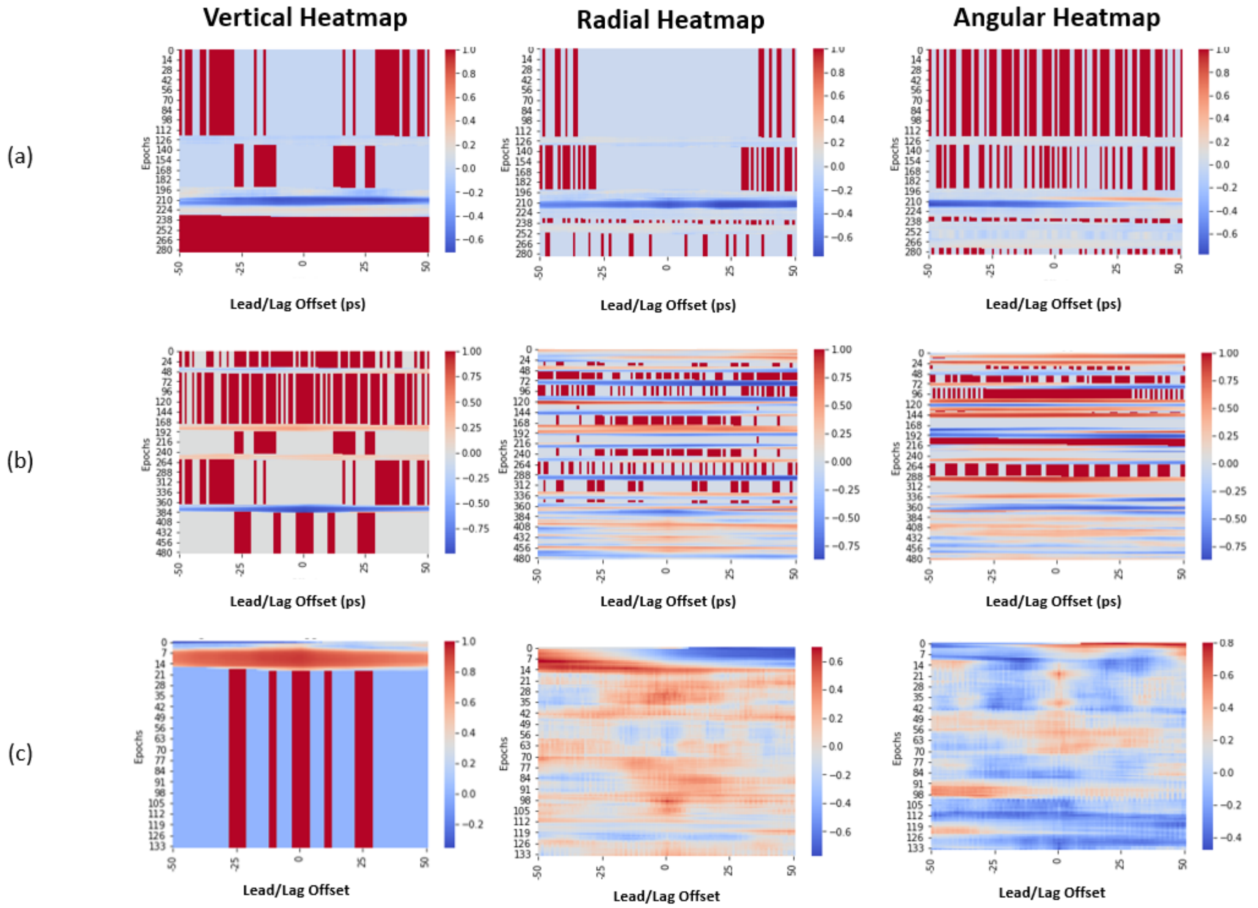

Figure 10: Rolling window cross-correlation heatmap comparing cylindrical coordinates z (first column), r (second column), and θ (third column) for a segregating Ni atom (negative offset) and a counter-migrating vacancy (positive offset). Trajectories from conventional MD (a), ParSplice (b), and AKMC (c) are shown. Time is binned in epochs on the vertical axis while time offset τ is on the horizontal axis. Solid red bands denote a numerical error filled with the default value($\rho = 1$).

vacancy vs. divacancy segregation. The divacancy segregation mechanism entails a rotation through 111 planes which occurs much more rapidly than the simpler monovacancy migration in [100] direction. There is a small influence of chemical environment on the vacancy migration rate as well, with Cu-rich regions showing slower vacancy diffusion than those with high Ni content. In the future, the effect of local composition on vacancy migration should be explored more in stoichiometric alloys which are both disordered and ordered to observe expected influences on monovacancy random walk. Similarly, cross-correlation analysis should be applied to simulations of oxide nucleation and growth to detect novel mechanisms of formation on the alloy substrate, particularly in the presence of roughened surfaces with defects present since oxygen adsorption is more likely in these regions.

4.0 Cu-Ni-O Forcefield Development

It is also important to simulate the effect of oxidation on the alloy segregation, since it is known from experiments that the competition between NiO and Cu_2O will induce phase separation trends that can invert the trend expected from vacuum surface tension. Key intermediates in the alloy surface oxidation consist of surface reconstructions under varying oxygen surface coverages. These stable surface arrangements of adsorbed oxygen create rows of adatoms on the (100) surface, creating corrugated rows similar to those seen on (110)[64, 62]. This surface roughening increases the number of hollow sites available for oxygen adsorption, which we determined to be the most favorable adsorption site based on a series of DFT surface energy calculations comparing the position of oxygen on CuNi surfaces.

After identifying important trends in oxide formation and nucleation on the reconstructed surfaces for pure Ni and alloyed CuNi with this first-principles data, the same values were used as training data for reactive force field (ReaxFF) optimization. In addition to the formation and surface energies presented in the following section (4.1), relative energy differences, per-atom forces, and interatomic distances were also incorporated into the training data from the available DFT calculations, expanding the number of training samples to 310.

4.1 Results: Surface Alloy Oxide Stability from First-Principles

The formation energy of surface oxides can also be compared for various oxygen coverages θ_O to evaluate the thermodynamic stability of differing surface reconstructions and oxides. The following formula can be used to find the formation energy of $\mathrm{Ni_{(1\text{-}x)}O_x}$ on the top layer of a Ni(100) substrate:

$$E_{form}(x) = E_{Ni,s+Ni_{(1-x)}O_x} - E_{Ni,s} - (1-x)N_{MS}E_{Ni} - \frac{xN_{OS}E_{O_2}}{2} \tag{4.1}$$

where $E_{Ni,s+Ni_{(1-x)}O_x}$ is the energy of the relaxed substrate with formed oxide layer on top, $E_{Ni,s}$ is the relaxed substrate energy with the top, reconstructed layer removed, E_{Ni} is the per-atom reference energy for bulk Ni, E_{O_2} , N_{MS} is the number of metal sites per layer (4-8 depending on periodicity), and N_{OS} is the number of available hollow sites on the surface for oxygen adsorption.

For a set of pristine Ni(100) surfaces with adsorbed oxygen and also reconstructed (100) surfaces with an oxygen coverage $0 < \theta_O < 1$, I calculated the formation energies of the surface oxides relative to the bare (100) substrate, presenting them as a convex hull in Figure 11. The most stable surface reconstruction is characterized by a c(2 x 2) surface arrangement. Because formation energies increase beyond this critical coverage $\theta_O = 0.5$, it is clear that oxide nucleation and growth atop the c(2 x 2) reconstruction will initiate as more oxygen adsorbs at the surface. This behavior occurs in lieu of forming a complete oxygen monolayer ($\theta_O = 1$). Importantly, the formation energy for $\theta_O = 1$ represents one layer of stoichiometric NiO, and does not follow the trend line. This is because developed oxide formation is preferred accompanied by surface roughening: the unaltered surface in the structure of $\theta_O = 1$ represents a lattice spacing closer to that of pure Ni (a = 3.52 Å) rather than NiO (a = 4.25 Å), so it remains less stable than the c(2 x 2) reconstruction which maintains a spacing closer to the oxide's equilibrium value.

I constructed a similar convex hull for the various alloy surface oxides $Cu_{(1-x)}Ni_xO_y$ atop the pristine Cu(100) substrate. The necessary equation is similar to (4.1):

$$E_{form}(x,y) = E_{CuNi,s+Cu_xNi_{(1-x)}O_y} - E_{CuNi,s} - xN_{MS}E_{Cu} - (1-x)N_{MS}E_{Ni} - \frac{xN_{OS}E_{O_2}}{2} \tag{4.2}$$

The formation energies of surface oxides for both pure and alloyed cases can be compared in this manner, not only revealing the highest coverage θ_O beyond which oxide nucleation occurs, but also the influence of oxygen on metallic surface segregation. Figure 12 shows the convex hull for a variety of formed alloy oxides $Cu_{(1-x)}Ni_xO_y$ which I use in the training for ReaxFF and my advisor, Saidi, used in the training for DeepPot.

The formation energies are presented as a function of Ni content (x) as well as the oxygen content (y). Clearly, low oxygen content around $\theta_O = 0.125$ is thermodynamically preferred

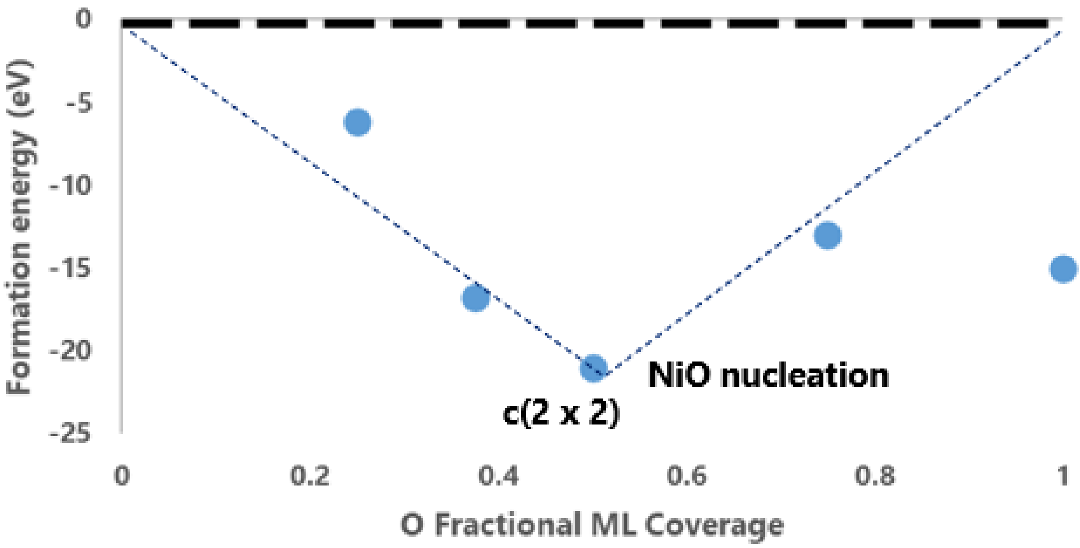

Figure 11: Convex hull of surface $Ni_{(1\text{-}x)}O_x$ formed on the pristine Ni(100) substrate for both monolayers and reconstructed surfaces.

above all other values for θ_O, indicating that the initiation of oxide growth proceeds before further adsorption of oxygen. As θ_O approaches 1 (a full monolayer), some stability is gained, since this creates a thin, developed oxide along the top layer. Additionally, surface oxides with Ni in the subsurface rather than the exposed surface tend to be more stable, as expected from the known influence of surface tension (dashed lines in Figure 12 highlight this behavior).

Surface reconstruction roughens the surface, providing more sites for oxygen adsorption at the lower coordination edges, kinks, and vertices. A variety of defective structures which do not contain a pristine (100) surface were also relaxed with adsorbed oxygen using DFT, allowing θ_O to reach 1.25 ML, since the defective surfaces contain more adsorption sites than are normally available on their pristine counterparts. Another set of convex hulls for $0.125 < \theta_O < 1.25$ is plotted for the full dataset in Figure 13, including defective, reconstructed surfaces which differ significantly from (100).

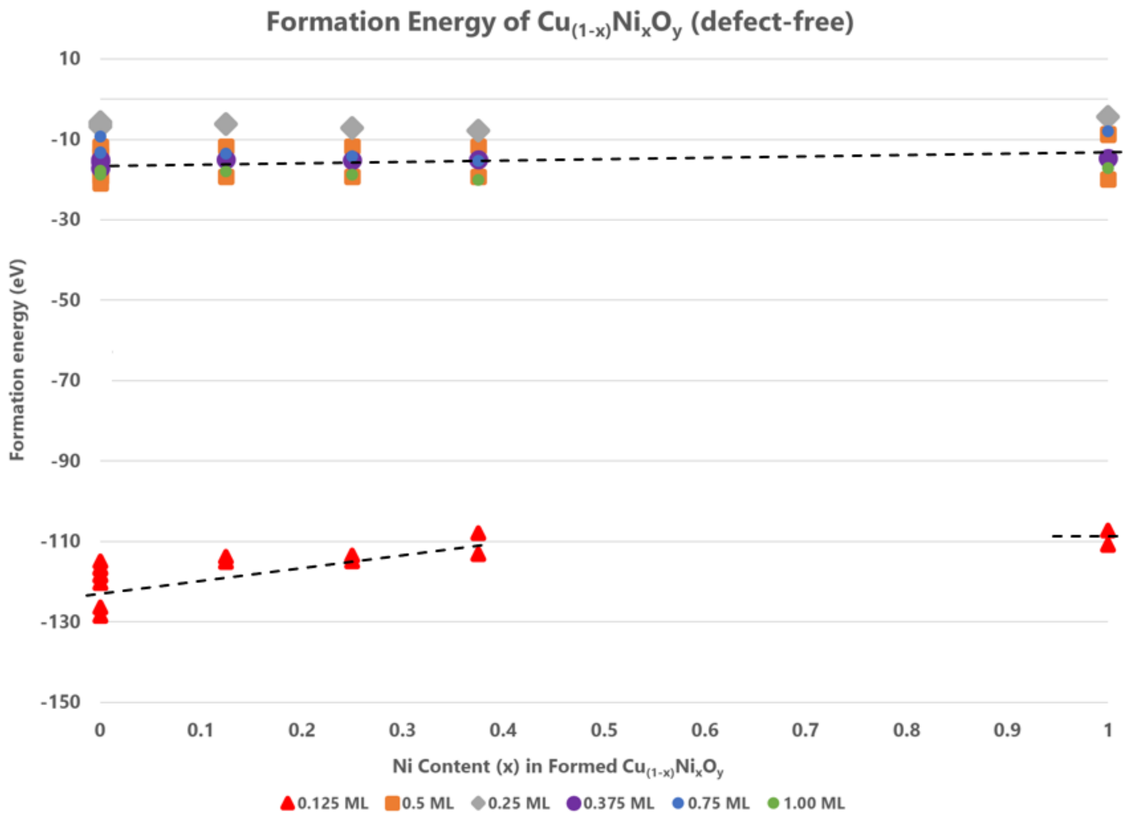

Figure 12: Convex hull of surface $Cu_{(1\text{-}x)}Ni_xO_y$ formed on the pristine $Cu_{(1\text{-}x)}Ni_x$(100) substrate for monolayers and some reconstructed surfaces. Dashed lines highlight differences in formation energy for equivalent values of x caused by Ni positioned in the surface (above the line) or subsurface (below the line).

Interestingly, for defective surfaces, the metallic segregation trend inverts: Ni prefers to be on the surface, part of the formed oxide. This is likely due to the structural inability to reduce surface tension in the presence of defects. Nearly all surfaces with defects have $E_{form} > 0$, falling outside the convex hull relative to the pristine (100) surface. Importantly, defective surfaces with $\theta_O = 1.25$ are all found to be more stable than the unoxidized, pristine surface ($E_{form} < 0$). This is because the oxide formation energy is greater than the segregation energy, which only relaxes surface tension rather than forming new bonds. In other words, the formation of nickel oxide is so favorable it overwhelms the thermodynamic

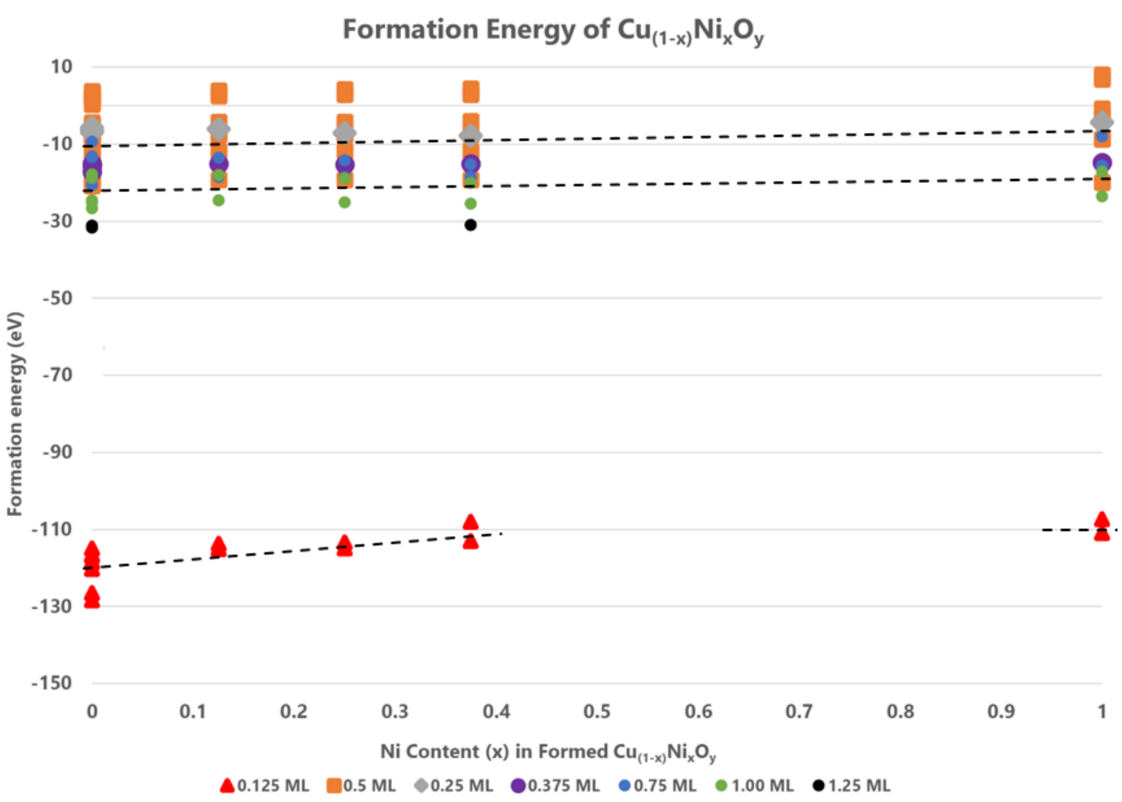

Figure 13: Convex hull of surface $\mathrm{Cu_{(1\text{-}x)}Ni_xO_y}$ formed on the pristine $\mathrm{Cu_{(1\text{-}x)}Ni_x}$(100) substrate for monolayers and some reconstructed surfaces. Dashed lines highlight differences in formation energy for equivalent values of x caused by Ni positioned in the surface (above the line) or subsurface (below the line).

tendency for Ni to be in the bulk.

The case with high surface defect density is likely to represent the realistic CuNi surface as it transiently oxidizes, since it is known that surface defects present favorable adsorption sites for oxygen gas. The inversion of expected surface segregation trends as oxygen roughens the surface explains the competitive oxidation of CuNi at the atomic and nanoscales. Locally, NiO can form before Cu_2O in the presence of roughened surfaces and inhomogeneous alloy composition caused by pre-annealing.

4.2 ReaxFF: Reactive Forcefields

The ReaxFF model is based on a bond order formalism, but also uses bond distance to determine further effects such as Coulomb and van der Waals forces[100]. Updates to bond order and distance allow for bonds to be dynamically formed and broken during simulation, and distinct atom types include lone pairs and more electronic effects such as shielding. All of these effects are handled at once by the embedding function of EAM, making it a less performative model than ReaxFF. For instance, EAM requires significant alterations to describe interactions with oxygen, which behaves fundamentally different than the metallic nuclei. To date, there is no applicable force field of any model which describes molecular oxygen and its reactions with solid, alloyed CuNi surfaces. For this reason, I developed a novel reactive potential for Cu-Ni-O using the ReaxFF formalism and an evolutionary algorithm, particle swarm optimization, from my own first-principles database describing the surface oxidation of CuNi.

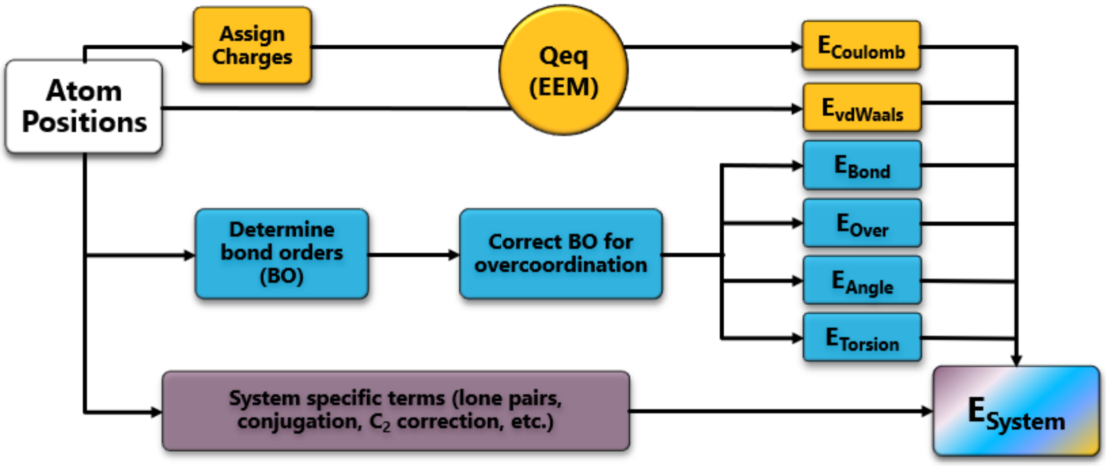

Figure 14: Diagram of energetic contributions to the total system energy from each atom, reproduced from [90]

There are atomic, two-body, three-body, and four-body interaction terms as well as off-diagonal two-body interaction terms within the ReaxFF model. To minimize alteration of pre-existing forcefields, we only re-optimized the two-body and three-body interaction terms. Specifically, the bond dissociation energy (*Edis1*), σ and π bond order pre-factors (*pbe1* and *pbe2*) and their related exponents (*pbo1*, *pbo2*, *pbo3*, *pbo5*, and *pbo6*) were varied. Off-diagonal terms (*Ediss*, *Ro*, *gamma*, and *rsigma*) were also varied to further improve performance. The free parameters include the self-interactions for Ni-Ni and O-O, which were both re-optimized to improve the existing Ni-O potential from van Duin et al[122]. In total, 44 two-body interaction parameters were allowed to vary during the Cu-Ni-O forcefield optimization, although 32 of these were optimized separately to create the Ni-O potential first. The three-body parameters for Cu-O interactions were held constant while 20 parameters were relaxed for the Ni-O three-body interactions. We benefit from a previously optimized Cu-O potential developed within our own lab group[121], necessitating only minor rescaling of two-body interactions with our improved Ni-O parameters to realize a viable Cu-Ni-O potential.

4.2.1 Particle Swarm Optimization

The algorithm used for development of ReaxFF potentials in this work is particle swarm optimization (PSO), an evolutionary or genetic method which explores multiple candidate potentials at once. It is publicly available at github.com/tisimst/pyswarm Information is shared between the candidate "particles" or force fields in the group, or "swarm". Information passing is a key feature of all evolutionary methods. PSO improves the force field parameters of each particle using the best performing parameter set: the current best force field $P_{best}(t)$ pulls the other candidates' parameters $\mathbf{P}_i(t)$ closer to its own parameters through a velocity update, creating a new swarm $\mathbf{P}$(t+1):

$$\begin{aligned} \mathbf{V}_i(t+1) &= \omega \mathbf{V}_i(t) + c_1 r_1 (P_{best} - \mathbf{P}_i(t)) \\ \mathbf{P}_i(t+1) &= \mathbf{P}_i(t) + \mathbf{V}_i(t+1) \end{aligned} \tag{4.3}$$

where $\mathbf{V}_i$ is the velocity vector for parameters belonging to candidate i. The weights c_1 and r_1 are selected by the user to determine the level of information passing from the best candidate to all others. Larger values indicate a bias towards exploitation of the best parameters in lieu of exploration for new potential candidates. This tunable approach allows for many more candidates to be tested than the typical Gaussian perturbation, which has been used in the literature for decades to create new ReaxFF parameter sets without exploring as many possibilities in parameter space. The moduler (object-oriented) code I developed for this study is publicly available at `github.com/15garzab/pso_rff`, building on a previous, functional optimization code driven by Gaussian perturbation written by Matt Curnan[121].

4.3 Results: ReaxFF for Ni and Ni-O

In order to better model surface nickel oxides, we first improved the performance of a pre-existing Ni-O ReaxFF potential available in the literature and trained using the same density functional ground-truth as in our own optimization[122]. These parameters were originally developed to describe bulk oxides rather than oxides formed on the exposed surface, justifying further improvement with PSO. Figure 15 shows the performance of the original potential for a variety of surface oxygen coverages of the Ni(100) surface as well as bulk Ni and NiO in face-centered cubic (FCC) and hexagonal close-packed (HCP) lattices.

This potential shows significant deviation from ground-truth data for the surface oxides and bulk oxides. It is expected for surface oxide species to be poorly modeled by this potential because our training structures were not used in its development, which focused on bulk properties.

However, the performance for bulk oxides is also poor even though the lattice parameter is correctly predicted, a fact which is obvious when examining the binding energy curves (Figures 16 and 17) for bulk NiO, which have root mean squared error (RMSE) greater than 5 eV. These plots document the lattice formation energy as a function of deviation (expansion/compression) away from the expected lattice parameter($a = c = 4.2$ Å).

Our re-optimization using PSO closes the gap between DFT and previous RFF performance, reducing the overall RMSE across the data for nickel and its oxides from 4.57 eV to 3.60 eV. The parity plot for the improved Ni-O forcefield and all relevant data is shown in Figure 18.

The majority of this performance enhancement comes from the bulk and surface nickel

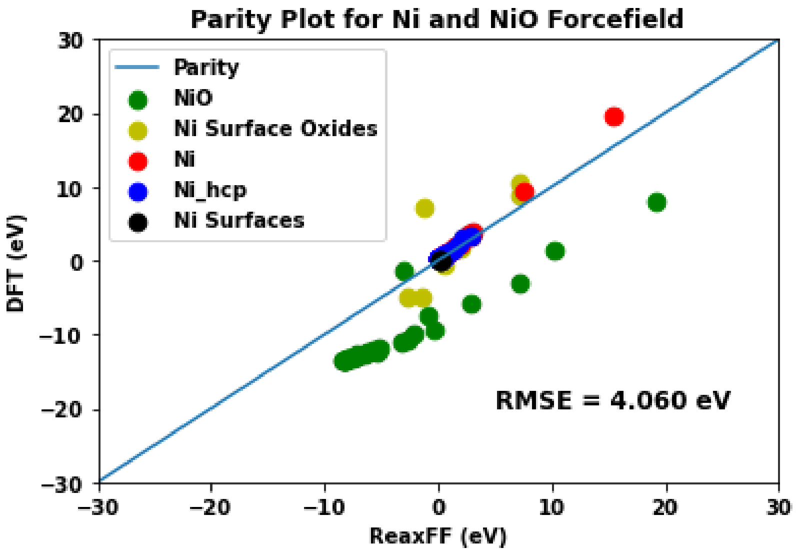

Figure 15: Parity plot comparing surface, bulk formation, and binding energies of Ni and NiO from the original Ni-O RFF [122] with their ground-truth DFT values

oxide binding energies, as shown in Figures 19 and 20. The improved potential not only predicts the correct lattice parameter ($a = c = 4.2$ Å), but also matches the functional dependence of formation energy on lattice expansion and compression. RMSE for bulk, FCC NiO binding energies dropped from 6-8 eV (planar vs. vertical binding) for the original parameters to 1-2 eV.

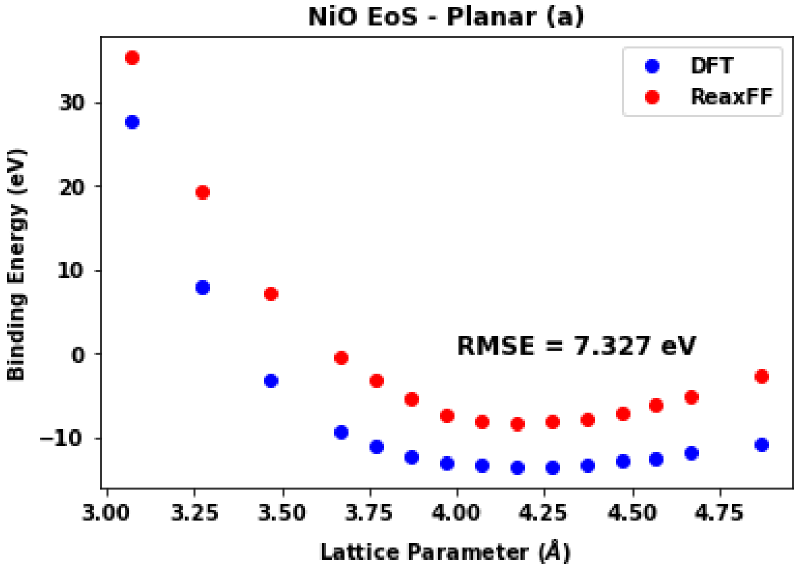

Figure 16: Binding energy as a function of planar lattice parameter (a) for FCC NiO calculated with outputs from the original Ni-O RFF parameters[122]

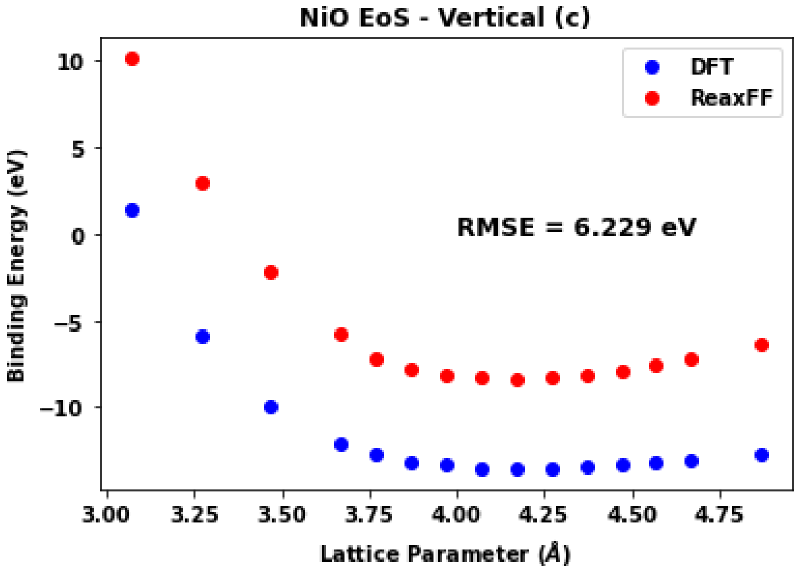

Figure 17: Binding energy as a function of vertical lattice parameter (c) for FCC NiO calculated with outputs from the original Ni-O RFF parameters[122]

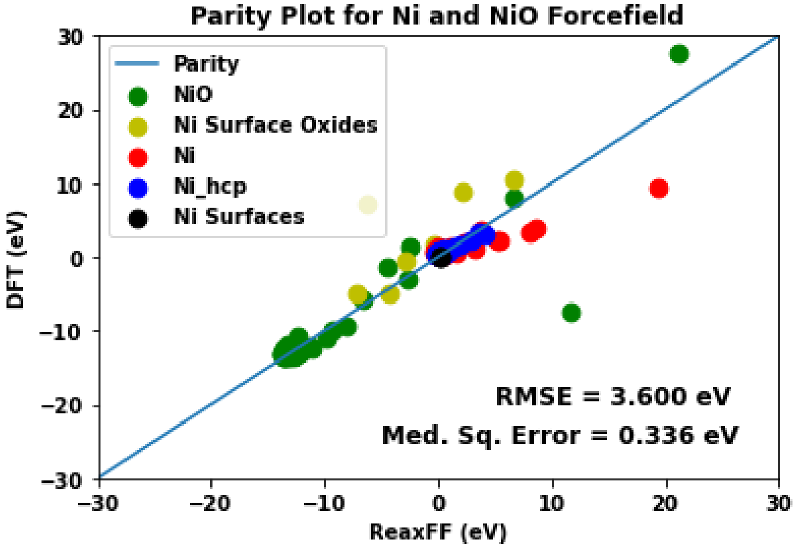

Figure 18: Parity plot comparing surface, bulk formation, and binding energies of Ni and NiO from the improved Ni-O RFF with their ground-truth DFT values

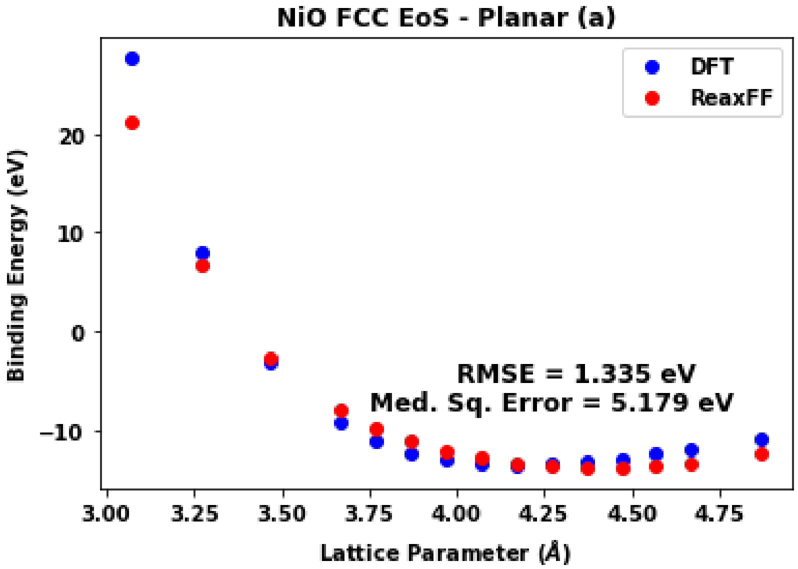

Figure 19: Binding energy as a function of planar lattice parameter (a) for FCC NiO calculated with outputs from the improved Ni-O RFF parameters

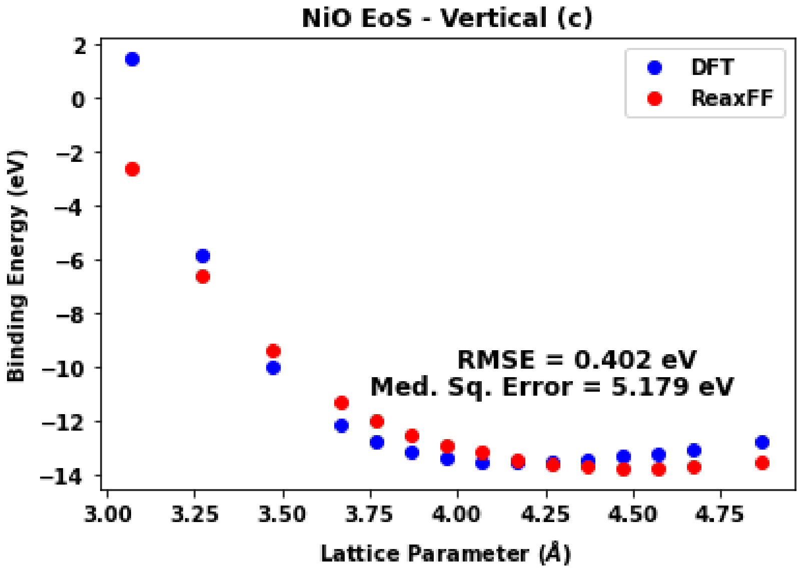

Figure 20: Binding energy as a function of planar lattice parameter (c) for FCC NiO calculated with outputs from the improved Ni-O RFF parameters

4.4 Results: ReaxFF for Cu-Ni-O Surfaces

After Ni-O parameters were improved beyond their previous performance, we re-scaled the Cu-O parameters alongside those for Ni-O to create the new Cu-Ni-O ReaxFF potential, the first of its kind to the best of our knowledge. The overall performance of the Cu-Ni-O RFF potential is shown in Figure 21: RMSE is below 7 eV for the full training set, exhibiting excellent performance for oxides on pure metal and alloyed surfaces.

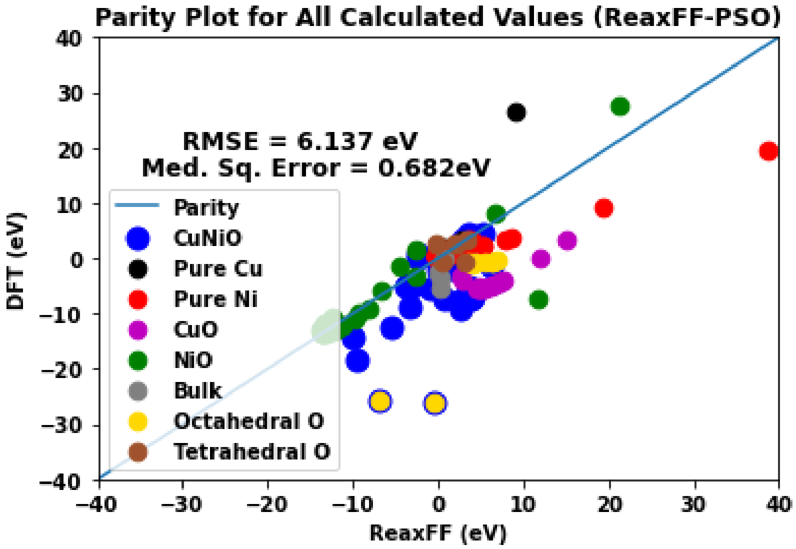

Figure 21: Parity plot comparing surface, bulk formation, and binding energies of Cu, Ni, CuO, NiO, CuNi, and surface alloy oxides from the final ReaxFF Cu-Ni-O potential with ground-truth DFT values

Inserting oxygen at octahedral and tetrahedral interstitial sites results in excited states (oxygen flow through the lattice preferentially follows along dislocations and lattice defects rather than the much smaller interstices), so benchmark structures for bulk alloys with oxygen inserted at interstitial positions are difficult to relax using not only DFT but any developed potentials. It is likely that four-body interactions will need to be re-optimized to account for the high degree of oxygen coordination at interstitial positions in the bulk lattice. Such development is beyond the scope of this work, which is focused primarily on surface and subsurface oxygen interactions.

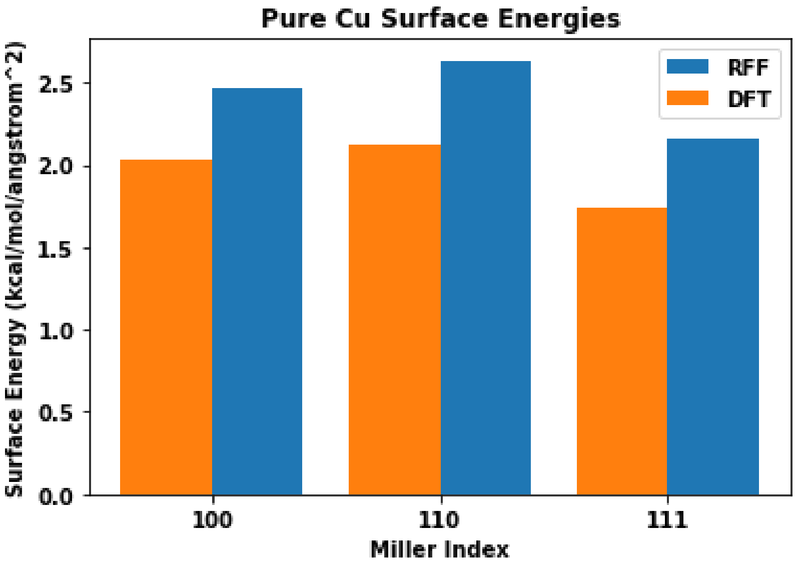

Figure 22: Surface energies from final ReaxFF Cu-Ni-O potential and first-principles ground truth for pure Cu surfaces

Close matches with first-principles binding energy curves for the pure metals Cu and Ni and are also provided by the final Cu-Ni-O potential for both FCC and HCP lattices. Average RMSE for these values is below 1 eV as shown in the binding energy curves provided in Appendix A.7.1 and A.7.2. Additionally, the ReaxFF potential replicates the order of surface energies from DFT for pure Cu (Figure 22) and Ni-doped Cu surfaces (Appendix section A.7.4) with low Miller index i.e. $E^{surf}_{Cu(111)} < E^{surf}_{Cu(100)} < E^{surf}_{Cu(110)}$. Further, the same behavior is exhibited for pure Ni and alloyed surfaces. Energy differences between structures with Ni on the surface, subsurface (2^{nd}), and interior (3rd)in the surface were included in the training to account for vacuum surface segregation previously described in 2. Trends for each of these cases are shown in Appendix section A.7.4.

Various oxygen coverages $0 < \theta_O < 1$ on the (100) surface were used as training structures with Ni doping in the surface, subsurface, and interior layers. As previously noted in 4.1, some of these structures are oxides formed on pristine (100) surfaces. Figure 23 displays good performance of the ReaxFF potential developed with PSO for surface alloy oxides without

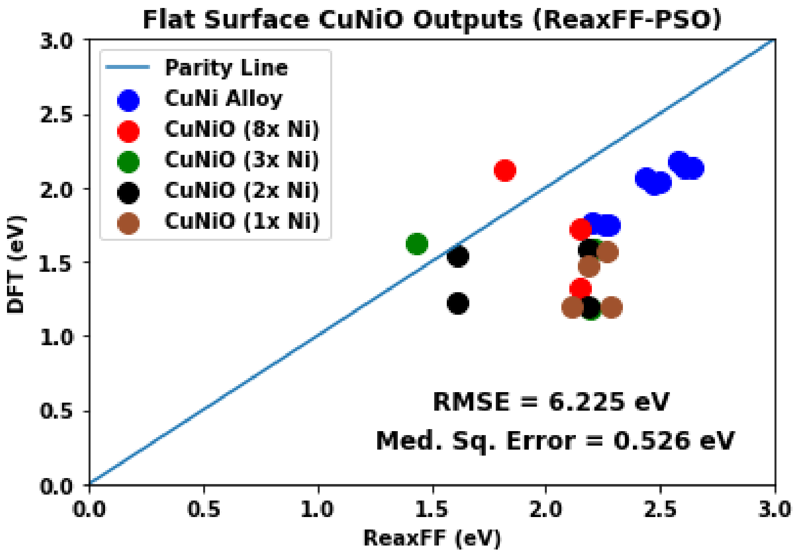

Figure 23: Parity plot comparing surface energies of pristine surface alloy oxides from the final ReaxFF Cu-Ni-O potential with ground-truth DFT values

defects (RMSE < 7 eV).

Further, the potential also performs well for reconstructed surfaces containing corrugated rows and other defects deviating from the pristine (100) surfaces of Figure 23. RMSE < 8 eV is shown in Figure 24 for these reconstructed surface oxides.

In the future, it will be essential to retrain this model with (110) and (111) surface reconstructions, although these reconstructions are not as well characterized in the literature[67, 66, 58]. Relaxing further structures with DFT which were not included in our data will be necessary. Such optimization will provide further confidence in the force field's application towards CuNi oxidation studies.

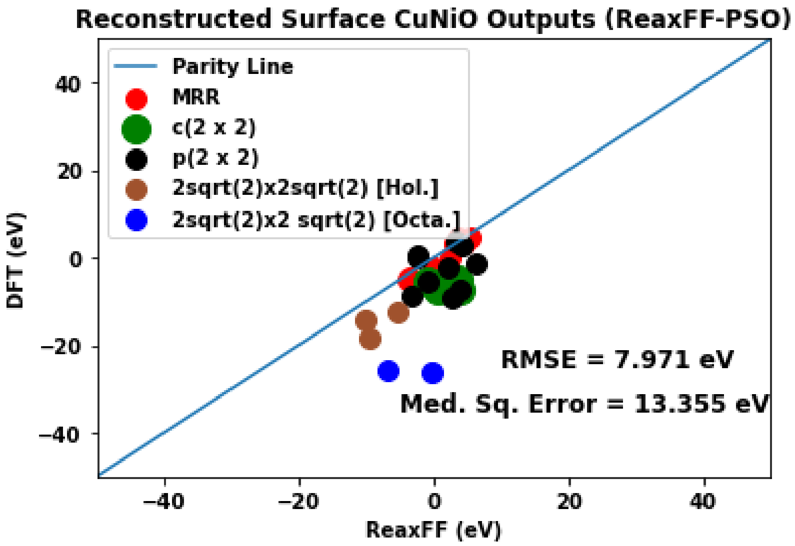

Figure 24: Parity plot comparing surface energies of pristine surface alloy oxides from the final ReaxFF Cu-Ni-O potential with ground-truth DFT values

4.5 DeepMD/DeepPot: Deep Learning of Atomistic Potentials

Although the ReaxFF model is derived from physical intuition and established chemical theories (bond order formalism, VSEPR theory, etc.) and it can appropriately model more than one chemical environment (surface vs. bulk), it is not highly accurate for any particular subsystem except the bulk (RMSE < 2 eV). The trade-off between model parsimony–having few parameters with high transferability–and model accuracy is important to balance. To address the inaccuracies of the developed PSO-RFF model, we also trained a neural network potential with thousands of parameters more than are used in ReaxFF.

DeepMD is a package written in Python and C++ that provides quick access to data loaders and model construction scripts to train a deep learned interatomic potential from energies, forces, and virials sampled from ab initio MD. It relies on Tensorflow for graph embedding of atomic environments in each frame of the dynamics. The output from DeepMD is a DeepPot-Smooth Edition (DeepPot-SE) model which replaces an older, discontinuous potential with appropriately smooth tapering near the cutoffs[117]. DeepPot-SE is extensive and preserves symmetry-invariant properties necessary to model dynamical and mechanical properties of interest in alloy systems via a set of adaptive environmental tensor embeddings and a family of loss functions for the user to select from[117]. After converting the coordinates of the particles into graph representations for more efficient processing, the environmental tensors of each atom within a cutoff radius are created. These local atomic environment tensors are then mapped to an embedded feature space which preserves the translational, rotational, and permutational symmetries of the target system. A final fitting network consists of a fully-connected set of feed-forward layers with skip connections, taking the feature embeddings to atomic energies which are summed to yield the total system energy[117]. Full code for the DeepMD kit is available at `github.com/deepmodeling/deepmd-kit`.

The training data used in the development of DeepPot-SE force fields for Cu-Ni-O interactions are a subset of my PSO-RFF training data, which my advisor (Saidi) selected, omitting Ni and NiO structures. Specifically, we evolved alloy oxide structures in time using ab initio MD to create thousands of samples of atomic forces, virials, and positions. Because only Cu-rich alloys were of interest to my advisor, there was minimal sampling of Ni and NiO trajectories for the input data. Thus, it is expected for the output model to perform poorly on pure Ni and NiO structures. I created all training structures and MD samples; the optimization and training of the neural network was carried out by my advisor, Saidi, one of the developers of the DeepMD kit. I performed all benchmarks and tests of this potential presented in the following section.

4.6 Results: DeepPot for Cu-Ni-O Surfaces

The following plots show the performance of the output DeepPot model for Cu-Ni-O. In particular, there is excellent agreement between DFT and DeepPot for alloy and alloy oxide structures. Overal RMSE is below 12 eV for the entire dataset: this number is inflated since the Ni and NiO bulk expansion/compression structures were not included in the training data. Without these data included in the assessment, RMSE falls to 3 eV26.

Focusing on alloy oxides with pristine, unreconstructed surfaces reveals excellent perfor-

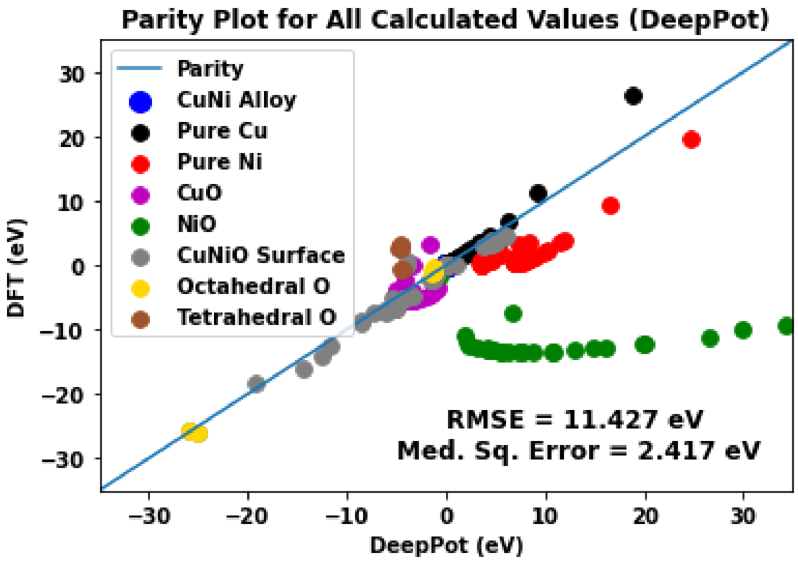

Figure 25: Parity plot comparing surface, bulk formation, and binding energies of Cu, Ni, CuO, NiO, CuNi, and surface alloy oxides from the final DeepPot Cu-Ni-O potential with ground-truth DFT values

mance of the DeepPot force field, with RMSE $<$ 2 eV. A small systematic error for alloy surfaces without oxygen is noticeable: this is because the per-atom energy for Ni is manually set to -5.13 eV for the purpose of formation energy calculations instead of the output from the DeepPot model itself. Because Ni structures were not used in the training, this reference energy is calculated incorrectly by the model. Using this reference energy instead of an internally calculated Ni bulk formation energy drives a systematic displacement from the DFT parity line for metallic structures, particularly those including many Ni atoms. Additionally, the per-atom reference energy for oxygen–equal to half of the formation energy of diatomic oxygen–is also manually set to -2.55 eV. Because diatomic oxygen samples were used to train the model, there is a smaller difference between the reference energy from the model (-2 eV) and that selected for benchmarking (-2.55 eV).

Despite usage of reference energies from outside the model, systematic deviations from parity are a degree of magnitude smaller than the random errors of the ReaxFF model for

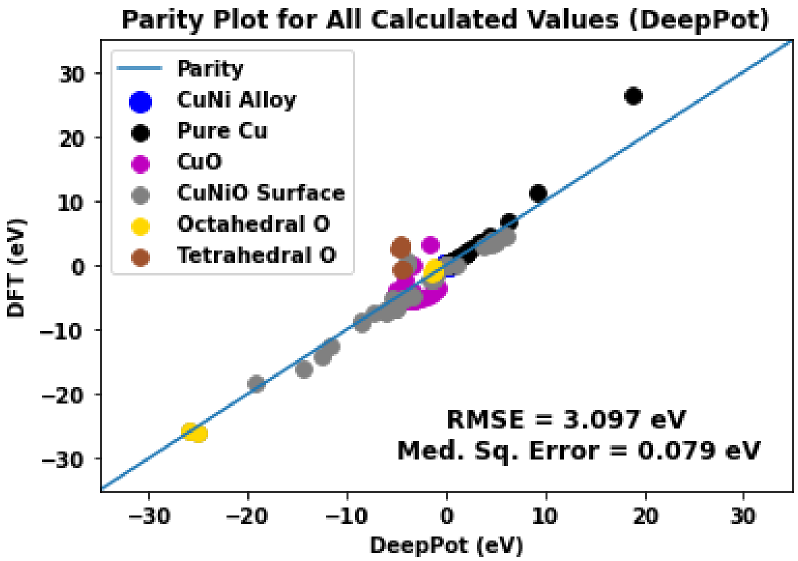

Figure 26: Parity plot comparing surface, bulk formation, and binding energies of Cu, CuO, CuNi, and surface alloy oxides from the final DeepPot Cu-Ni-O potential with ground-truth DFT values

the same system.

The performance of the DeepPot force field for roughened, reconstructed surfaces also closely matches that expected from DFT, with RMSE < 2 eV as well. Fortunately, there are no systematic errors in this subset of the data. Full binding energy curves with comparisons to the first-principles dataset are provided in the Appendix for FCC and HCP Cu (A.8.1) and Ni (A.8.3) as well as FCC CuO A.8.2. Performance on bulk FCC NiO is poor since those structures were not included in the training. This binding curve has been omitted from the presented results for lack of relevance to the CuNi surface oxide system. However, the use of reference energies external to the model explains the systematic error for pure Ni as well as NiO. In the future, further training with pure Ni and NiO bulk structures will be necessary to avoid reliance on exogenous reference energies from the literature. Ideally, the model will replicate these references through learning on those systems.

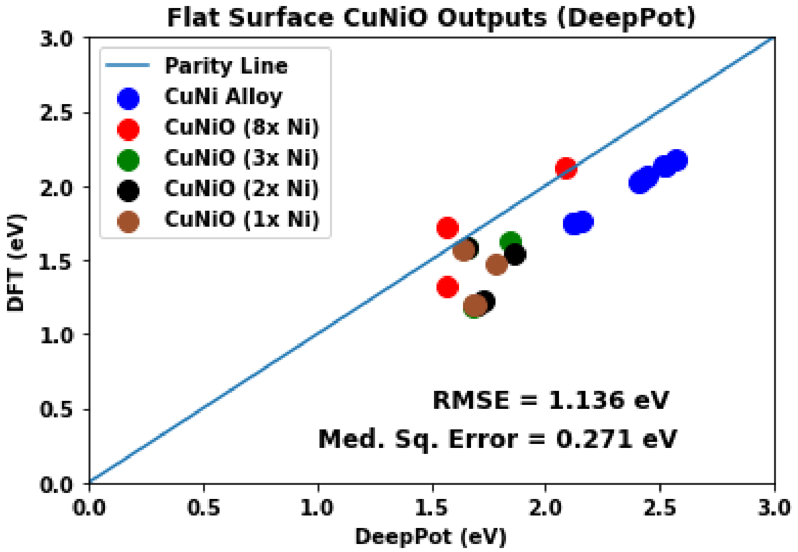

Figure 27: Parity plot comparing surface energies of pristine surface alloy oxides from the final DeepPot Cu-Ni-O potential with ground-truth DFT values

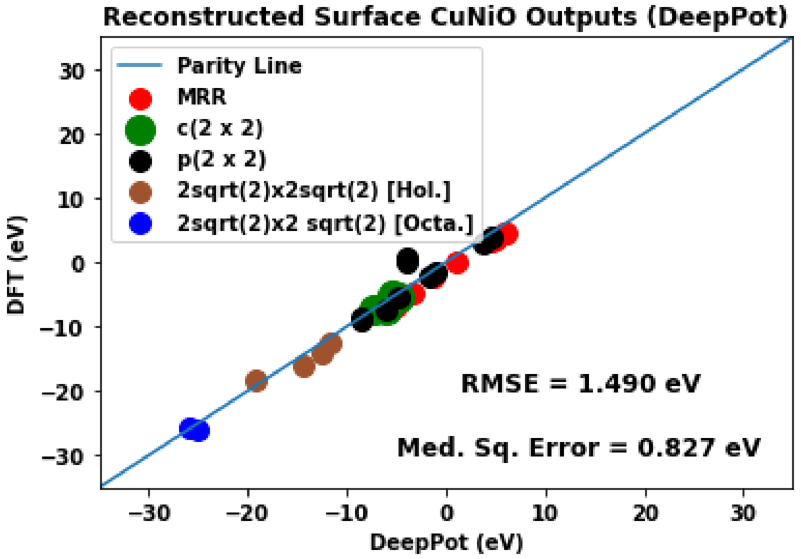

Figure 28: Parity plot comparing surface energies of pristine surface alloy oxides from the final DeepPot Cu-Ni-O potential with ground-truth DFT values

5.0 Conclusions

The work in this thesis describes multiple improvements to simulation of CuNi surface segregation and oxidation. Namely, the acceleration of the molecular dynamics of binary alloy segregation was achieved using a hierarchy of multiscale tools, including ParSplice and KMC-based methods. Novel trajectory analysis tools are presented in this work to effectively harness the data from these simulations. Additionally, two separate optimizations of Cu-Ni-O interatomic potentials using an evolutionary algorithm and a deep learning approach were carried out using the same dataset of structures relaxed with first-principles methods. This database provides a set of oxide formation energies that estimate the cutoff for surface oxygen fractional coverage before oxide nucleation begins.

The thermodynamic knowledge within this database is first described in chapter two, which focuses on the preference for Ni to segregate into the bulk of CuNi binary alloy during annealing. This chapter also introduced small timescale and equilibrium simulations of CuNi segregation using MD and MC to probe the initial and final stages of alloy segregation. To describe vacancy migration and its inherent relation to metallic segregation, a novel trajectory analysis was proposed, with code at `github.com/15garzab/trajectory-analysis-redux`. In this approach, the cross-correlation between particle coordinates from molecular dynamics is calculated via convolutions in time with a range of lag times, determining not only lead-lag dynamics between two particles, but also spatiotemporally localizing critical events responsible for metallic phase separation on the atomic and nanoscale.

In the third chapter, accelerated dynamics methods revealed the rate of segregation in CuNi alloy from nanosecond to second timescales, reaching 2 seconds of simulation time and the equilibrium composition with KMC, the most approximate of the methods. The resultant composition profile shows no Ni on the top surface monolayer, with less than 15at% Ni in the 2nd layer compared to 22at% Ni in the bulk on a per layer basis, in agreement with MC predictions. Though most of our accelerated methods were used to simulate up to the µs timescale, only modified KMC dynamics could reach the equilibrium profile obtained from MC and previous experimental observations. Our model estimates that the timescale for segregation in the top layer to reach equilibrium is on the order of 0.1 ms, while equilibrium segregation does not penetrate to the 3$^{\text{rd}}$ layer until timescales on the order of 100 ms. The equilibrium timescales for surface segregation of any FCC bimetal can be determined with a combination of AKMC and KMC. However, KMC-based methods require assumptions regarding transition state theory, and they do not resolve fast atomic exchange processes as well as ParSplice and MD. Our study shows that a model for the relationship between solvent distribution, activation energy, and large-scale phenomena like segregation may be developed from further simulations of bimetallics on experimental timescales. Our methodology is general, and can be applied in the future using other interatomic potentials, including those derived from machine learning[117, 7]. Further, the trajectory analysis method of cross-correlation heatmapping allowed for unique mechanisms to be identified and differentiated based upon the local vacancy concentration in the presence of segregating alloy components.

In the fourth chapter, we presented multiple novel interatomic potentials for the simulation of CuNi surface oxidation from first adsorption to oxide nucleation. The first-principles data used in this optimization contain thermodynamic insights meriting their own discussion: the oxygen surface coverage θ_O which inverts the expected surface segregation trend ($\theta_O > 0.125$) also depends on the density of surface defects after reconstruction. Calculations of formation energies for surface oxides identified the onset of oxide nucleation as a function of oxygen coverage.

The first force field presented in Chapter 4 was a reactive forcefield (ReaxFF) based on bond-order and VSEPR theories, resulting in an accurate description of alloyed surface oxides for a variety of oxygen coverages and surface reconstructions. Further, the pure metals and their oxides are also well-described by this potential, which was created by combining two previous potentials for CuO and NiO, then refining with a particle swarm optimization algorithm (PSO). The developed potentials replicate a variety of DFT calculations for both static oxidized structures and dynamic oxidation processes. Our new reactive force field exhibits improved performance for bulk and surface NiO structures compared to previous Ni-O interaction parameters. The ReaxFF parameters for the Cu-Ni-O system also exhibit good fit with ab initio formation energies for all metals and oxides occurring in the bulk and on the surface of the alloy, except those resulting from insertion of oxygen at interstitial positions, an excited state not expected to occur in the real system. The code I wrote for this ReaxFF development is available at `github.com/15garzab/pso_rff`.

The database of DFT-relaxed structures I created was used by my advisor (Saidi) to train a second Cu-Ni-O interaction model with thousands of parameters and greater accuracy for surface alloy oxides and Cu-rich metal oxide systems, a deep learned, neural network model (DeepMD). Though he omitted pure Ni and NiO structures from the training, there is excellent performance on the Cu, Cu-O, and Cu-Ni-O training data including alloyed and oxidized structures in the bulk and on both pristine and defective (100) surfaces.

This thesis has established multiple new tools which can be used in concert to advance the study of nanoscale surface science beyond what is currently possible in environmental microscopy. Before this work, metal oxide formation could only be partially resolved with state-of-the-art electron microscopy on much longer timescales than are covered by accelerated dynamics (Chapter 3).

In future, canonical and grand canonical dynamics from these potentials will be carried out to reveal the nature of transient, competitive surface oxidation on cupronickel using MD acceleration. Progression from diatomic adsorption and disassociation of oxygen to surface reconstruction can be followed all the way through oxide initiation and growth using accelerated techniques. The order and timing of duplex oxide formation under various temperatures and oxygen pressures can be tested using accelerated dynamics in combination with the developed interatomic potentials from this work. These timescales are expected to be an order of magnitude greater (minutes) than those for vacuum segregation (seconds). To deduce various mechanisms taking place during reconstruction and oxide nucleation, cross-correlation trajectory analysis can be applied to output data from these simulations (Chapter 2 and Chapter 3). Cross-correlation analysis could be adapted for application to TEM images as well, since the appearance/disappearance of atomic columns in space constitutes a time series evolving as oxidation proceeds. Application of this method to TEM imagery will be complicated by the difficulty in tracking individual point defects using TEM alone, though their positions may be inferred by the rate of disappearance or lightening of atomic columns. Any new interatomic potentials needed for other alloy systems can be quickly trained using the particle swarm method described in Chapter 4. MD acceleration, force field optimization, and trajectory analysis together comprise a complete toolbox to boost the efficiency and scientific impact of molecular simulation at the atomic and nanoscales.

Appendix

A.1 Density Functional Theory (DFT)

The largest assumption underlying ab initio approaches lies in the Born-Oppenheimer approximation, which presumes that electronic equilibration occurs much faster than nuclear equilibration. Essentially, the nuclear coordinates $\mathbf{R}$ can be held constant while the electronic positions $\mathbf{r}$ are first optimized in phase space, since the nuclei are much more massive than the electrons. The many-body problem of electron repulsion remains unsolved in the original Schrödinger representation but is addressed by Hartree-Fock (HF) and Kohn-Sham (KS) theories, the latter of which is termed density functional theory (DFT). Forces on atoms will depend on the electron density field (bonding and coordination environment), coulombic internuclear repulsion/attraction, van der Waals forces, and some amount of shielding. During structural relaxation, the electronic component is optimized before nuclear positions can be iterated using the force:

$$\mathbf{F} = -\nabla E(\mathbf{R}) \tag{A.1}$$

Electronic relaxation steps (fixed-point calculations) must be taken between ionic relaxations. To solve the many-body problem for electrons, one can consider the adjacent problem of finding the electron density: the electron positions are reduced to a scalar density which depends on 3 position variables instead of 3N position variables for N particles in the original problem. We seek the density functional $\rho(\mathbf{r})$, that is, the relationship between system energy and the position-dependent electron density can be expressed as a variational upper bound to the energetic eigenvalues of the electronic Schrödinger equation:

$$E_{DFT}\left[\rho(\mathbf{r})\right] \geq E_{actual} \tag{A.2}$$

In order to accomplish this, for each state in phase space, there must be a unique 1:1 relationship between a single spatial function of electron density $\rho(r)$ and a set of energies E. Fortunately, the Hohenberg-Kohn theorem [9, 46, 51] provides the necessary proof of this fact for the ground-state, and extensions by subsequent theorists proved the same for excited states.

Statistical ensemble effects must be taken into account as well, since electrons are indistinguishable and can be exchanged to yield the same energy. The so-called exchange-correlation energy is a quantum mechanical effect that results in the Pauli exclusion principle, the filling of orbitals with paired electrons of opposite spin. Hartree-Fock theory provides analytical forms for the exchange integral yet only approximates the many-body problem with a system of one-electron wavefunctions interacting with an approximate electron cloud. Unfortunately, the approach fails to account for correlation in the electron ensemble.

The density functional can be used instead to approximates both exchange and correlation, since it provides a description of the electron gas as a function of only 3 coordinates. Re-contextualizing the problem in terms of a single density for all the electrons eliminates the summations over all coulombic attractions and repulsions from the second and third terms. DFT does not yield results for the kinetic energy (first term) or the exchange-correlation energy E_{XC} directly in terms of $\rho(\mathbf{r})$: the former is obtained using a pseudo-velocity based on Kohn-Sham (KS) wavefunctions which do not represent physical electrons. Briefly, the KS equations can be written as:

$$\left[-\frac{1}{2}\nabla^2 + V_Z(\mathbf{r}) + V_H[\rho](\mathbf{r}) + V_{XC}[\rho](\mathbf{r})\right]\psi_i = \epsilon_i\psi_i \tag{A.3}$$

where the first two terms represent kinetic energies of the electrons and their coulomb interactions with the fixed ionic potential V_Z. The potential V_H is for the Hartree energy resulting from the electrostatic potential formed by the electron density, and V_{XC} is the exchange-correlation energy depending only on the density functional. The wavefunctions of KS theory are unphysical, merely interacting with the ions and approximated electron gas to yield an expectation value for kinetic energy which is not tied to a true particle velocity. Although it is not the focus of further discussion in this text, there are many resources available which discuss the details of Kohn-Sham theory[11, 1, 24].

The exchange energy can be obtained directly from Hartree-Fock (HF) theory or through a variety of approximation and tabulation methods. The coupling of exchange and correlation is more difficult to account for, but the simplest way is to vary this energy directly with the local density approximation (LDA) for a homogeneous electron gas [23, 82]:

$$E_{XC}^{LDA}[\rho] = \int \rho \epsilon_{XC}^{unif}(\rho_\uparrow, \rho_\downarrow) = C \int \rho^{4/3}(\mathbf{r}) d\mathbf{r} \tag{A.4}$$

which obeys detailed balance for the spin density ($\rho = \rho_\uparrow + \rho_\downarrow$). Many methods have been developed to account for exchange and correlation including using the gradient of the electron density (e.g. GGA methods); these various approximations constitute the namesake functionals of density functional theory. Hybrid functionals are constructed with a weighted sum of the exact HF exchange energy and the approximate LDA/GGA result in addition to some derived or empirical contribution. In the present work, the hybrid functional PBE0[2]–derived from the original PBE functional of Perdew, Burke, and Enzerhof [82]–is used, where exchange contributions are denoted with the subscript 'X' and correlation terms with 'C':

$$E_{XC}^{PBE0} = \frac{1}{4} E_X^{HF} + \frac{3}{4} E_X^{PBE0} + E_C^{PBE} \tag{A.5}$$

The periodicity of the simulation cell created in 2.1 must be taken into account, therefore all basis functions within Kohn-Sham DFT should be periodic as well. The non-physical wavefunction must now exhibit translational invariance over the box length:

$$\begin{aligned} \psi_{n\mathbf{k}}(\mathbf{r} + \mathbf{R}) &= \psi_{n\mathbf{k}}(\mathbf{r}) e^{i\mathbf{k}\mathbf{R}} \\ \psi_{n\mathbf{k}}(\mathbf{r}) &= u_{n\mathbf{k}}(\mathbf{r}) e^{i\mathbf{k}\mathbf{r}} \\ u_{n\mathbf{k}}(\mathbf{r} + \mathbf{R}) &= u_{n\mathbf{k}}(\mathbf{r}) \end{aligned} \tag{A.6}$$

where $\mathbf{k}$ is the Bloch vector and n is the band index. The Bloch vector $\mathbf{k} = [k_x, k_y, k_z]$ is constrained to the first Brillouin zone $k_i \in [0, \frac{\pi}{a}]$ where a is the primitive cell length for a cubic system. This zone represents a constant energy surface for electron kinetic energies in reciprocal space, or k-space. The form of each component in $\mathbf{k}$ differs for other Bravais lattices.

The cell-periodic wavefunctions have a set of basis functions to allow for a large expansion to be made and truncated at a desired cutoff for the kinetic energies: $\frac{1}{2}|\mathbf{G} + \mathbf{k}|^2 < E_{\text{cutoff}}$ where a large cutoff is chosen to model the more tightly held and energetic core electrons.

$$\psi_{n\mathbf{k}}(\mathbf{r}) = \frac{1}{\Omega^{\frac{1}{2}}} \sum_{\mathbf{G}} C_{\mathbf{G}n\mathbf{k}} e^{i(\mathbf{G}+\mathbf{k})\mathbf{r}} \tag{A.7}$$

A plane wave basis set composed of $C_{\mathbf{G}n\mathbf{k}}$ band occupancies yields the orbital occupancies $C_{\mathbf{r}n\mathbf{k}}$ with straightforward Fast Fourier transform. The volume of the primitive cell depends on its lattice parameters i.e. $\Omega = \mathbf{a}_1 \cdot \mathbf{a}_2 \times \mathbf{a}_3$.

In summary, the KS wavefunctions are optimized along a mesh of k-points distributed in reciprocal space, then FFT is used to recover the real-space representation. The Brillouin zones of k-space are analogous to Wigner-Seitz cells, which represent the primitive cell in direct space and a unique Bravais lattice. The concept of Wigner-Seitz cells formed from Voronoi tesselation in real space is important for the detection of vacancies in the FCC CuNi alloy, since cells with zero atomic occupancy must have a local defect in the lattice.

The Wigner-Seitz analysis available through OVITO is used in this work to detect point defects and their dynamics, forming pseudo-particle trajectories evolving in time alongside the real Cu and Ni atoms[94]. The absence of mass in the lattice breaks local coordination shells and provides a low energy pathway for migration through the defect site such that vacancies become the primary predictor of both segregation mechanism and timescale.

A.2 Velocity-Verlet Algorithm

A Taylor series can be used to approximate the N x 3 matrix of particle positions at the next timestep $\mathbf{r}(t + \Delta t)$ from the current positions $\mathbf{r}$ given knowledge of its derivatives with respect to time. The original Verlet algorithm [101] utilizes the central difference approximation for the first derivative of position, equivalent to finding the velocity:

$$\begin{aligned} \mathbf{r}_i(t + \Delta t) &= \mathbf{r}_i(t) + \frac{d\mathbf{r}_i}{dt}\Delta t + \frac{1}{2}\frac{d^2\mathbf{r}_i}{dt^2}\Delta t^2 + ... \\ &= \mathbf{r}_i(t) + \mathbf{v}_i(t)\Delta(t) + \frac{1}{2}\frac{\mathbf{f}_i(t)}{m}\Delta t^2 \end{aligned} \tag{A.8}$$

As shown, Newton's 2$^{\text{nd}}$ Law can be inserted in this equation with f(t) as a per-atom force. A similar expression can be made for $\mathbf{r}(t - \Delta t)$, then added to (A.8) to solve for the velocity. Truncating at second order results in the central difference approximation to the velocity:

$$\mathbf{v}_i(t) = \frac{\mathbf{r}_i(t + \Delta t) - \mathbf{r}_i(t - \Delta t)}{2\Delta t} \tag{A.9}$$

A more efficient version of the algorithm, the velocity-Verlet algorithm[96], instead acquires the next timestep's velocities using $\mathbf{r}(t+\Delta t)$ already known from (A.8). Because the force depends only on the position in the potential field, the value of $\mathbf{f}(t+\Delta t)$ is also known and can be used to directly compute the next set of velocities:

$$\mathbf{v}(t+\Delta t) = \mathbf{v}(t) + \frac{f(t) + f(t+\Delta t)}{2}\frac{\Delta t^2}{m} \tag{A.10}$$

This implementation is most common in modern simulation software like LAMMPS since it is faster and involves fewer computations as well as less memory overhead. Per-atom forces $f(t+\Delta t)$ are convenient to compute and store as they will be used for propagation in the next timestep too.

Non-equilibrium dynamics should have a varying total energy with fluctuating kinetic energy around a constant, target value tied to a certain temperature. Thus, many rescaling schemes have been developed for the velocities, keeping the system at equilibrium with a thermal bath to achieve the canonical NVT ensemble. For example, the Nosé-Hoover (NH) thermostat uses a momentum rescaling procedure to impart "friction" to the system, biasing velocities towards that of a desired temperature[29]. This fictitious friction force ζ is added to the force balance from Newton's 2^{nd} Law to make new equations of motion.

Stochastic dynamics within a surrounding solvent–or, on a longer timescale, an alloy with de-localized electrons–were not accounted for by the earlier Brownian dynamics, although the properties of its underlying random walk are still desirable to describe mass diffusion[18]. The Langevin equations for molecular dynamics are similar to those for NH dynamics, but the friction force is sampled from a probability distribution to resemble random thermal noise. The Gaussian width for this friction force sampling is chosen to satisfy the fluctuation-dissipation theorem for the non-equilibrium Langevin process held in thermal equilibrium with an external bath[89, 18].

A.3 Composition Profile Estimation from MC Data

Each step of the simulated annealing to equilibrium is dependent on the previous configuration (serial correlation), so the observed samples for calculating the estimated mean composition have a biased standard error that is overestimated by a naïve error calculation. To correct this, autocorrelation of subsequent frames in the MC process was estimated by assuming samples are generated by a first order autoregressive process (AR(1)):

$$X_t = c + \rho X_{t-1} + \epsilon_{unbiased} \tag{A.11}$$

where X_t is the estimated value at time t by the AR(1) model, c is an optional shifting constant (typically zero), and ϵ the corrected error we wish to estimate. The process has an analytically known correction to find the unbiased, standard error of the estimated mean from n measurements and depends on ρ to calculate the measurement error for each layer[92].

$$\sigma_{unbiased} = \sigma_{biased} \sqrt{\frac{1 + \frac{2\delta}{n}}{1 - \frac{2\delta}{n(n-1)}}} \tag{A.12}$$

A custom Perl script was used to analyze the output data from MC, finding the composition in each layer and tracking it over all the annealed samples. These measurements were exported to a Python script which estimated values of ρ for the data using the 'statsmodels' module, and the above equations estimated accurate errors for plots of the equilibrium composition profiles.

A.4 Vacancy and Divacancy Formation Energies

The formation energy is similar to the expression used in 2.4 for surface energy without any areal normalization. A factor of $N - 1$ must be included to account for the removed atom from a bulk reference structure:

$$E_{1vac}^{formation} = E_f^{defective} - \frac{N-1}{N} E_{Cu}^{bulk} \tag{A.13}$$

The divacancy formation energies are also critical for predicting the stability of monovacancy pairs discussed in section 3.2.3. The formation energy of divacancies in the bulk of Cu can be computed

$$E_{2vac}^{formation} = E_f^{defective} - \frac{N-2}{N} E_{Cu}^{bulk} \tag{A.14}$$

where the defective structure relaxed to find $E_f^{defective}$ was created at varying separation distances using manual particle deletion in *atomsk*[45]. The formation energies for the divacancy in bulk Cu are shown below in Figure 29.

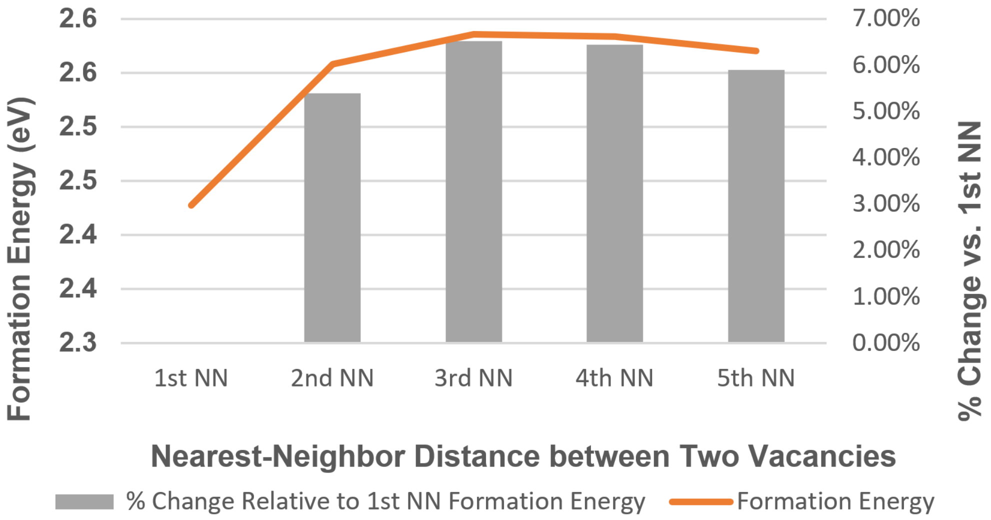

Figure 29: Divacancy formation energies and percent change in formation energy relative to that of the clustered divacancy at 1^{st} NN separation distance

A.5 Cluster Expansion Model for Kinetic Monte Carlo (KMC) Simulation

The reaction coordinate between two states is identified and analyzed using high-temperature sampling and climbing image nudged elastic band (CI-NEB) in AKMC. Contrastingly, our KMC model approximates these transition energies using an equation parametrized from

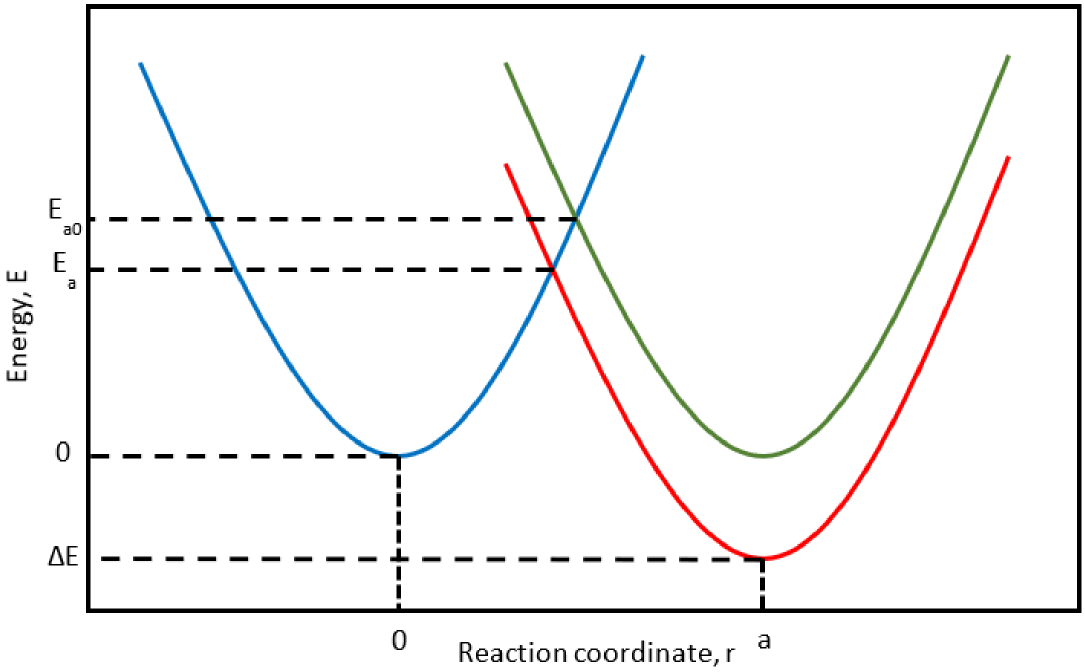

Figure 30: Parabolic construction showing energy diagram of a system. The blue curve is the initial state, the green curve is the final state with the same energy as the blue curve while the red curve is the final state with lower energy than the blue curve (Recreation)[111].

barriers already known from AKMC: in Figure 3-1, the energy of the red curve is lower than the green curve due to a change in local environment of the vacancy. As a result, the barrier is lower and the rate can be calculated analytically as[111]

$$\begin{gathered} E_a = \frac{(4E_{a0} + \Delta E)^2}{16E_{a0}} \\ \text{rate} = Ae^{\frac{-E_a}{kT}} \end{gathered} \tag{A.15}$$

where E_a is the barrier from one state to a lower-energy state (blue and red), E_{a0} is the barrier between two isoenergetic states (blue and green) also known as the intrinsic barrier, ΔE is the energy difference between the initial and the final state, A is the pre-factor in s^{-1}, k is the Boltzmann constant 8.617 eV*K^{-1}, and T is temperature in K. The intrinsic barrier E_{a0} obtained from AKMC data in 3.

Table 3: Intrinsic barrier of a vacancy migration event taken from AKMC data

Vacancy Location	**Surface**		**Subsurface**	
Moving atom	Cu	Ni	Cu	Ni
Intrinsic Barrier E_{a0} (eV)	0.453	0.487	0.635	0.681

To acquire ΔE, the energy of each state is needed for the equation

$$\Delta E = E_{v,i} - E_{v,j} \tag{A.16}$$

where $E_{v,i}$ is the total energy of the configuration with the vacancy at location i (final) and $E_{v,j}$ is the total energy of the configuration with the vcancy at location j (initial). Vacancy formation energy is calculated by

$$E_f = E_v - E_0 + \mu_a \tag{A.17}$$

where E_f is the vacancy formation energy, E_v is the total energy of the configuration with the vacancy, E_0 is the total energy of the configuration without the vacancy (initial configuration) and μ_a is the chemical potential of the atom removed from the initial configuration to make the vacancy.

The vacancy formation energy can then be used to determine ΔE:

$$\Delta E = (E_{f,i} + E_0 - \mu_a) - (E_{f,j} + E_0 - \mu_a) = E_{f,i} - Ef, j \tag{A.18}$$

Vacancy formation energy is predicted by the cluster expansion method, which samples multiple alloy structures uniformly at random vacancies with different local environments. The energies of these structures were calculated and used to parameterize the model shown in Figure 31.

While the cluster expansion model for KMC works for surface-surface and subsurface-subsurface diffusion, it fails to illustrate correct surface-subsurface migrations (Figure 31b)

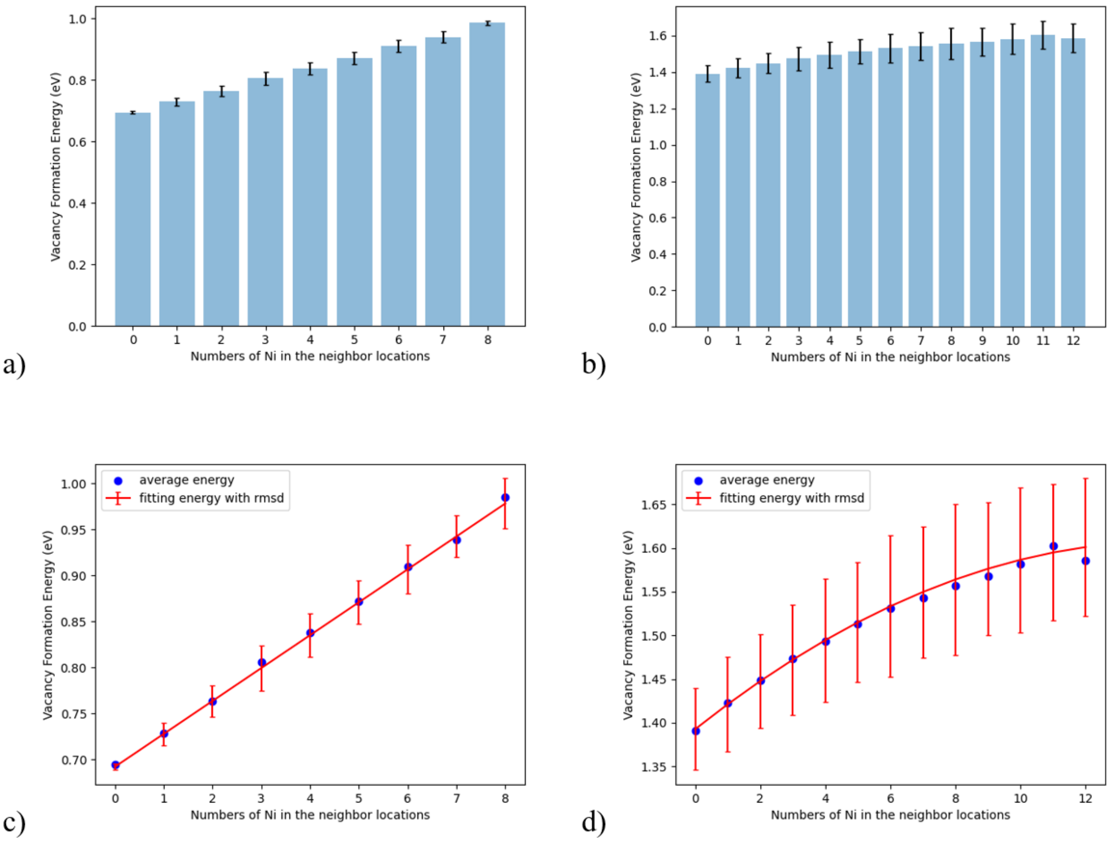

Figure 31: Average and standard deviation values of vacancy formation energy at (a) surface and (b) subsurface. Cluster expansion fitting model for the vacancy formation energy at (c) surface and (d) subsurface.

since the identity of the migrating atom (counter to the vacancy movement) is not included in this model: Ni requires higher barriers (∼0.95-1.0 eV) than Cu (∼0.8-0.9 eV) to move from surface to subsurface according to AKMC data. To fix this significant qualitative limitation of the cluster expansion model, a new definition for the barriers of a vacancy migration from surface to subsurface is proposed based on the AKMC data:

$$E_{a,surf\rightarrow sub} = \Delta E + E_{a,sub\rightarrow surf} \tag{A.19}$$

The AKMC data shows that the barriers of a vacancy migration from surface to subsurface are very similar to the energy difference of final and initial states (ΔE in the equation above), and values of , $E_{a,sub\rightarrow surf}$ are very small (0.049 eV for moving Cu atom and 0.067 eV for moving Ni atom) regardless of local environment. Figure 32 depicts an interpretation to calculate the barriers of a vacancy migration from surface to subsurface by adding the difference in energy, ΔE, between two states to $E_{a,sub\rightarrow surf}$.

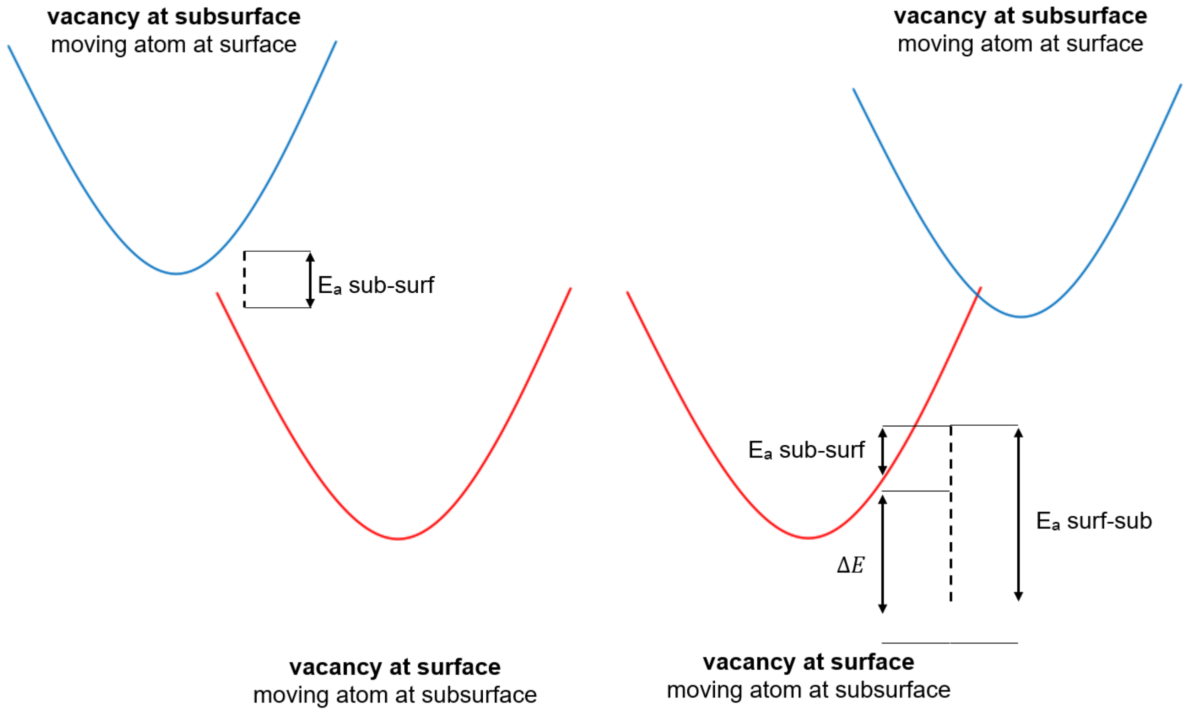

Figure 32: An illustration to determine the barrier of vacancy migration from surface to subsurface using the existed barrier of vacancy migration from subsurface to surface.

By the new definition, the barrier difference between Ni and Cu originates from the energy difference of two states ΔE, and its correction is significant to obtain correct dynamics. To include this information, ΔE was calculated from EON, where AKMC runs, then compared with the numerically calculated ΔE from cluster expansion. This discrepancy is illustrated in Figure 33: the errors are approximately 0.09 eV for Cu and 0.24 eV for Ni, so these correction values were chosen to improve the cluster expansion model.

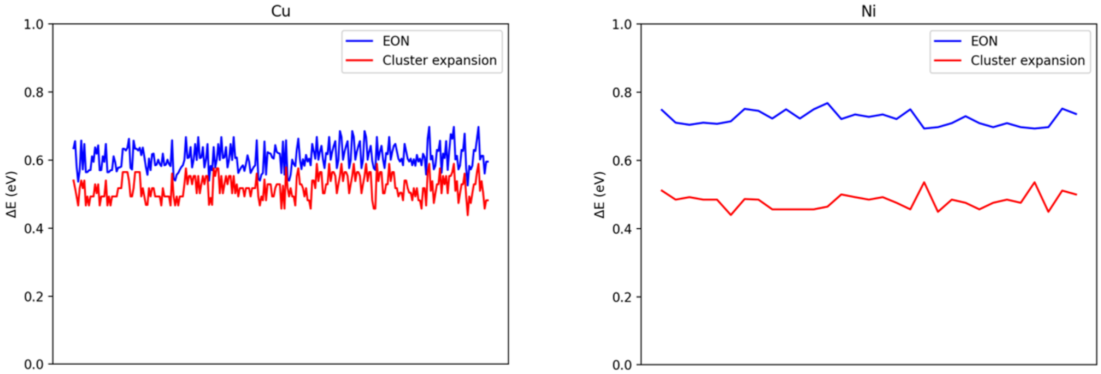

Figure 33: A plot showing the discrepancy between ΔE from EON and from cluster expansion.

A.6 Comparison of AKMC and KMC Results

Figure 34 presents the energy profiles obtained from AKMC and KMC simulations that reach a timescale of 300 μs, realizing 144,597 and 124,650 transition states respectively. Both methods show two Ni segregation events away from the surface at ∼100 - 125 μs and ∼170 - 200 μs, which correspond to the energy drops in Figure 34. This comparison supports that our KMC model can simulate the similar behaviors that were observed in AKMC.

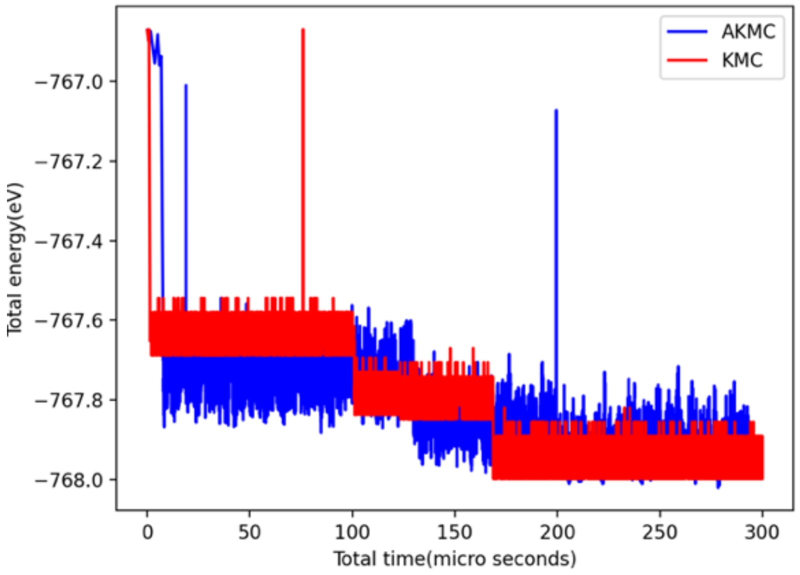

Figure 34: Energetic profiles of AKMC (blue) and KMC (red) simulations with respect to the total time of 300 μs.

A.7 ReaxFF Performance Benchmarks

A.7.1 Pure Ni: FCC and HCP Binding Energy Curves

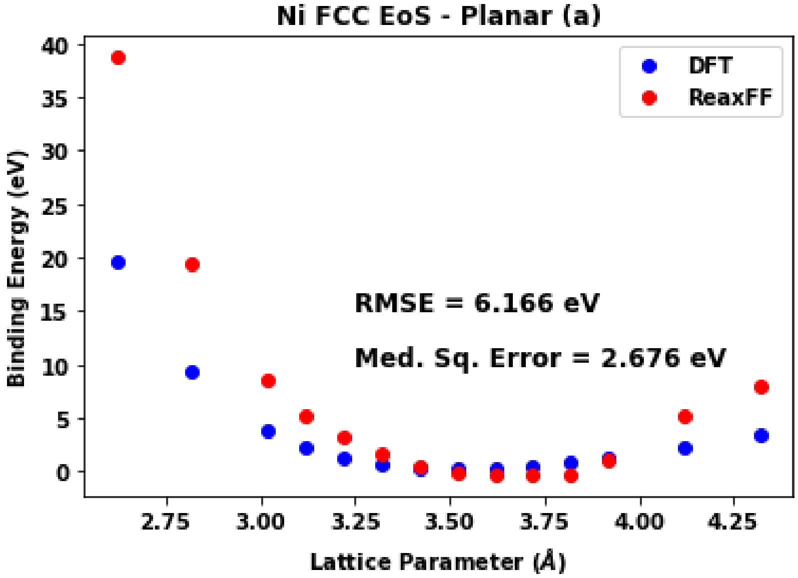

Figure 35: Binding energy as a function of planar lattice parameter (a) for FCC Ni calculated with outputs from the improved Ni-O RFF parameters

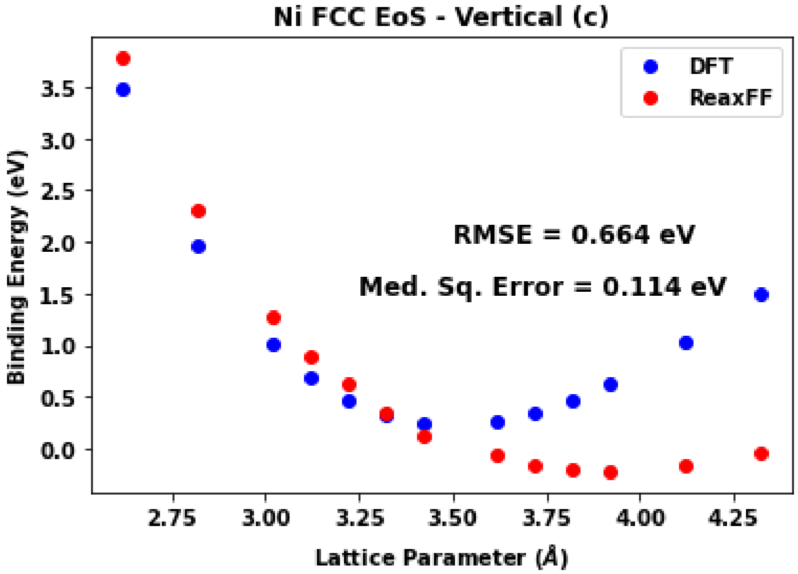

Figure 36: Binding energy as a function of vertical lattice parameter (c) for FCC Ni calculated with outputs from the improved Ni-O RFF parameters

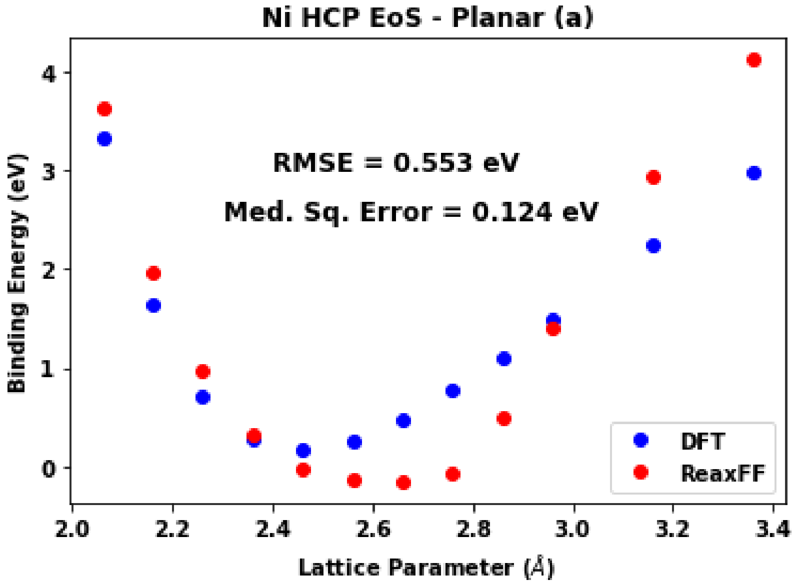

Figure 37: Binding energy as a function of planar lattice parameter (a) for HCP Ni calculated with outputs from the improved Ni-O RFF parameters

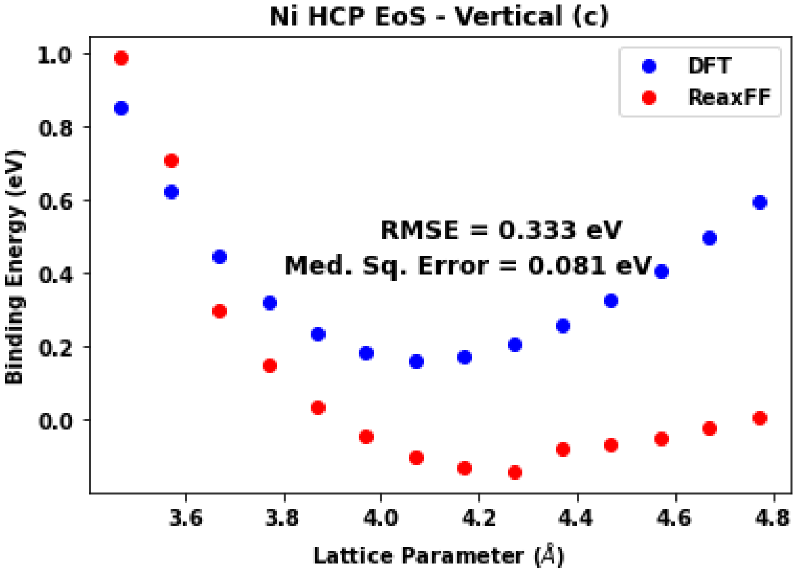

Figure 38: Binding energy as a function of vertical lattice parameter (c) for HCP Ni calculated with outputs from the improved Ni-O RFF parameters

A.7.2 Pure Cu: FCC and HCP Binding Energy Curves

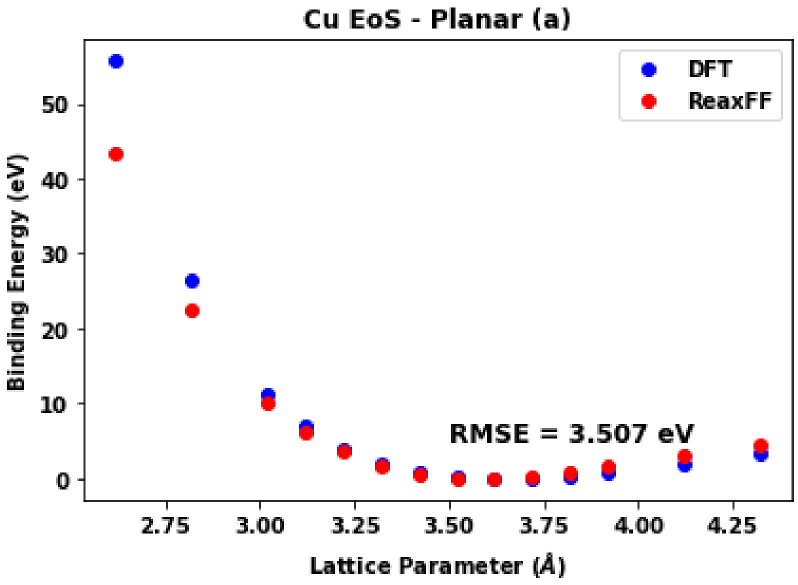

Figure 39: Binding energy as a function of planar lattice parameter (a) for FCC Cu calculated with outputs from the improved Cu-Ni-O RFF parameters

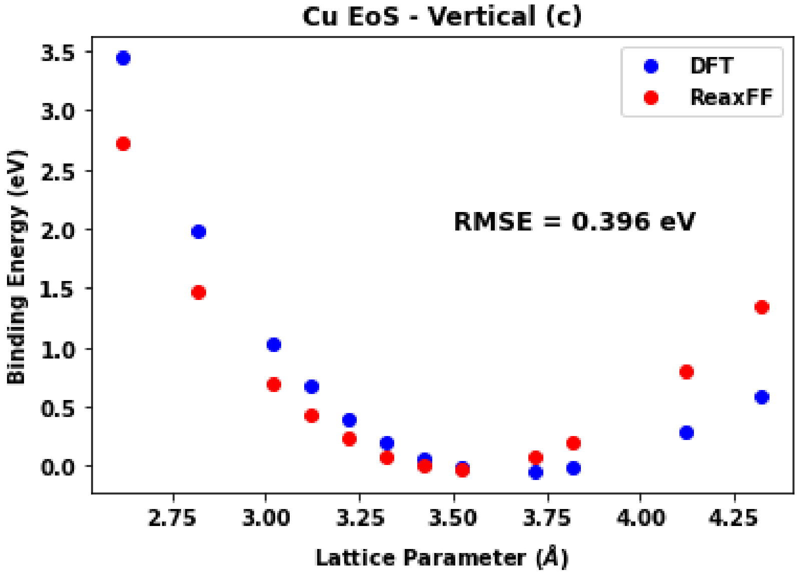

Figure 40: Binding energy as a function of vertical lattice parameter (c) for FCC Cu calculated with outputs from the improved Cu-Ni-O RFF parameters

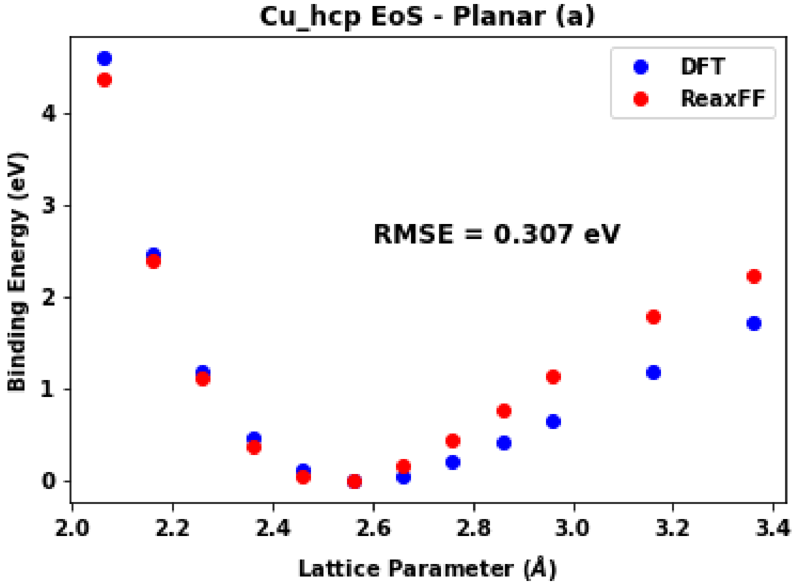

Figure 41: Binding energy as a function of planar lattice parameter (a) for HCP Cu calculated with outputs from the improved Cu-Ni-O RFF parameters

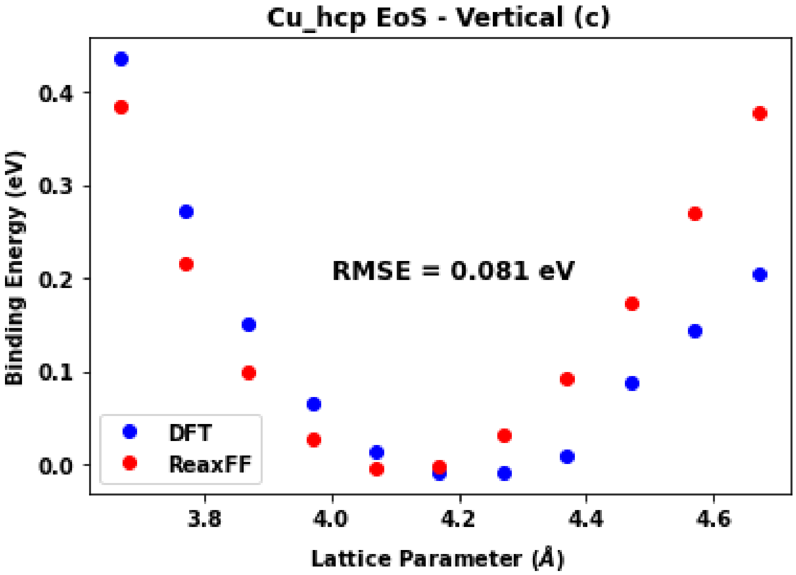

Figure 42: Binding energy as a function of vertical lattice parameter (c) for HCP Cu calculated with outputs from the improved Cu-Ni-O RFF parameters

A.7.3 CuO: FCC Binding Energy Curves

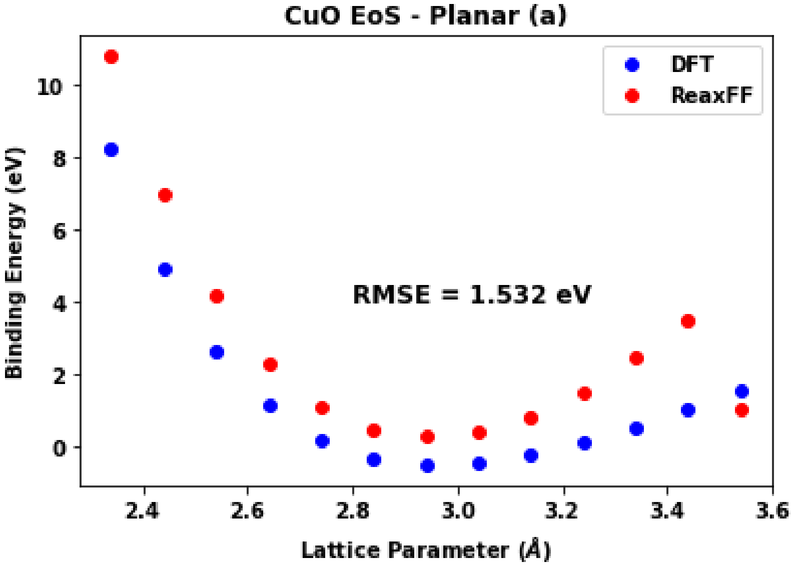

Figure 43: Binding energy as a function of planar lattice parameter (a) for FCC CuO calculated with outputs from the improved Cu-Ni-O RFF parameters

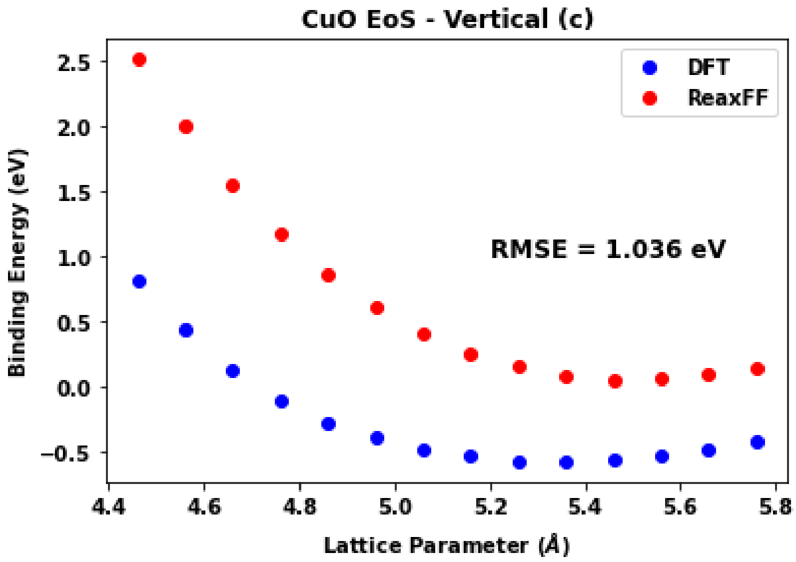

Figure 44: Binding energy as a function of vertical lattice parameter (c) for FCC CuO calculated with outputs from the improved Cu-Ni-O RFF parameters

A.7.4 Surface Energy Trends for Pure Cu, Pure Ni, and Ni-Doped Cu Surfaces

The surface energies from first-principles and ReaxFF are compared in the following figures for (100), (110), and (111) orientations. These slab models contain 90, 84, and 80 atoms, respectively. Figures 22 (pure Cu) and 46 (pure Ni) compare the calculated surface energies from ReaxFF and first-principles. Small variations in surface energy present when replacing a Cu atom in the pure slab with 1x Ni atom at varying depth. Energy differences between structures with Ni on the surface, subsurface (2^{nd}), and interior (3rd)in the surface were included in the training to account for surface segregation trends previously described in 2.

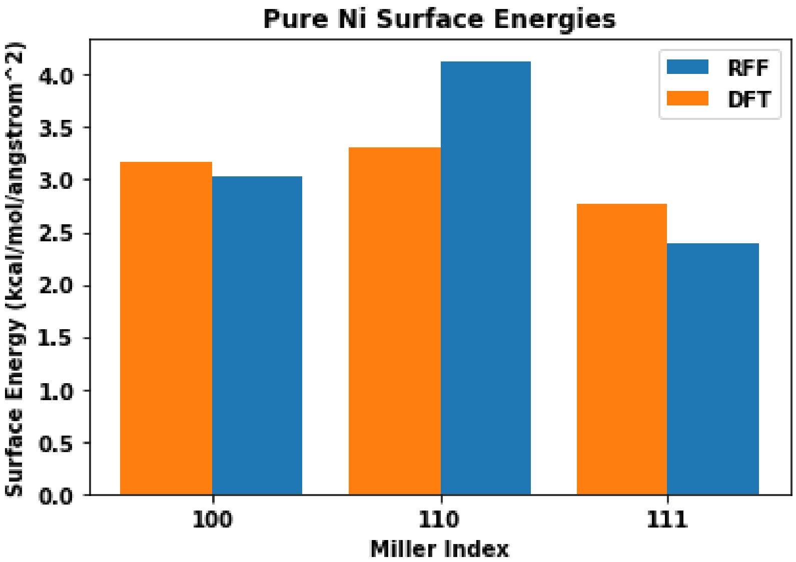

Figure 45: Surface energies from developed Cu-Ni-O ReaxFF potential and first-principles ground truth for pure Ni surfaces

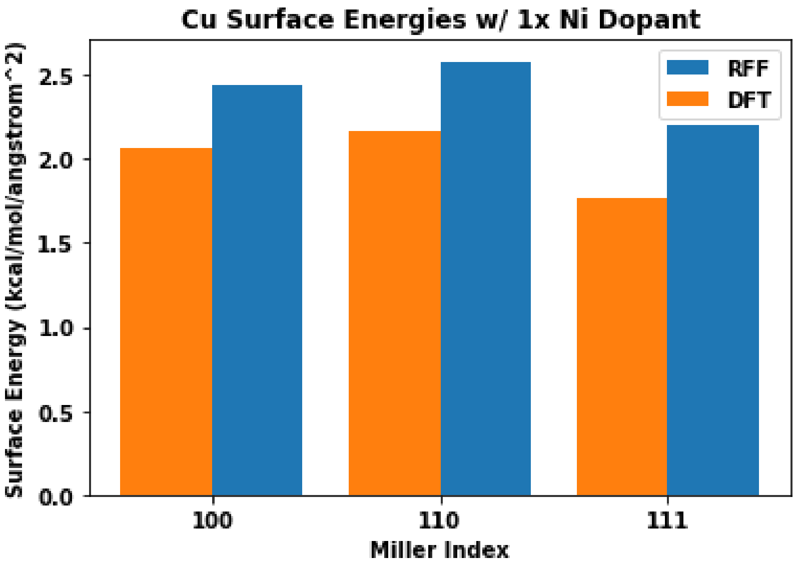

Figure 46: Surface energies from developed Cu-Ni-O ReaxFF potential and first-principles ground truth for Cu surfaces with 1x Ni atom on the surface

A.8 DeepPot Performance Benchmarks

A.8.1 Pure Cu: FCC and HCP Binding Energy Curves

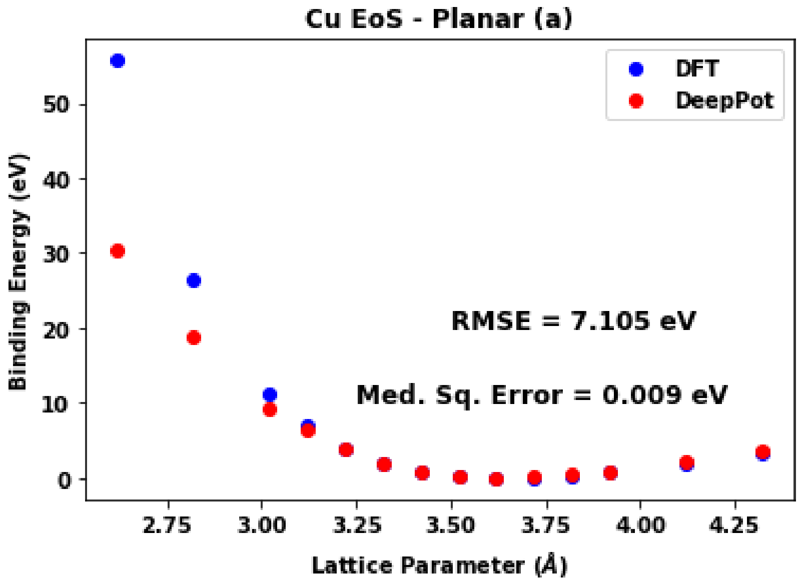

Figure 47: Binding energy as a function of planar lattice parameter (a) for FCC Cu calculated with outputs from the Cu-Ni-O DeepPot model

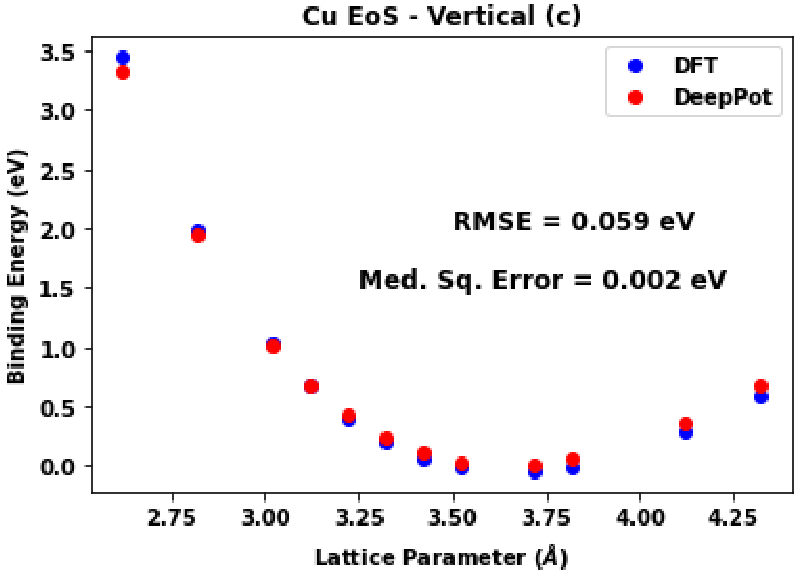

Figure 48: Binding energy as a function of vertical lattice parameter (c) for FCC Cu calculated with outputs from the Cu-Ni-O DeepPot model

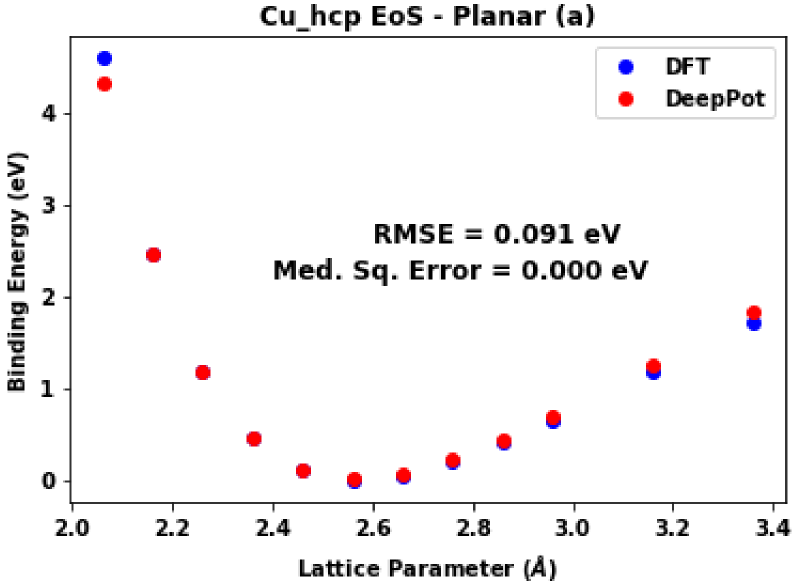

Figure 49: Binding energy as a function of planar lattice parameter (a) for HCP Cu calculated with outputs from the Cu-Ni-O DeepPot model

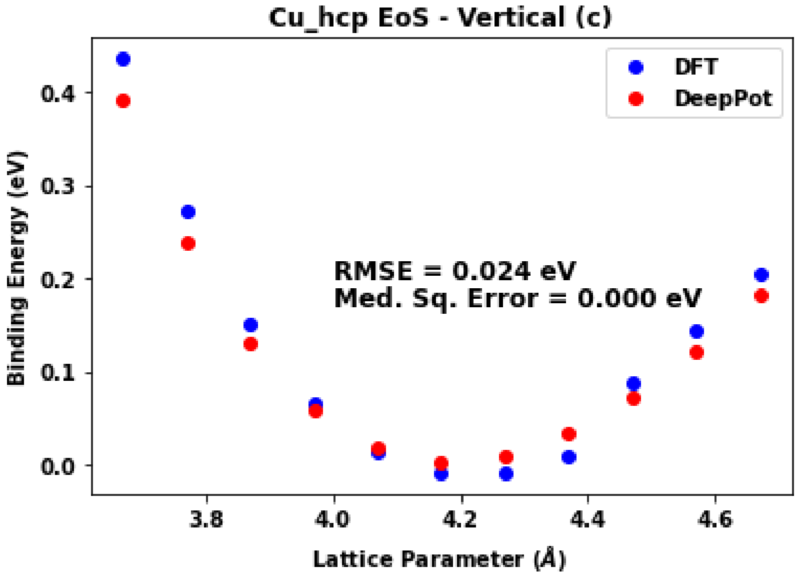

Figure 50: Binding energy as a function of vertical lattice parameter (c) for HCP Cu calculated with outputs from the Cu-Ni-O DeepPot model

A.8.2 CuO: Binding Energy Curves

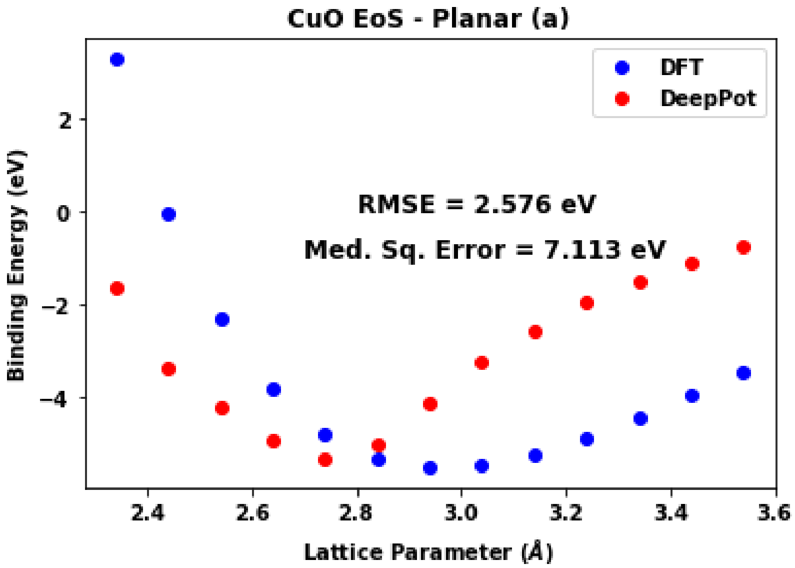

Figure 51: Binding energy as a function of planar lattice parameter (a) for FCC CuO calculated with outputs from the Cu-Ni-O DeepPot model

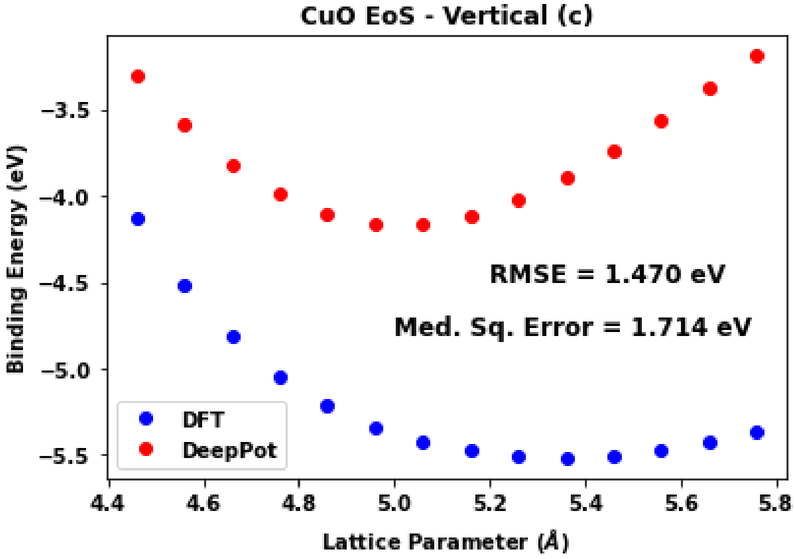

Figure 52: Binding energy as a function of vertical lattice parameter (c) for FCC CuO calculated with outputs from the Cu-Ni-O DeepPot model

A.8.3 Pure Ni: FCC and HCP Binding Energy Curves

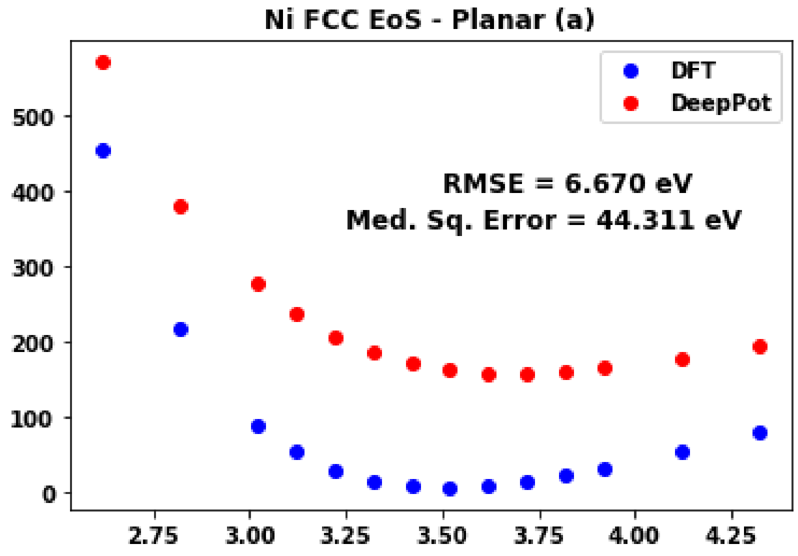

Figure 53: Binding energy as a function of planar lattice parameter (a) for FCC Ni calculated with outputs from the Cu-Ni-O DeepPot model

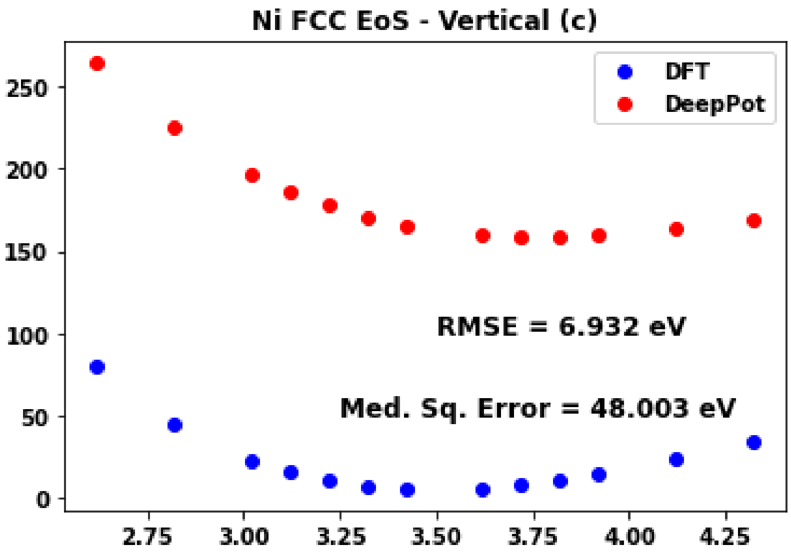

Figure 54: Binding energy as a function of vertical lattice parameter (c) for FCC Ni calculated with outputs from the Cu-Ni-O DeepPot model

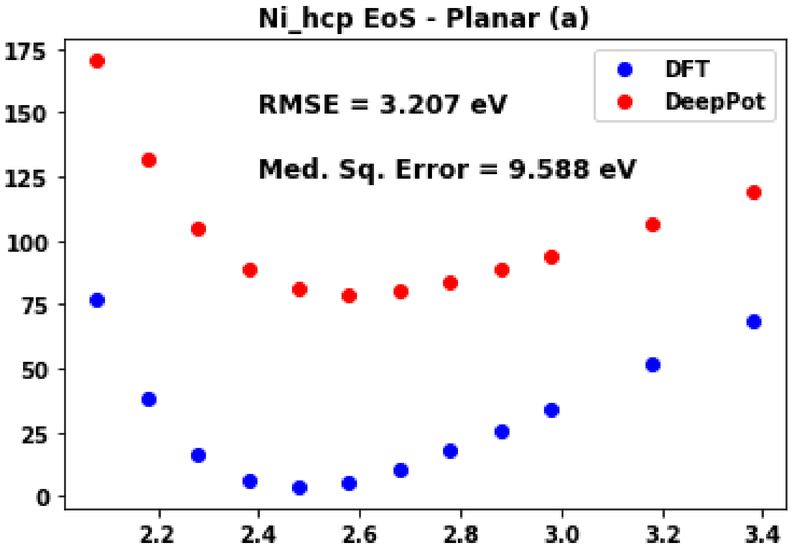

Figure 55: Binding energy as a function of planar lattice parameter (a) for HCP Ni calculated with outputs from the Cu-Ni-O DeepPot model

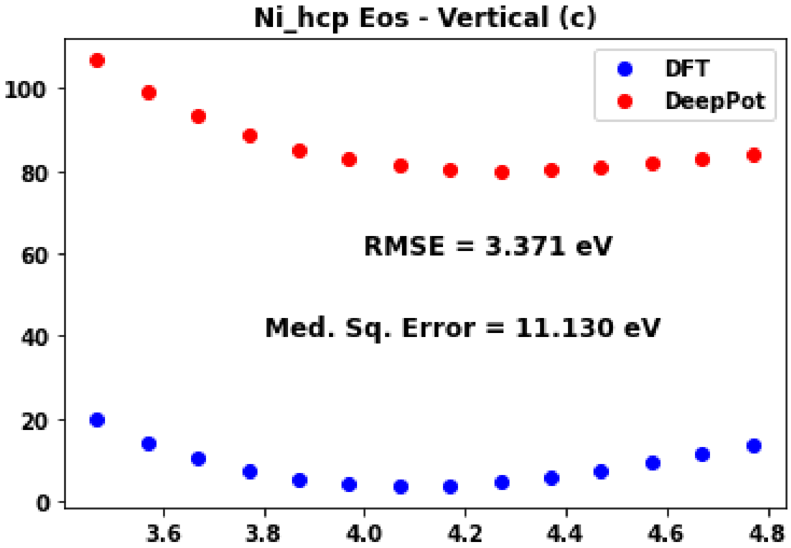

Figure 56: Binding energy as a function of vertical lattice parameter (c) for HCP Ni calculated with outputs from the Cu-Ni-O DeepPot model

Bibliography

[1] The Kohn-Sham Approach. In *A Chemist's Guide to Density Functional Theory*, chapter 5, pages 41–64. John Wiley & Sons, Ltd, 2001.

[2] Carlo Adamo and Vincenzo Barone. Toward reliable density functional methods without adjustable parameters: The PBE0 model. *The Journal of Chemical Physics*, 110(13):6158–6170, April 1999.

[3] John E. Adams and Jimmie D. Doll. Dynamical aspects of precursor state kinetics. *Surface Science*, 111(3):492–502, November 1981.

[4] Michael P. Allen and Dominic J. Tildesley. *Computer Simulation of Liquids: Second Edition*. Oxford University Press, Oxford, second edition, 2017.

[5] Mie Andersen, Chiara Panosetti, and Karsten Reuter. A Practical Guide to Surface Kinetic Monte Carlo Simulations. *Frontiers in Chemistry*, 7, 2019.

[6] D. A. Andersson and S. I. Simak. Monovacancy and divacancy formation and migration in copper: A first-principles theory. *Physical Review B*, 70(11):115108, September 2004.

[7] Christopher M. Andolina, Philip Williamson, and Wissam A. Saidi. Optimization and validation of a deep learning CuZr atomistic potential: Robust applications for crystalline and amorphous phases with near-DFT accuracy. *The Journal of Chemical Physics*, 152(15):154701, April 2020.

[8] Natalie Austin, Brandon Butina, and Giannis Mpourmpakis. CO2 activation on bimetallic CuNi nanoparticles. *Progress in Natural Science: Materials International*, 26(5):487–492, October 2016.

[9] Paul W. Ayers, Sidney Golden, and Mel Levy. Generalizations of the Hohenberg-Kohn theorem: I. Legendre Transform Constructions of Variational Principles for Density Matrices and Electron Distribution Functions. *The Journal of Chemical Physics*, 124(5):054101, February 2006.

[10] U. Bardi. The atomic structure of alloy surfaces and surface alloys. *Reports on Progress in Physics*, 57(10):939–987, October 1994.

[11] F. Matthias Bickelhaupt and Evert Jan Baerends. Kohn-Sham Density Functional Theory: Predicting and Understanding Chemistry. In *Reviews in Computational Chemistry*, pages 1–86. John Wiley & Sons, Ltd, 2000.

[12] P. E. Blöchl. Projector augmented-wave method. *Physical Review B*, 50(24):17953–17979, December 1994.

[13] Laure Bourgeois, Yong Zhang, Zezhong Zhang, Yiqiang Chen, and Nikhil V. Medhekar. Transforming solid-state precipitates via excess vacancies. *Nature Communications*, 11(1):1248, March 2020.

[14] H. H Brongersma, M. J Sparnaay, and T. M Buck. Surface segregation in Cu-Ni and Cu-Pt alloys; A comparison of low-energy ion-scattering results with theory. *Surface Science*, 71(3):657–678, February 1978.

[15] William D Callister and David G Rethwisch. *Materials Science and Engineering: An Introduction.* 2010.

[16] Fabrizio Carbone, Brett Barwick, Oh-Hoon Kwon, Hyun Soon Park, J. Spencer Baskin, and Ahmed H. Zewail. EELS femtosecond resolved in 4D ultrafast electron microscopy. *Chemical Physics Letters*, 468(4):107–111, January 2009.

[17] David Chandler. Statistical mechanics of isomerization dynamics in liquids and the transition state approximation. *The Journal of Chemical Physics*, 68(6):2959–2970, March 1978.

[18] C. E. Colosqui. Thermodynamics, Dynamics, and Kinetics at Liquid–Fluid and Fluid–Solid Interfaces. In Klaus Wandelt, editor, *Encyclopedia of Interfacial Chemistry*, pages 654–667. Elsevier, Oxford, January 2018.

[19] Matthew T. Curnan, Christopher M. Andolina, Meng Li, Qing Zhu, Hao Chi, Wissam A. Saidi, and Judith C. Yang. Connecting Oxide Nucleation and Growth to Oxygen Diffusion Energetics on Stepped Cu(011) Surfaces: An Experimental and Theoretical Study. *The Journal of Physical Chemistry C*, 123(1):452–463, January 2019.

[20] Nishith K. Das, Tetsuo Shoji, Takeharu Nishizumi, Taishi Fukuoka, Takeshi Sugawara, Ryouta Sasaki, Tadashi Tatsuki, Hideki Yuya, Keisuku Ito, Kimihisa Sakima, Kazuya Tsutsumi, Suguru Ooki, Yuichiro Sueishi, and Kiyoko Takeda. First-principles

calculations of hydrogen interactions with nickel containing a monovacancy and divacancies. *Materials Research Express*, 4(7):076505, July 2017.

[21] Murray S. Daw and M. I. Baskes. Embedded-atom method: Derivation and application to impurities, surfaces, and other defects in metals. *Physical Review B*, 29(12):6443–6453, June 1984.

[22] Murray S. Daw, Stephen M. Foiles, and Michael I. Baskes. The embedded-atom method: A review of theory and applications. *Materials Science Reports*, 9(7):251–310, March 1993.

[23] P. a. M. Dirac. Note on Exchange Phenomena in the Thomas Atom. *Mathematical Proceedings of the Cambridge Philosophical Society*, 26(3):376–385, July 1930.

[24] J. Dobson, G. Vignale, M. P. Das, and New Directions. Electronic density functional theory : Recent progress and new directions. *undefined*, 1998.

[25] R. G. Donnelly and T. S. King. Surface composition and surface cluster size distribution of Cu-Ni alloys via a monte carlo method. *Surface Science*, 74(1):89–108, May 1978.

[26] P. Ehrhart. Cu. In H. Ullmaier, editor, *Atomic Defects in Metals*, volume 25, pages 231–241. Springer-Verlag, Berlin/Heidelberg, 1991.

[27] P. Ehrhart. Ni. In H. Ullmaier, editor, *Atomic Defects in Metals*, volume 25, pages 242–250. Springer-Verlag, Berlin/Heidelberg, 1991.

[28] Z. Erdélyi, Ch. Girardeaux, Zs. Tôkei, D. L. Beke, Cs. Cserháti, and A. Rolland. Investigation of the interplay of nickel dissolution and copper segregation in Ni/Cu(111) system. *Surface Science*, 496(1):129–140, January 2002.

[29] D. J. Evans and B. L. Holian. The Nose–Hoover thermostat. *The Journal of Chemical Physics*, 83(8):4069–4074, October 1985.

[30] M. G. Evans and M. Polanyi. Some applications of the transition state method to the calculation of reaction velocities, especially in solution. *Transactions of the Faraday Society*, 31(0):875–894, January 1935.

[31] J Eymery and J. C Joud. Surface segregation in binary Cu-Ni and Pt-Ni alloys using Monte Carlo simulation. *Surface Science*, 231(3):419–426, May 1990.

[32] Keyvan Ferasat, Yuri N. Osetsky, Alexander V. Barashev, Yanwen Zhang, Zhongwen Yao, and Laurent Karim Béland. Accelerated kinetic Monte Carlo: A case study; vacancy and dumbbell interstitial diffusion traps in concentrated solid solution alloys. *The Journal of Chemical Physics*, 153(7):074109, August 2020.

[33] F. Fischer, G. Schmitz, and S. M. Eich. A systematic study of grain boundary segregation and grain boundary formation energy using a new copper–nickel embedded-atom potential. *Acta Materialia*, 176:220–231, September 2019.

[34] S. M. Foiles. Calculation of the surface segregation of Ni-Cu alloys with the use of the embedded-atom method. *Physical Review B*, 32(12):7685–7693, December 1985.

[35] Richard B. Garza, Jiyoung Lee, Mai H. Nguyen, Andrew Garmon, Danny Perez, Meng Li, Judith C. Yang, Graeme Henkelman, and Wissam A. Saidi. Atomistic mechanisms of binary alloy surface segregation from nanoseconds to seconds using accelerated dynamics. *Journal of Chemical Theory and Computation*, 18(7):4447–4455, 2022. PMID: 35671511.

[36] Helmut Gassner, Michael Probst, Albert Lauenstein, and Kersti Hermansson. Representation of Intermolecular Potential Functions by Neural Networks. *The Journal of Physical Chemistry A*, 102(24):4596–4605, June 1998.

[37] Brian Good, Guillermo Bozzolo, and John Ferrante. Surface segregation in Cu-Ni alloys. *Physical Review B*, 48(24):18284–18287, December 1993.

[38] Grégory Guisbiers, Subarna Khanal, Francisco Ruiz-Zepeda, Jorge Roque de la Puente, and Miguel José-Yacaman. Cu–Ni nano-alloy: Mixed, core–shell or Janus nano-particle? *Nanoscale*, 6(24):14630–14635, November 2014.

[39] T. Helander and J. Ågren. A phenomenological treatment of diffusion in Al–Fe and Al–Ni alloys having B2-b.c.c. ordered structure. *Acta Materialia*, 47(4):1141–1152, March 1999.

[40] Graeme Henkelman and Hannes Jónsson. A dimer method for finding saddle points on high dimensional potential surfaces using only first derivatives. *The Journal of Chemical Physics*, 111(15):7010–7022, October 1999.

[41] Graeme Henkelman and Hannes Jónsson. Long time scale kinetic Monte Carlo simulations without lattice approximation and predefined event table. *The Journal of Chemical Physics*, 115(21):9657–9666, November 2001.

[42] Graeme Henkelman, Blas P. Uberuaga, and Hannes Jónsson. A climbing image nudged elastic band method for finding saddle points and minimum energy paths. *The Journal of Chemical Physics*, 113(22):9901–9904, November 2000.

[43] M. Hennes, J. Buchwald, U. Ross, A. Lotnyk, and S. G. Mayr. Equilibrium segregation patterns and alloying in Cu/Ni nanoparticles: Experiments versus modeling. *Physical Review B*, 91(24):245401, June 2015.

[44] Andreas Heyden, Alexis T. Bell, and Frerich J. Keil. Efficient methods for finding transition states in chemical reactions: Comparison of improved dimer method and partitioned rational function optimization method. *The Journal of Chemical Physics*, 123(22):224101, December 2005.

[45] Pierre Hirel. Atomsk: A tool for manipulating and converting atomic data files. *Computer Physics Communications*, 197:212–219, December 2015.

[46] P. Hohenberg and W. Kohn. Inhomogeneous Electron Gas. *Physical Review*, 136(3B):B864–B871, November 1964.

[47] M. P. Ida and M. J. Miksis. The Dynamics of Thin Films I: General Theory. *SIAM Journal on Applied Mathematics*, 58(2):456–473, 1998.

[48] C. Jiang and B. Gleeson. Surface segregation of Pt in Γ'-Ni3Al: A first-principles study. *Acta Materialia*, 55(5):1641–1647, March 2007.

[49] Tingzhu Jin, Weifang Zhang, Ning Li, Xuerong Liu, Lu Han, and Wei Dai. Surface Characterization and Corrosion Behavior of 90/10 Copper-Nickel Alloy in Marine Environment. *Materials*, 12(11), June 2019.

[50] Johannes Kästner and Paul Sherwood. Superlinearly converging dimer method for transition state search. *The Journal of Chemical Physics*, 128(1):014106, January 2008.

[51] J. Katriel. An alternative interpretation of Theophilou's extension of the Hohenberg-Kohn theorem to excited states. *Journal of Physics C: Solid State Physics*, 13(15):L375–L376, May 1980.

[52] James Keck. Statistical investigation of dissociation cross-sections for diatoms. *Discussions of the Faraday Society*, 33(0):173–182, January 1962.

[53] G. Kresse and J. Furthmüller. Efficiency of ab-initio total energy calculations for metals and semiconductors using a plane-wave basis set. *Computational Materials Science*, 6(1):15–50, July 1996.

[54] G. Kresse and J. Furthmüller. Efficient iterative schemes for ab initio total-energy calculations using a plane-wave basis set. *Physical Review B*, 54(16):11169–11186, October 1996.

[55] G. Kresse and D. Joubert. From ultrasoft pseudopotentials to the projector augmented-wave method. *Physical Review B*, 59(3):1758–1775, January 1999.

[56] N. Q. Lam, L. Dagens, and N. V. Doan. Calculations of the properties of self-interstitials and vacancies in the face-centred cubic metals Cu, Ag and Au. *Journal of Physics F: Metal Physics*, 13(12):2503–2516, December 1983.

[57] A. Landa, P. Wynblatt, A. Girshick, V. Vitek, A. Ruban, and H. Skriver. Development of Finnis–Sinclair type potentials for Pb, Pb–Bi, and Pb–Ni systems: Application to surface segregation. *Acta Materialia*, 46(9):3027–3032, May 1998.

[58] Yun-Jae Lee, Trinh Thi Ly, Taehun Lee, Krisztián Palotás, Se Young Jeong, Jungdae Kim, and Aloysius Soon. Completing the picture of initial oxidation on copper. *Applied Surface Science*, 562:150148, 2021.

[59] B. Legrand, G. Tréglia, and F. Ducastelle. On some Spectacular Surface Segregation Behaviors in CuNi and PtNi Alloys Analyzed within the Tight-Binding Ising Model. In Vaclav Vitek and David J. Srolovitz, editors, *Atomistic Simulation of Materials: Beyond Pair Potentials*, pages 461–466. Springer US, Boston, MA, 1989.

[60] Tony Lelièvre. Metastability: a journey from stochastic processes to semiclassical analysis, Oct 2017.

[61] Malte Lenz, Mingjian Wu, and Erdmann Spiecker. Segregation-assisted climb of Frank partial dislocations: An alternative route to superintrinsic stacking faults in L12-hardened superalloys. *Acta Materialia*, 191:270–279, June 2020.

[62] Guanxing Li, Songda Li, Zhong-Kang Han, Chen Zou, Hanglong Wu, Wentao Yuan, Beien Zhu, Yi Gao, Hangsheng Yang, Ze Zhang, and Yong Wang. In Situ Resolving

the Atomic Reconstruction of SnO2 (110) Surface. *Nano Letters*, 21(17):7309–7316, September 2021.

[63] Lei Li, Xinyu Li, Zhiyao Duan, Randall J. Meyer, Rob Carr, Sumathy Raman, Lucas Koziol, and Graeme Henkelman. Adaptive kinetic Monte Carlo simulations of surface segregation in PdAu nanoparticles. *Nanoscale*, 11(21):10524–10535, May 2019.

[64] Meng Li, Matthew Curnan, Richard Garza, Michael Gresh-Sill, Stephen House, Wissam Saidi, and Judith Yang. In Situ Atomic Scale ETEM Observation of Oxide Nucleation and Growth During Initial Oxidation of Cu and Cu-Ni Alloy. *Microscopy and Microanalysis*, 26(S2):1672–1673, August 2020.

[65] Meng Li, Matthew T. Curnan, Wissam A. Saidi, and Judith C. Yang. Uneven Oxidation and Surface Reconstructions on Stepped Cu(100) and Cu(110). *Nano Letters*, 22(3):1075–1082, February 2022.

[66] Meng Li, Matthew T. Curnan, Wissam A. Saidi, and Judith C. Yang. Uneven oxidation and surface reconstructions on stepped cu(100) and cu(110). *Nano Letters*, 22(3):1075–1082, 2022. PMID: 35086335.

[67] Xin Lian, Penghao Xiao, Renlong Liu, and Graeme Henkelman. Communication: Calculations of the (2 × 1)-o reconstruction kinetics on cu(110). *The Journal of Chemical Physics*, 146(11):111101, 2017.

[68] Maxime Lortie, Rima Isaifan, Yun Liu, and Sander Mommers. Synthesis of CuNi/C and CuNi/-Al2O3 Catalysts for the Reverse Water Gas Shift Reaction. https://www.hindawi.com/journals/ijce/2015/750689/, 2015.

[69] Alexander Y. Lozovoi, Ali Alavi, and Michael W. Finnis. Surface Stoichiometry and the Initial Oxidation of NiAl(110). *Physical Review Letters*, 85(3):610–613, July 2000.

[70] René Marcelin. Contribution a l'étude de la cinétique physico-chimique. *Annales de Physique*, 3:120–231, 1915.

[71] E. H. Megchiche, C. Mijoule, and M. Amarouche. First principles calculations of vacancy-vacancy interactions in nickel: Thermal expansion effects. *Journal of Physics. Condensed Matter: An Institute of Physics Journal*, 22(48):485502, December 2010.

[72] Nicholas Metropolis, Arianna W. Rosenbluth, Marshall N. Rosenbluth, Augusta H. Teller, and Edward Teller. Equation of State Calculations by Fast Computing Machines. *The Journal of Chemical Physics*, 21(6):1087–1092, June 1953.

[73] Radu A. Miron and Kristen A. Fichthorn. Multiple-Time Scale Accelerated Molecular Dynamics: Addressing the Small-Barrier Problem. *Physical Review Letters*, 93(12):128301, September 2004.

[74] Vahagn Mkhitaryan, Eduardo J. C. Dias, Fabrizio Carbone, and F. Javier García de Abajo. Ultrafast Momentum-Resolved Free-Electron Probing of Optically Pumped Plasmon Thermal Dynamics. *ACS Photonics*, 8(2):614–624, February 2021.

[75] F. Montalenti, M. R. Sørensen, and A. F. Voter. Closing the Gap between Experiment and Theory: Crystal Growth by Temperature Accelerated Dynamics. *Physical Review Letters*, 87(12):126101, August 2001.

[76] J. P. Muscat. Surface segregation in binary alloys: A simple theoretical model. *Journal of Physics C: Solid State Physics*, 15(4):867–879, February 1982.

[77] M. A. Novotny. Monte Carlo Algorithms with Absorbing Markov Chains: Fast Local Algorithms for Slow Dynamics. *Physical Review Letters*, 74(1):1–5, January 1995.

[78] Berk Onat and Sondan Durukanoğlu. An optimized interatomic potential for Cu–Ni alloys with the embedded-atom method. *Journal of Physics: Condensed Matter*, 26(3):035404, December 2013.

[79] Yuri N. Osetsky, Laurent K. Béland, and Roger E. Stoller. Specific features of defect and mass transport in concentrated fcc alloys. *Acta Materialia*, 115:364–371, August 2016.

[80] Emanuele Panizon, Jimena A. Olmos-Asar, Maria Peressi, and Riccardo Ferrando. Study of structures and thermodynamics of CuNi nanoalloys using a new DFT-fitted atomistic potential. *Physical Chemistry Chemical Physics*, 17(42):28068–28075, 2015.

[81] Qing Peng, Xu Zhang, and Gang Lu. Structure, mechanical and thermodynamic stability of vacancy clusters in Cu. *Modelling and Simulation in Materials Science and Engineering*, 18(5):055009, May 2010.

[82] John P. Perdew, Kieron Burke, and Matthias Ernzerhof. Generalized Gradient Approximation Made Simple. *Physical Review Letters*, 77(18):3865–3868, October 1996.

[83] Danny Perez, Ekin D. Cubuk, Amos Waterland, Efthimios Kaxiras, and Arthur F. Voter. Long-Time Dynamics through Parallel Trajectory Splicing. *Journal of Chemical Theory and Computation*, 12(1):18–28, January 2016.

[84] Lukas Pielsticker, Ioannis Zegkinoglou, Nuria J. Divins, Hemma Mistry, Yen-Ting Chen, Aleksander Kostka, Jorge Anibal Boscoboinik, and Beatriz Roldán Cuenya. Segregation Phenomena in Size-Selected Bimetallic CuNi Nanoparticle Catalysts. *The Journal of Physical Chemistry B*, 122(2):919–926, January 2018.

[85] Frederico V. Prudente, Paulo H. Acioli, and J. J. Soares Neto. The fitting of potential energy surfaces using neural networks: Application to the study of vibrational levels of H3+. *The Journal of Chemical Physics*, 109(20):8801–8808, November 1998.

[86] Marshall N. Rosenbluth. Genesis of the Monte Carlo Algorithm for Statistical Mechanics. *AIP Conference Proceedings*, 690(1):22–30, November 2003.

[87] V. M. Samsonov, I. V. Talyzin, A. Yu. Kartoshkin, and S. A. Vasilyev. Surface segregation in binary Cu–Ni and Au–Co nanoalloys and the core–shell structure stability/instability: Thermodynamic and atomistic simulations. *Applied Nanoscience*, 9(1):119–133, February 2019.

[88] Andrés Saúl, Bernard Legrand, and Guy Tréglia. Equilibrium and kinetics in the (111) surface of Cu-Ag alloys: Comparison between mean-field and Monte Carlo calculations. *Physical Review B*, 50(3):1912–1921, July 1994.

[89] J. David Schall, Paul T. Mikulski, Ginger M. Chateauneuf, Guangtu Gao, and Judith A. Harrison. 5 - Molecular Dynamics Simulations of Tribology. In Ali Erdemir and Jean-Michel Martin, editors, *Superlubricity*, pages 79–102. Elsevier Science B.V., Amsterdam, January 2007.

[90] Thomas P. Senftle, Sungwook Hong, Md Mahbubul Islam, Sudhir B. Kylasa, Yuanxia Zheng, Yun Kyung Shin, Chad Junkermeier, Roman Engel-Herbert, Michael J. Janik, Hasan Metin Aktulga, Toon Verstraelen, Ananth Grama, and Adri C. T. van Duin. The ReaxFF reactive force-field: Development, applications and future directions. *npj Computational Materials*, 2(1):1–14, March 2016.

[91] Daniel Sheppard, Rye Terrell, and Graeme Henkelman. Optimization methods for finding minimum energy paths. *The Journal of Chemical Physics*, 128(13):134106, April 2008.

[92] Robert H. Shumway and David S. Stoffer. *Time Series Analysis and Its Applications (Springer Texts in Statistics)*. Springer-Verlag, Berlin, Heidelberg, 2005.

[93] Daniel A. Steigerwald and Paul Wynblatt. Calculation of the anisotropy of equilibrium surface composition in metallic solid solutions using the embedded atom method. *Surface Science*, 193(1):287–303, January 1988.

[94] Alexander Stukowski. Visualization and analysis of atomistic simulation data with OVITO–the Open Visualization Tool. *Modelling and Simulation in Materials Science and Engineering*, 18(1):015012, December 2009.

[95] V. S. Sundaram and P. Wynblatt. A Monte Carlo study of surface segregation in alloys. *Surface Science*, 52(3):569–587, November 1975.

[96] William C. Swope, Hans C. Andersen, Peter H. Berens, and Kent R. Wilson. A computer simulation method for the calculation of equilibrium constants for the formation of physical clusters of molecules: Application to small water clusters. *The Journal of Chemical Physics*, 76(1):637–649, January 1982.

[97] Qingqing Tan, Zhisheng Shi, and Dongfang Wu. CO2 Hydrogenation to Methanol over a Highly Active Cu–Ni/CeO2–Nanotube Catalyst. *Industrial & Engineering Chemistry Research*, 57(31):10148–10158, August 2018.

[98] Guy Tréglia, Bernard Legrand, and Philippe Maugain. Surface segregation in CuNi and AgNi alloys formulated as an area-preserving map. *Surface Science*, 225(3):319–330, January 1990.

[99] C. D. S. Tuck, C. A. Powell, and J. Nuttall. Corrosion of Copper and Its Alloys. In *Reference Module in Materials Science and Materials Engineering*. Elsevier, January 2016.

[100] Adri C. T. van Duin, Siddharth Dasgupta, Francois Lorant, and William A. Goddard. ReaxFF: A Reactive Force Field for Hydrocarbons. *The Journal of Physical Chemistry A*, 105(41):9396–9409, October 2001.

[101] Loup Verlet. Computer "Experiments" on Classical Fluids. I. Thermodynamical Properties of Lennard-Jones Molecules. *Physical Review*, 159(1):98–103, July 1967.

[102] Arthur F. Voter. Parallel replica method for dynamics of infrequent events. *Physical Review B*, 57(22):R13985–R13988, June 1998.

[103] Arthur F. Voter and Jimmie D. Doll. Dynamical corrections to transition state theory for multistate systems: Surface self-diffusion in the rare-event regime. *The Journal of Chemical Physics*, 82(1):80–92, January 1985.

[104] Arthur F. Voter, Francesco Montalenti, and Timothy C. Germann. Extending the Time Scale in Atomistic Simulation of Materials. *Annual Review of Materials Research*, 32(1):321–346, 2002.

[105] K. Wandelt and C. R. Brundle. Evidence for Crystal-Face Specificity in Surface Segregation of CuNi Alloys. *Physical Review Letters*, 46(23):1529–1532, June 1981.

[106] Qiang Wang, Xinyan Wang, Jianlan Liu, and Yanhui Yang. Cu–Ni core–shell nanoparticles: Structure, stability, electronic, and magnetic properties: A spin-polarized density functional study. *Journal of Nanoparticle Research*, 19(2):25, January 2017.

[107] Kuniaki Watanabe, Masao Hashiba, and Toshiro Yamashina. A quantitative analysis of surface segregation and in-depth profile of copper-nickel alloys. *Surface Science*, 61(2):483–490, December 1976.

[108] P. R. Webber, M. A. Morris, and Z. G. Zhang. Crystal-face specificity in surface segregation of CuNi alloys. *Journal of Physics F: Metal Physics*, 16(4):413–419, April 1986.

[109] P. Weinberger, A. Vernes, L. Szunyogh, and J. Zabloudil. Describing surfaces: Semi-infinite versus thin film approaches. *Physical Review B*, 80(7):075430, August 2009.

[110] Meizhen Xiang, Yi Liao, Kun Wang, Guo Lu, and Jun Chen. Shock-induced plasticity in semi-coherent {111} Cu-Ni multilayers. *International Journal of Plasticity*, 103:23–38, April 2018.

[111] Penghao Xiao and Graeme Henkelman. Kinetic Monte Carlo Study of Li Intercalation in LiFePO4. *ACS Nano*, 12(1):844–851, January 2018.

[112] Lijun Xu and Graeme Henkelman. Adaptive kinetic Monte Carlo for first-principles accelerated dynamics. *The Journal of Chemical Physics*, 129(11):114104, September 2008.

[113] Ying Yang, Yi-An Lin, XiaoYu Yan, Fei Chen, Qiang Shen, Lianmeng Zhang, and Ning Yan. Cooperative Atom Motion in Ni–Cu Nanoparticles during the Structural

Evolution and the Implication in the High-Temperature Catalyst Design. *ACS Applied Energy Materials*, 2(12):8894–8902, December 2019.

[114] Tetyana V. Zaporozhets, Andriy Taranovskyy, Gabriella Jáger, Andriy M. Gusak, Zoltán Erdélyi, and János J. Tomán. The effect of introducing stochasticity to kinetic mean-field calculations: Comparison with lattice kinetic Monte Carlo in case of regular solid solutions. *Computational Materials Science*, 171:109251, January 2020.

[115] Ioannis Zegkinoglou, Lukas Pielsticker, Zhong-Kang Han, Nuria J. Divins, David Kordus, Yen-Ting Chen, Carlos Escudero, Virginia Pérez-Dieste, Beien Zhu, Yi Gao, and Beatriz Roldan Cuenya. Surface Segregation in CuNi Nanoparticle Catalysts During CO2 Hydrogenation: The Role of CO in the Reactant Mixture. *The Journal of Physical Chemistry. C, Nanomaterials and Interfaces*, 123(13):8421–8428, April 2019.

[116] Jian-Min Zhang, Xiang-Lei Song, Xiao-Jun Zhang, and Ke-Wei Xu. The properties and structures of the mono- and the di- vacancy in Cu crystal. *Journal of Physics and Chemistry of Solids*, 67(4):714–719, April 2006.

[117] Linfeng Zhang, Jiequn Han, Han Wang, Wissam A. Saidi, Roberto Car, and Weinan E. End-to-end Symmetry Preserving Inter-atomic Potential Energy Model for Finite and Extended Systems. *arXiv:1805.09003 [cond-mat, physics:physics]*, December 2018.

[118] S. N. Zhevnenko, I. S. Petrov, D. Scheiber, and V. I. Razumovskiy. Surface and segregation energies of Ag based alloys with Ni, Co and Fe: Direct experimental measurement and DFT study. *Acta Materialia*, 205:116565, February 2021.

[119] Qing Zhu, Wissam A. Saidi, and Judith C. Yang. Step-Induced Oxygen Upward Diffusion on Stepped Cu(100) Surface. *The Journal of Physical Chemistry C*, 119(1):251–261, January 2015.

[120] Qing Zhu, Wissam A. Saidi, and Judith C. Yang. Step-Edge Directed Metal Oxidation. *The Journal of Physical Chemistry Letters*, 7(13):2530–2536, July 2016.

[121] Qing Zhu, Wissam A. Saidi, and Judith C. Yang. Enhanced Mass Transfer in the Step Edge Induced Oxidation on Cu(100) Surface. https://pubs.acs.org/doi/pdf/10.1021/acs.jpcc.6b13055, May 2017.

[122] Chenyu Zou, Yun Kyung Shin, Adri C. T. van Duin, Huazhi Fang, and Zi-Kui Liu. Molecular dynamics simulations of the effects of vacancies on nickel self-diffusion,

oxygen diffusion and oxidation initiation in nickel, using the ReaxFF reactive force field. *Acta Materialia*, 83:102–112, January 2015.